

A11102 788858

NAT'L INST OF STANDARDS & TECH R.I.C.



A11102788858

/Development of standards for superconductors  
QC100 .U56 NO.88-3088 1988 V19 C.1 NBS-P

IYDQ

PUBLICATIONS

# DEVELOPMENT OF STANDARDS FOR SUPERCONDUCTORS

## Interim Report

### January 1986-December 1987

L.F. Goodrich, Editor

Electromagnetic Technology Division  
Center for Electronics and Electrical Engineering  
National Engineering Laboratory  
National Bureau of Standards  
Boulder, Colorado 80303

FEBRUARY 1988



Stimulating America's Progress  
1913-1988

QC  
100  
U56  
#88-3088  
1988  
c.2

Work performed under Department of Energy contract DE-AI01-76PR06010



NBSIR 88-3088

100-20888-1  
C2

# DEVELOPMENT OF STANDARDS FOR SUPERCONDUCTORS

## Interim Report

### January 1986-December 1987

L.F. Goodrich, Editor

Electromagnetic Technology Division  
Center for Electronics and Electrical Engineering  
National Engineering Laboratory  
National Bureau of Standards  
Boulder, Colorado 80303

## FEBRUARY 1988

Work performed under Department of Energy contract DE-AI01-76PR06010



---

U.S. DEPARTMENT OF COMMERCE, C. William Verity, Secretary

NATIONAL BUREAU OF STANDARDS, Ernest Ambler, Director



## FOREWORD

The broad objective of this research program is the development of standards for the definition and measurement of superconductor parameters. The utility of these standards in commerce depends upon their wide acceptance and use. To this end, an underlying objective of the program must be the maintenance of technical credibility throughout the industrial and research communities. A consistent demonstration of accuracy, precision, and general attention to detail greater than that commonly achieved by the users is obviously requisite to this goal.

A less prominent, but equally important, objective of this program is the expansion of fundamental understanding, measurement capabilities, and the technological base. These particular goals provide the necessary foundation for achieving the broader program objectives and, thus, are of primary importance.

Finally, it is necessary to maintain flexibility in direction and emphasis in order to effectively exploit the unforeseeable products of research within the context of the basic program objectives.

The work described here strongly reflects this philosophy.



## SUMMARY

Considerable progress has been made in the expansion and refinement of measurement capabilities for critical currents in practical superconductors. Most of these improvements were motivated by specific measurement applications; however, they have resulted in a general increase in measurement versatility. Both the expanded capabilities and the resulting measurements and investigations are reported.

Measurement problems associated with the determination of critical current for large conductors and ac loss measurements are the major components of the work. Many of the results have already been presented at workshops and published in the literature. Those publications not previously included in our annual reports are collected in the appendixes.

### Effect of Current Ripple on Critical Current Measurements

The effect of current ripple or noise on dc critical current measurements was systematically studied. A recent literature search indicates that this is the first documented study of this type. A low noise, battery powered current supply was required in this study in order to make the pure dc critical current measurements. Also, an electronic circuit that simulates a superconductor's general current-voltage characteristic was developed and used as an analysis tool. In order to make critical current measurements in which current ripple was present, the battery supply was modified to allow the introduction of controlled amounts of ac ripple. The effect of current ripple is a reduction in the measured dc critical current; however, ripple of sufficient amplitude can result in arbitrary measurement results. The results of this work are general and quantitatively applicable to the evaluation of critical-current data and measurement systems. A theoretical model was developed to further support and explain the ripple effect. An unexpected benefit of this work was that it led to a more precise method for general critical-current data acquisition.

### Critical Current Measurements on Cable Strands

A capability to measure localized variations in critical currents was developed in this standards program. This capability allows the measurement of the critical current profile inherent in cable strands and was used in measuring strands extracted from NbTi Rutherford cables as part of another Department of Energy program. A large variation in critical current (up to 35%) was observed along the length of the cable strand. Also, the voltage distribution along the strand was shown to be dependent upon magnetic field orientation and current direction. Many voltage taps were required in order to accurately construct the strand's voltage profile. Further, the deformation geometry of the strand dictated a close spacing of voltage taps which, in turn, resulted in a reduced voltage signal. In order to measure these low voltage signals, a low noise current supply was required to maintain an acceptable signal-to-noise ratio. The battery powered current supply was ideally suited to this application. The results of these measurements, including suggestions for specific measurement techniques, and an effective critical current definition applicable to cabled conductors, are reported and

will be incorporated into future recommendations on standard measurement methods for cable conductors.

#### NbTi Round Robin

The critical current of a large NbTi conductor was measured as part of a round robin collaboration with several other laboratories. This measurement presented an opportunity to establish and test a large conductor measurement capability. Specifically, a high-output low-noise current supply was developed and calibrated to allow critical-current measurements of the quality achieved previously using the low-current system. Also, superior magnetic field calibration equipment and techniques were developed and applied to the 10 T split pair magnet for use in these measurements. The effect of current supply ripple on these high current measurements was found to be consistent with the low current studies. Preliminary results indicate that one of the participants' measurements was about 10% lower than the consensus value. These low values were attributed to a magnet calibration error and to power supply ripple and spikes.

#### Nb<sub>3</sub>Sn Round Robin: NBS Critical Current Measurements

A 12 T, 12.7 cm diameter solenoidal magnet system was acquired (with NBS funds), tested, and calibrated. This system represents an increase in high field capability and, owing to its large bore diameter, an increase in large conductor critical-current measurement capability. The magnet calibration techniques developed for the NbTi round robin were employed in the calibration of this system. The system was used in the most recent Nb<sub>3</sub>Sn round robin measurements. The large number of samples that were to be measured in this round robin dictated a test fixture and related equipment that would allow rapid mounting, instrumentation, and measurement of the various samples with a minimum of system down time. Equipment was designed and constructed to meet these needs. The results of these measurements indicate that sample handling and mounting techniques continue to be a dominant variable in Nb<sub>3</sub>Sn critical-current measurements. In fact, a systematic study indicated that a seemingly small change in the mounting technique can result in a 40% change in the measured critical current at 12 T.

#### Critical Current Measurement System

As the design of the battery powered current supply has evolved and improved, demands for its use by several different programs and in two adjacent laboratories have greatly increased. Moreover, the dependence upon this current supply has reached the point where measurements are frequently postponed until this supply is available rather than use the commercial supplies that are at hand. The battery supply's advantage over these particular commercial supplies is twofold. First, it has much lower noise and, second, it is less susceptible to ground loop problems. The latter quality is due to its superior electrical isolation and is accomplished through the use of an optically coupled input stage. This type of electrical isolation is in many ways superior to previous methods and, consequently, its use is becoming commonplace in sensitive measurement devices (see Reference [3] of Chapter V). As a result of the increasing dependence on, and use of,

this supply, circuitry for its protection against electrical damage due to misuse has been designed and implemented. Details of the overall supply design and applications are reported.

#### Magnetic Evaluation of Cu-Mn Matrix Material for Fine-Filament Nb-Ti Superconductors

The addition of Mn to the Cu matrix of fine-filament Nb-Ti superconductors has been recently shown to reduce proximity-effect coupling between closely spaced filaments. The reduction in coupling is thought to be caused by magnetic impurity scattering of electron pairs by the Mn moments rather than simply the increased electrical resistivity of the matrix. Copper-manganese, the proposed matrix alloy, is a classical spin glass. Spin-glass effects could result in hysteresis loss and remanent magnetization in composite superconductors, features that could counteract the reduction in loss due to the Mn additions. We have examined some of the magnetic properties of Cu-Mn alloys with Mn content in the range 0.16 to 3.75 wt.% to determine whether spin-glass effects could impair the performance of fine-filament Nb-Ti conductors. It appears that, for Mn content in this range, the adverse magnetic properties of the matrix are not significant.

#### Coupling Losses Measured by Vibrating-Sample Magnetometry

Coupling losses in multifilamentary superconductors may be measured with a vibrating-sample magnetometer by varying the waiting period before recording the magnetization signal after a field change. A Nb-Ti multifilamentary wire and a multistrand cable with different twist pitches were measured for different waiting periods. For wire with long twist lengths, coupling losses may be up to two times the hysteresis loss.



## CONTENTS

	Page
FOREWORD . . . . .	iii
SUMMARY . . . . .	v
ABSTRACT . . . . .	xi
I. EFFECT OF CURRENT RIPPLE ON CRITICAL CURRENT MEASUREMENTS L. F. Goodrich . . . . .	1
II. CRITICAL CURRENT MEASUREMENTS ON CABLE STRANDS L. F. Goodrich . . . . .	13
III. NbTi ROUND ROBIN L. F. Goodrich . . . . .	15
IV. Nb <sub>3</sub> Sn ROUND ROBINS: NBS Critical Current Measurements L. F. Goodrich and S. L. Bray . . . . .	18
V. CRITICAL CURRENT MEASUREMENT SYSTEM S. L. Bray and L. F. Goodrich . . . . .	44
VI. MAGNETIC EVALUATION OF Cu-Mn MATRIX MATERIAL FOR FINE-FILAMENT Nb-Ti SUPERCONDUCTORS R. B. Goldfarb, D. L. Ried, T. S. Kreilick, and E. Gregory . .	55
VII. COUPLING LOSSES MEASURED BY VIBRATING-SAMPLE MAGNETOMETRY R. B. Goldfarb . . . . .	61
Appendix A - Current-Ripple Effect on Superconductive dc Critical Current Measurements L. F. Goodrich, S. L. Bray, and A. F. Clark . . .	64
Appendix B - Hysteresis Losses in Fine-Filament Internal-Tin Superconductors R. B. Goldfarb and J. W. Ekin . . . . .	72



DEVELOPMENT OF STANDARDS FOR SUPERCONDUCTORS

Interim Report  
January 1986-December 1987

L. F. Goodrich, Editor  
Electromagnetic Technology Division  
Center for Electronics and Electrical Engineering  
National Engineering Laboratory  
National Bureau of Standards  
Boulder, Colorado 80303

A cooperative program with the Department of Energy, the National Bureau of Standards, other national laboratories, and private industry is in progress to develop standard measurement practices for use in large scale applications of superconductivity. This report describes research for the period January 1986 through December 1987. It contains the results of critical current studies on the effect of power-supply current ripple, measurements on cable strands, an interlaboratory comparison (round robin) on a large NbTi monolithic conductor, and a Nb<sub>3</sub>Sn round robin. Several useful current supply circuits have been developed. The reduction in coupling losses in multifilamentary NbTi conductors has been addressed by a study of the magnetic properties of matrix material consisting of dilute alloys of Mn in Cu. In addition, vibrating-sample magnetometry is shown to be adaptable to the measurement of coupling losses, in addition to hysteresis losses, in multifilamentary conductors.

Key words: ac losses; circuit diagrams; critical current; current ripple; hysteresis; magnetization; niobium-tin; niobium-titanium; power supply; round robin; standards; superconductors; susceptibility.



## I. EFFECT OF CURRENT RIPPLE ON CRITICAL CURRENT MEASUREMENTS

L. F. Goodrich

The effect of sample-current power-supply ripple on the measurement of dc critical current was reported in reference [1], which is included as Appendix A in this report. A battery current supply was modified to allow the creation of current ripple with variable frequency and amplitude (see Sec. V). This was used to systematically study the effect of current ripple [1]. The presence of current ripple (any periodic departure from a dc output level) reduces the measured dc critical current ( $I_c$ ). In the present report, further calculations and comments are made on this effect that will make the results more complete and general.

### Data Acquisition

The sample voltage and current were measured at relatively fixed current ripple and numerous dc bias currents (point method). These points along the voltage-current (V-I) curve were analyzed to determine  $I_c$ . This procedure is different from the more typical procedure where the current is ramped continuously with time while the voltage and current are recorded. Ramping the current was not an option in this experiment because the ac and dc components of the current had to be accurately separated and the steady state voltage measured. The point method has some general advantages over the ramp method. The point method allows for a longer time average voltage to be measured (if voltage noise is a problem) without significantly increasing the time required for taking a complete V-I curve. This is achieved by selecting a distribution of current bias points that results in a more precise measurement. This requires taking a few widely spaced points in the low current portion of the curve to establish the base line and then taking a progressively closer-spaced point distribution as the current increases toward  $I_c$ . The point method greatly reduces the effect of inductive voltage and sample motion. The only disadvantages are that it takes longer because the voltage has to settle for each data point and the general shape of the curve has to be known *a priori*.

### Theoretical Model

The motivation for modeling the effect of current ripple on the measurement of dc critical current is to help understand what is being measured and how to generalize the results to different samples, ripple, and voltmeters. As described in reference [1], calculating the time average of the instantaneous, resistive voltage would model the measurement of dc critical current with ripple. This can be done by starting with the approximate voltage-current relationship,

$$V = V_o (I / I_o)^n,$$

where  $I_o$  is a reference critical current at a voltage criteria of  $V_o$ ,  $V$  is the instantaneous voltage,  $I$  is the instantaneous current, and  $n$  reflects the shape of the curve with typical values from 20 to 60 (a higher number is a sharper transition). The time average of this voltage ( $V_{ta}$ ) is

$$V_{ta} = \left( V_o / [ I_o ]^n \right) \int_0^1 I^n dt,$$

where the period was set to 1 s ( $\omega=2\pi s^{-1}$ ) in general. For a sinusoidal and dc current, the instantaneous current can be expressed as

$$I^n = [ i + a \sin (2\pi t) ]^n = i^n [ 1 + \{a/i\} \sin (2\pi t) ]^n,$$

where  $i$  is the dc component of the current and  $a$  is the amplitude of the sinusoidal component. Thus, the time average voltage becomes

$$V_{ta} = V_o [ i / I_o ]^n \int_0^1 [ 1 + \{a/i\} \sin (2\pi t) ]^n dt,$$

or

$$V_{ta} = V_o [ i / I_o ]^n G,$$

where  $G$  is defined as the value of the integral. Notice that  $V_{ta} = V_o$  when  $I_o^n = i^n G$ . With these definitions,  $I_o$  is the dc critical current without ripple and  $i$  is the measured dc critical current with ripple present. In order to keep the equations based on measured quantities instead of theoretical quantities, such as  $I_o$ , the percent difference ( $D$ ) is defined as the difference between  $I_o$  and  $i$  normalized to  $i$

$$D = 100 (I_o - i)/i = 100 (G^{1/n} - 1).$$

This definition is consistent with a/i ratio in the integral (the ripple is relative to the measured quantity i).

The integral G was determined by numerical integration for a number of values of n and a/i ratios. These results are shown for three different magnitudes of current ripple on Figures 1, 2, and 3. The x-axis is percent ripple amplitude (percent of a/i) and the y-axis is the percent reduction in measured critical current (D). The line of  $I_c$  reduction equal to the ac amplitude was predicted [1] as the limit as n goes to infinity, and these plots are consistent with this limit. Consider the physical meaning of a point on this limit line where the ripple amplitude is 100%; at this point, the  $I_c$  reduction is 100%. The amplitude of the ripple is equal to the measured dc critical current with ripple present (a=i) and  $I_o = 2i$ .

#### Comparison of Model and Experimental Data

The model curves are compared to the experimental data from reference [1] in Figures 4, 5, 6, and 7 for two different ranges and two different voltmeters. A few model curves are used for clarity and the experimental points are the symbols. The two types of voltmeters used to measure the sample voltage are described in [1]. The -60 Hz frequency was labeled negative to indicate that the ripple current was a triangular waveform at 60 Hz rather than a sinusoidal waveform. The experimental data fall on the model curve with an n of 40 within experimental error. The measured value of n was about 30. A model curve with an n of 30 would be a lower limit to the effect. These experimental values indicate that the effective n may be higher because of the range of electric fields that occur during the peak current (n is weak function of E) or because sample heating increases the value of n. The model and data are in close agreement, within  $\pm 2\%$  for ripple below 20% and within  $\pm 5\%$  for ripple up to 100% using an n of 30.

The model curves can be used to estimate the effect of current ripple on the measured dc critical current. For approximating the effect of commercial power supply ripple on critical current measurements, the curves of Fig. 3 may be the most useful because of their lower range. Both ripple and the reduction in critical current can be generalized to a percentage effect. Heating through ac losses may increase the size of this effect at higher amplitudes depending upon the sample geometry [1]. Voltmeter effects will also become more significant at higher amplitudes [1].

#### Superconductor Simulator

A simple electronic circuit was designed to simulate the intrinsic V-I characteristic of a superconductor. This circuit was used during current ripple studies (Appendix A) in order to characterize the response of a nanovoltmeter when subjected to a highly asymmetric periodic voltage as results from passing a dc biased ac current through a superconductor. A more general application of this circuit has been to aid in the development and testing of critical-current data acquisition systems. This circuit was developed based on an idea by J. W. Ekin and J. C. Brauch of this institution. The original idea used a diode in series with a current sensing resistor. This combination was placed in parallel with a high-current shunt resistor.

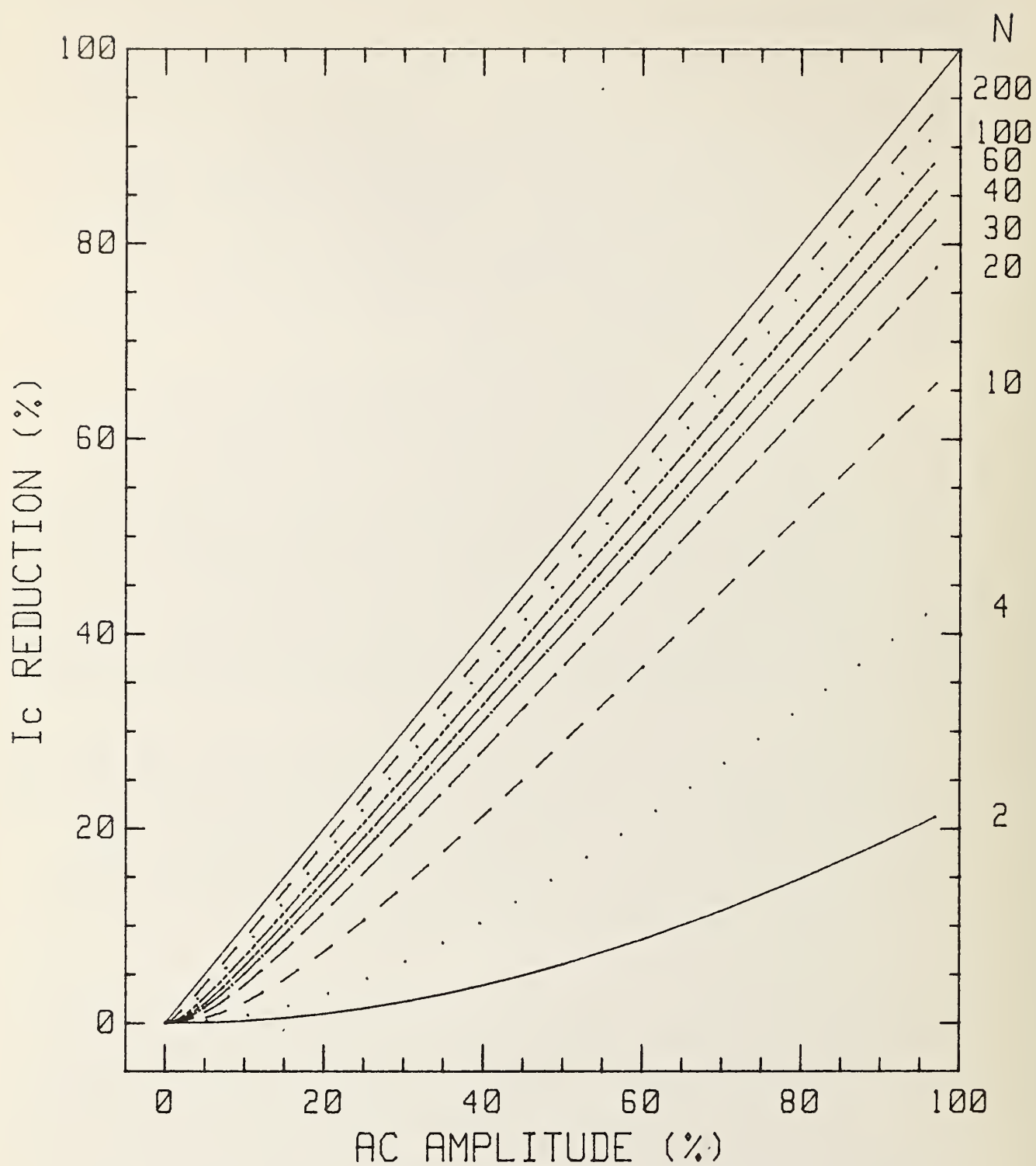


Fig. 1. Model curves of the percent  $I_c$  reduction versus the percent ac amplitude for several values of  $n$  that are listed on the right.

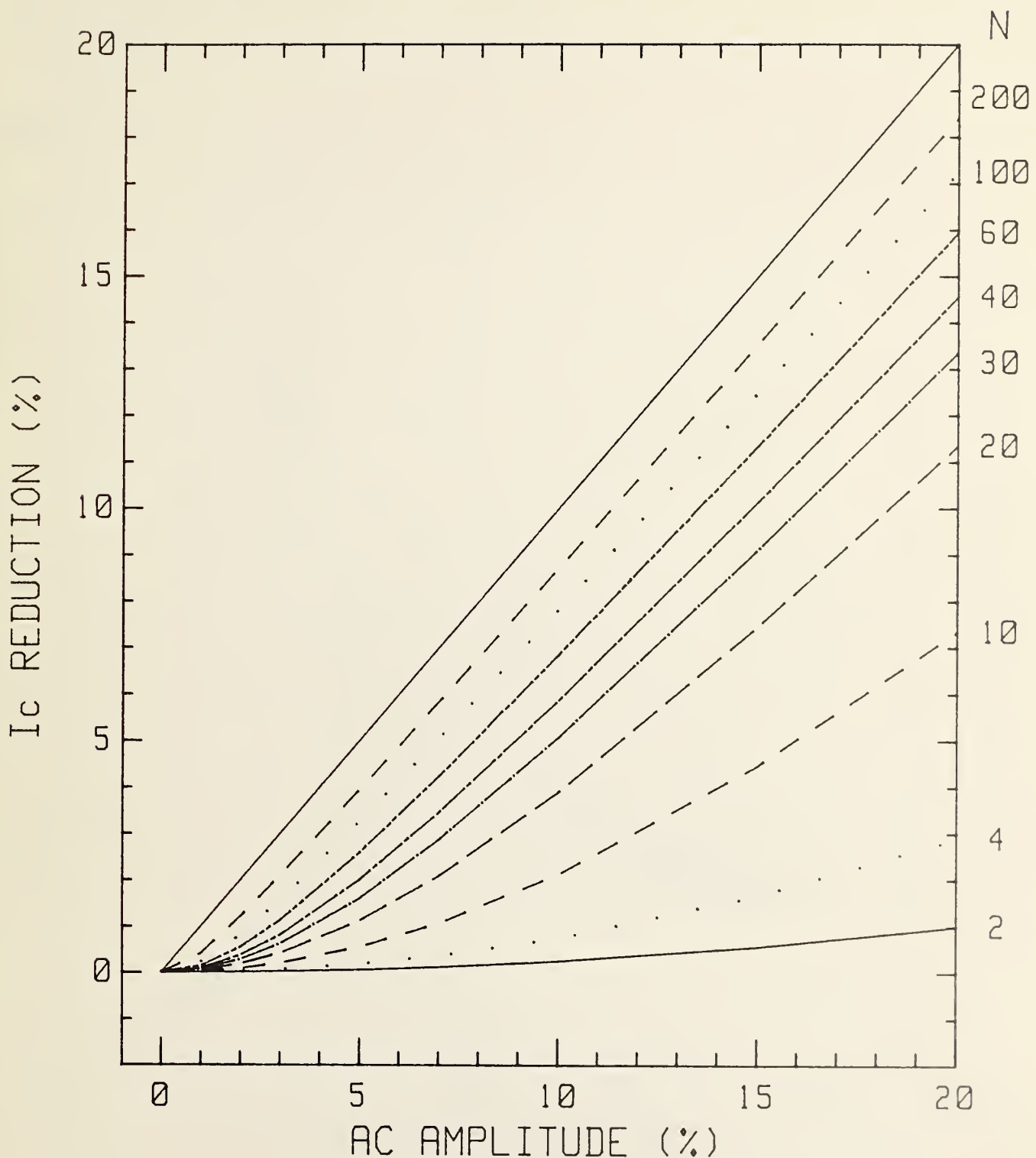


Fig. 2. Model curves of the percent  $I_c$  reduction versus the percent ac amplitude for several values of  $n$  that are listed on the right.

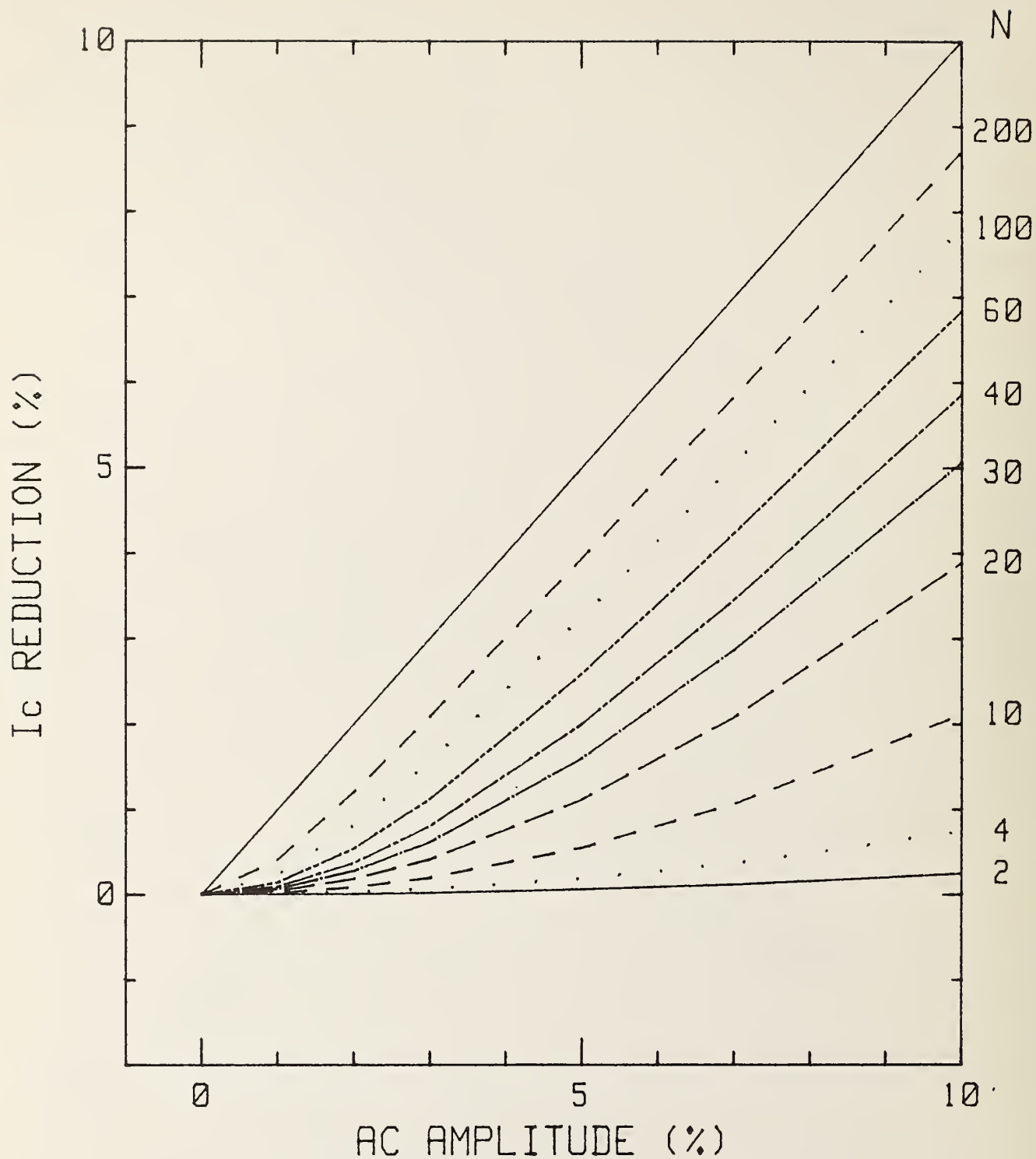


Fig. 3. Model curves of the percent  $I_c$  reduction versus the percent ac amplitude for several values of  $n$  that are listed on the right.

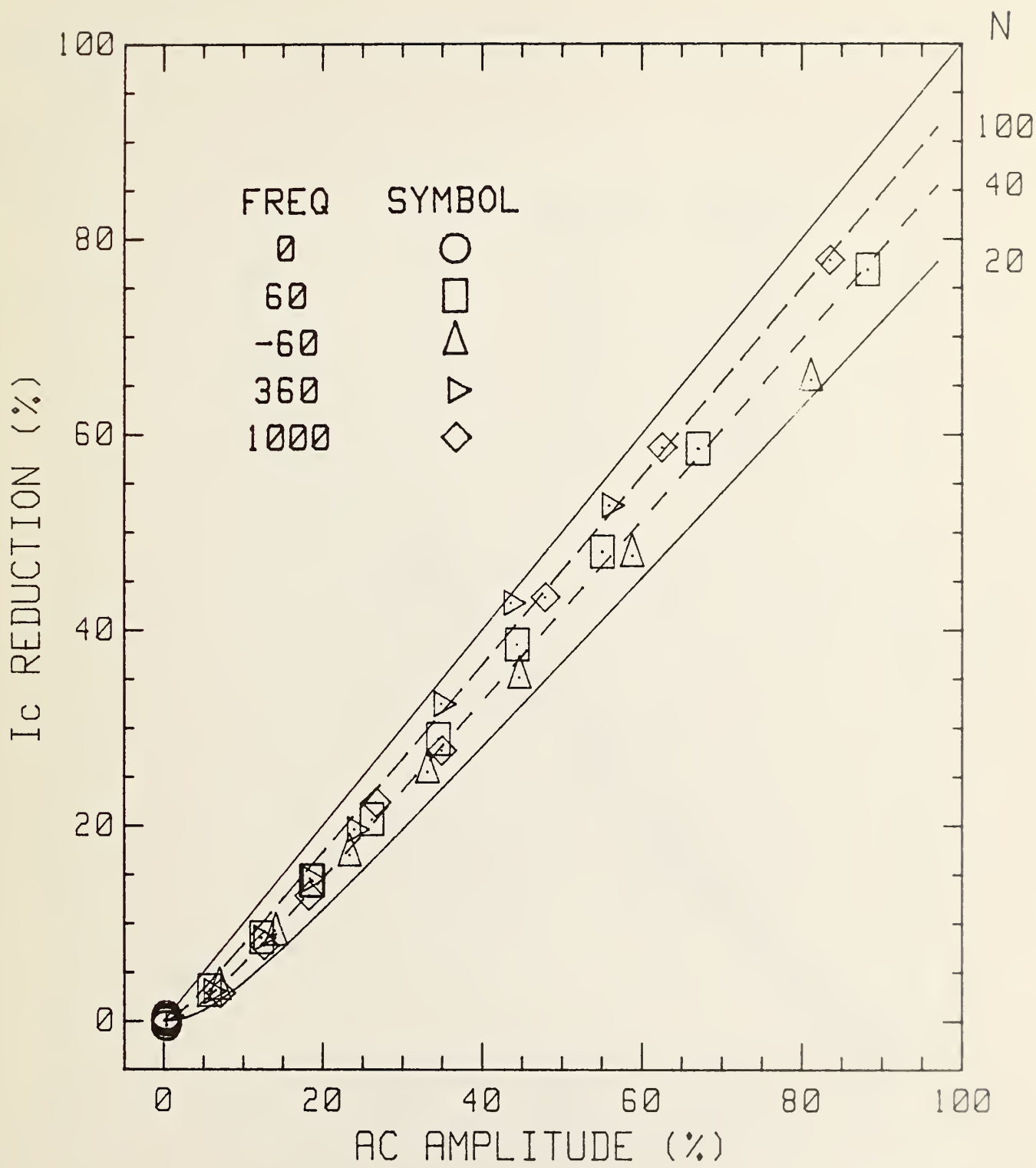


Fig. 4. The percent  $I_c$  reduction versus the percent ac amplitude. Model curves are shown for several values of  $n$  and experimental data at several frequencies using an analog voltmeter.

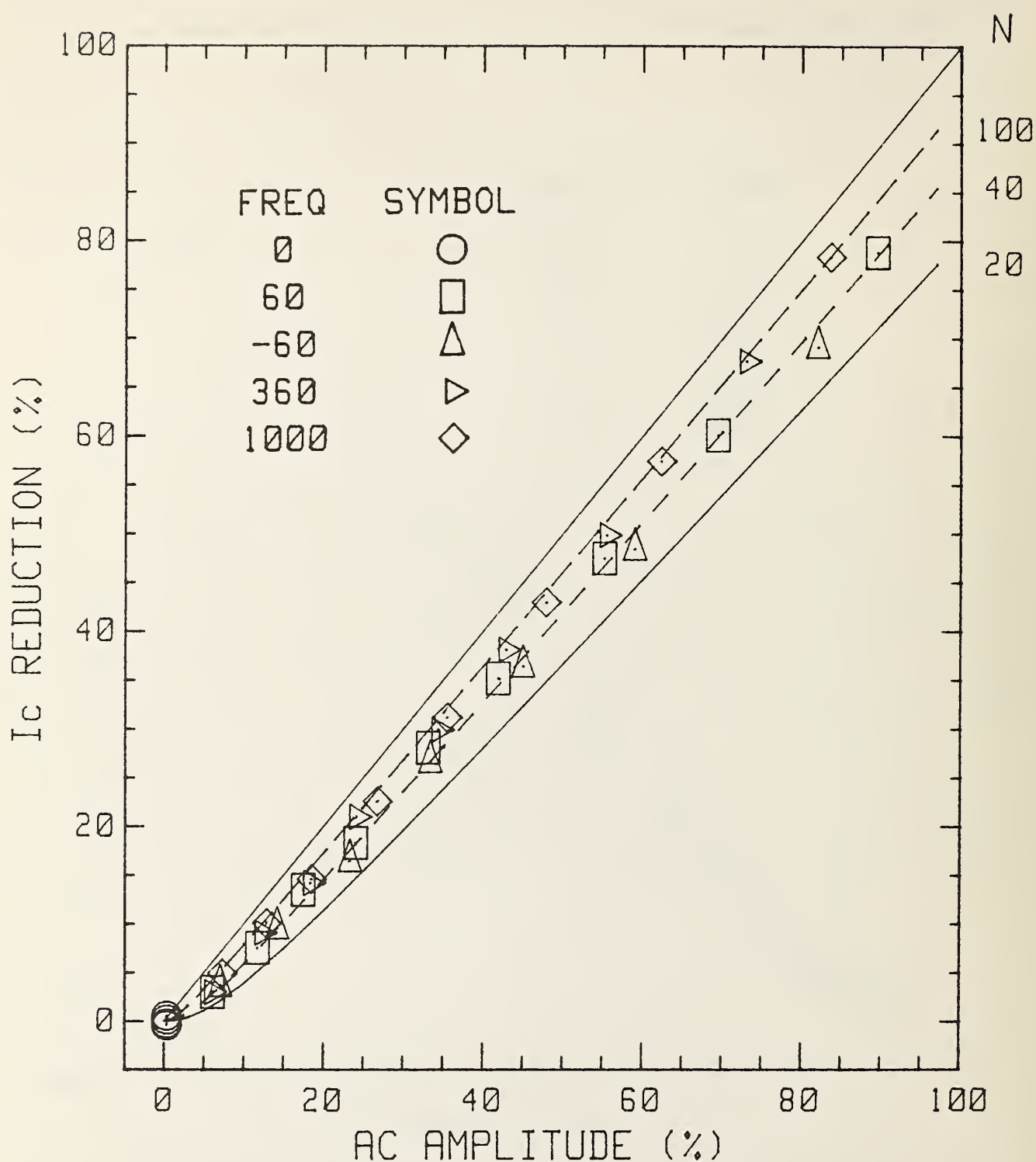


Fig. 5. The percent  $I_c$  reduction versus the percent ac amplitude. Model curves are shown for several values of  $n$  and experimental data at several frequencies using a digital voltmeter.

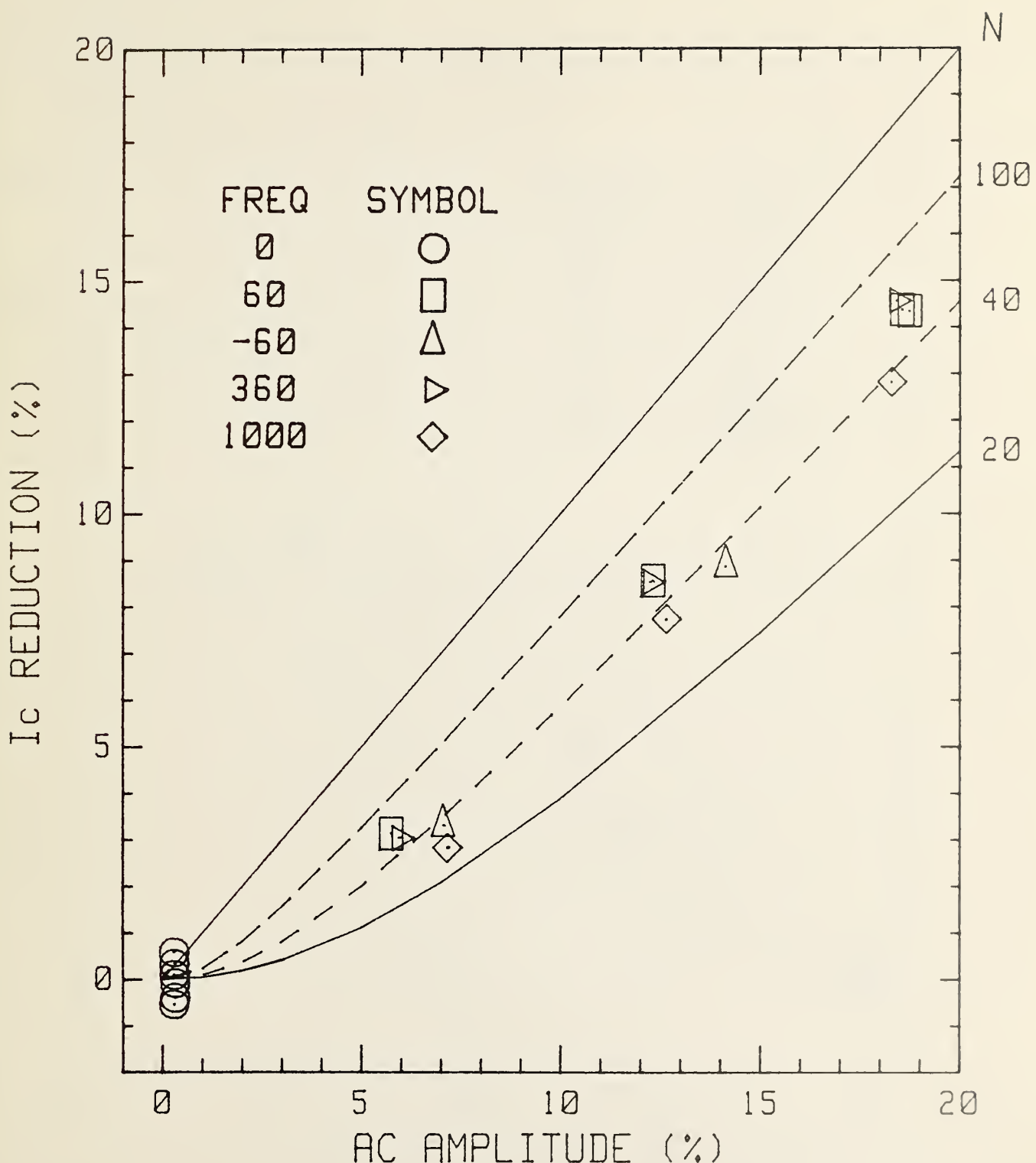


Fig. 6. The percent  $I_c$  reduction versus the percent ac amplitude. Model curves for several values of  $n$  and experimental data at several frequencies using an analog voltmeter.

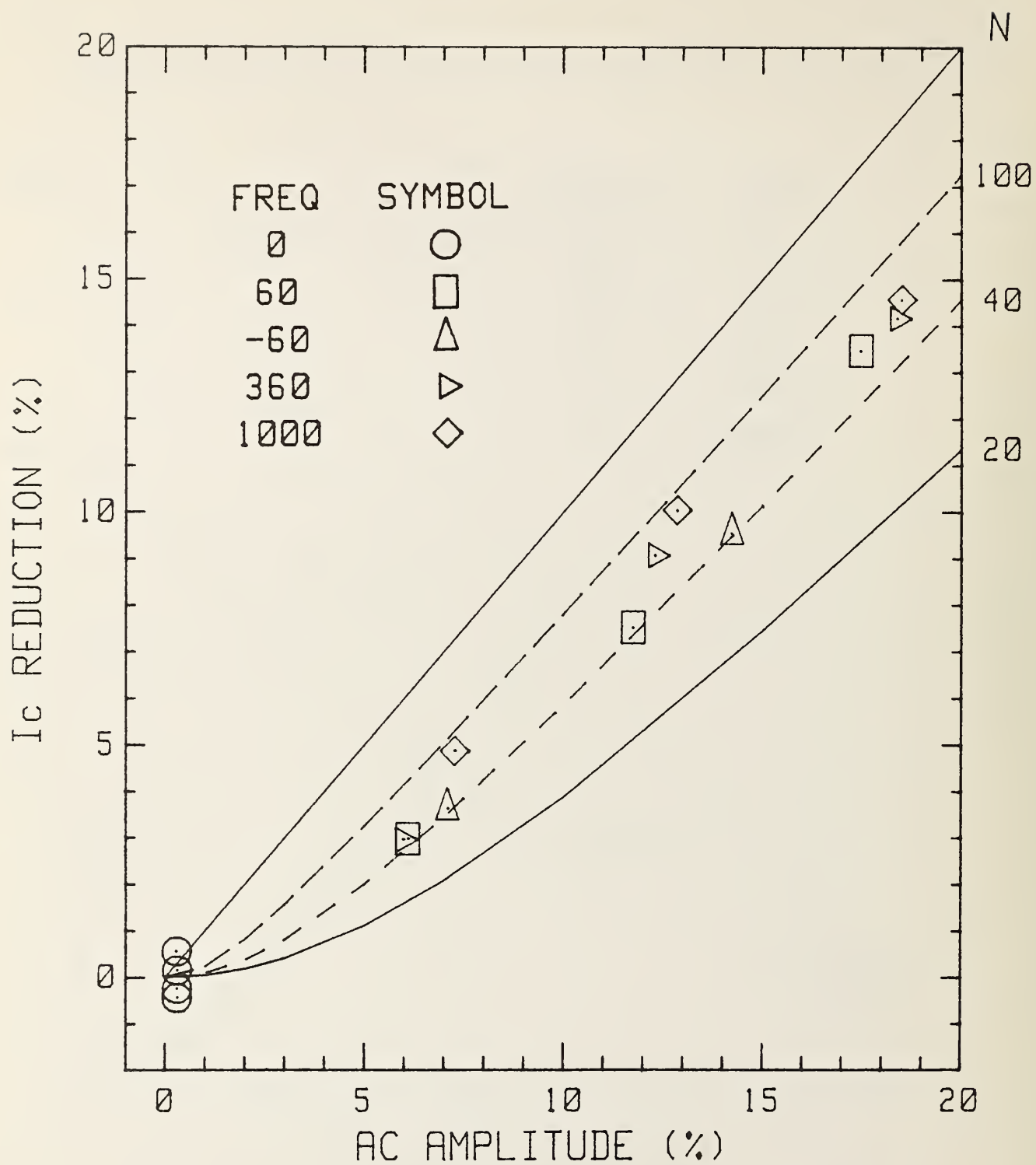


Fig. 7. The percent  $I_c$  reduction versus the percent ac amplitude. Model curves for several values of  $n$  and experimental data at several frequencies using a digital voltmeter.

This passive circuit gives a nonlinear V-I characteristic. Unfortunately, the curve is not very sharp ( $n$  about 10) and it is not adjustable. A active simulator circuit is shown in Fig. 8. The input of the simulator circuit comes from a large shunt connected in series with the current supply. This input voltage is compared with a bias voltage and then amplified. The adjustable bias voltage serves to simulate  $I_c$ . No output occurs until the input voltage has risen above the bias voltage. The gain of the amplifier may be varied and simulates the " $n$ " of a superconductor. The voltage output of this amplifier stage drives the base of a transistor. A non-linear current results on the emitter of the transistor. This non-linear current passes through a blocking diode and two shunt resistors. The output of the circuit is taken from one or the other of these shunt resistors. Typically, the nonovoltmeter to be tested is connected to the  $0.01 \Omega$  resistor and a recording instrument is connected to the  $100 \Omega$  resistor. Another channel of the recording instrument is connected to the analog output of the nonovoltmeter. These two channels are then compared and the nonovoltmeter may be thus characterized under conditions similar to an  $I_c$  measurement. The  $0.01 \Omega$  series resistor is externally connected to the remainder of the simulator circuit to allow thermal stabilization of the nonovoltmeter-to-resistor connection.

#### Reference

- [1] L. F. Goodrich, S. L. Bray, and A. F. Clark, "Current-Ripple effect on Superconducting DC Critical Current Measurements," *Adv. Cryo. Eng.-Materials*, Vol. 34, pp. 1019-1026, Plenum Press, New York (1988).

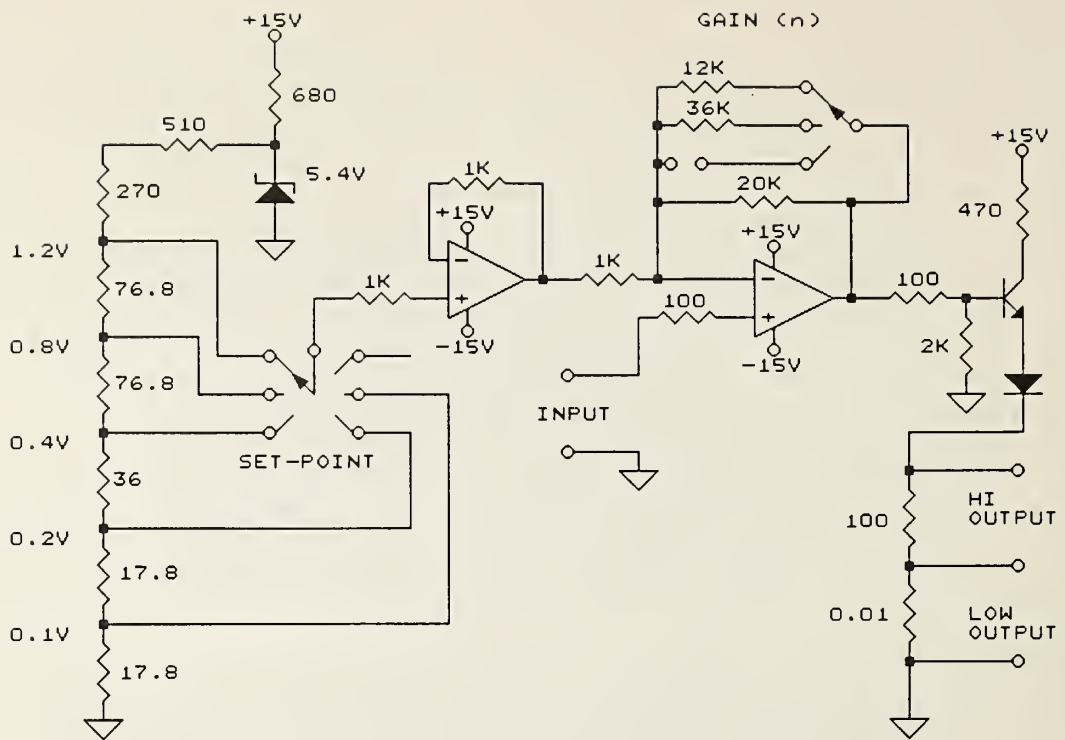


Fig. 8. Schematic diagram of an electronic circuit that simulates the intrinsic voltage-current characteristic of a superconductor.

## II. CRITICAL CURRENT MEASUREMENTS ON CABLE STRANDS

L. F. Goodrich

Detailed critical current measurements were made on the spatial and angular dependency of the local critical current,  $I_c$ , of strands extracted from Rutherford cables [1,2] as part of the electromechanical DoE/HEP program. Previous standards work on cable critical current was published as [3]. In the present report, the implications of those results for a recommended cable test method are discussed after a summary of the results.

### Samples

A study was made of the effects of strand location and magnetic field angle on current degradation that occurs in cables that have been compacted into a keystone shape. The samples came from prototype cables for high energy physics applications.

To perform this study a number of voltage taps were placed along the length of the strand to determine its local electrical properties after it had been deformed by the cabling process. Three regions of the cable were studied: the thin edge, the face (top or bottom), and the thick edge. Each of these regions was divided with voltage taps into three approximately equal length, adjacent segments. The three segments of each cable edge were denoted as the central flat edge and the two corners (bent portion).

### Results

Results on a number of strands indicate that cabling can lead to very localized reduction in  $I_c$  within a given strand. A weak link that represents only 5% of the total length can contribute 95% of the total voltage. The local critical current varies by as much as 35% along the length of a given strand at a given magnetic field orientation. This profile with position can also change with the magnetic field orientation by as much as 15%. The  $I_c$  of the thin edge of the cable can be as much as 20% lower than the thick edge.

The effective critical current was defined as the critical current determined by adding the voltage contributions of each strand segment. This total voltage was then converted to an effective electric field by dividing by one pitch length. This was useful because it related more directly to measurements made on the whole cable where several pitch lengths were included between the voltage taps.

### Conclusions

These results have several implications for short-sample critical-current testing. First, both magnetic-field orientations need to be tested to determine the limiting case for critical current. Second, the difference between thick and thin edge degradation indicates that changing the direction of the test current (for each field orientation) will affect the critical current. This is so because the location of the peak magnetic field changes

with current direction. Thus, the peak field location relative to the thin edge should be recorded. Third, to determine an effective critical current the voltage taps should be placed an integral number of cable pitch lengths apart, preferably on the same strand to reduce transverse voltages. Fourth, the current contacts should be an integer number of cable twist pitch lengths long in order to give more uniform current injection and reduce transverse voltages. Fifth, the legitimacy of the definition of effective critical current being defined as a spatial average of the local  $I_c$  needs to be demonstrated by actual practice. Dependence upon sample stability and the extent of local variations may need to be considered.

These results would be incorporated into any future recommendations on standard measurement methods for cabled conductors.

#### References

- [1] L. F. Goodrich, E. S. Pittman, J. W. Ekin, and R. M. Scanlan, "Studies of NbTi strands Extracted from Rutherford Cables," IEEE Trans. on Magnetics, Vol. MAG-23, No. 2, pp. 1642-1645 (March 1987).
- [2] J. W. Ekin, L. F. Goodrich, J. Moreland, E. S. Pittman, and A. F. Clark, "Electro-Mechanical Properties of Superconductors for High Energy Physics Applications," NBSIR 86-3061, National Bureau of Standards, Boulder, Colorado.
- [3] L. F. Goodrich, W. P. Dube, E. S. Pittman, and A. F. Clark, "The Effect of Aspect Ratio on Critical Current in Multifilamentary Superconductors," Adv. Cryog. Eng.-Materials, Vol. 32, 833, Plenum Press, New York (1986).

### III. NbTi ROUND ROBIN

L. F. Goodrich

NBS was invited by Intermagnetics General (IGC) to participate in a round robin measurement of critical current on a large NbTi conductor. Other participants were Brookhaven National Laboratory (BNL), General Electric Medical System Group, and IGC. The experiment was intended to measure the uniformity of critical current test standards among several independent laboratories. The cumulative results of the test were to be reported by IGC.

#### Sample and Measurement Specifications

The conductor was a large NbTi monolith with a 1.8 x 3.6 mm cross section and a copper-to-superconductor ratio of 2.5 to 1. It had 774 filaments, each about 52  $\mu\text{m}$  in diameter. The primary measurement conditions were at 4.2 K, 6 to 7 T, and the external magnetic field oriented transverse to the conductor axis and parallel to the wide face of the conductor. Data at two resistivity criteria ( $1 \times 10^{-11}$  and  $1 \times 10^{-12} \Omega\cdot\text{cm}$ ) were requested. The minimum critical current specification was 2500 A at 6 T and 1900 A at 7 T using the  $1 \times 10^{-11} \Omega\cdot\text{cm}$  criterion.

Several determinations of critical current were made at a number of magnetic fields (6.0, 6.2, 6.5, 6.8, 7.0, 7.2 T) in the range of interest. Therefore, the effect of random uncertainty should be negligible compared to the systematic uncertainty. The total systematic uncertainty was estimated using a straight summation of the individual uncertainties (worst case) in magnetic field, current, temperature, voltage, strain, and current transfer. No correction was made for the small (~0.3% amplitude) current ripple; however, it was included in the systematic error. The aspect ratio effect was about 13.0% at 6 T and 12.6% at 7 T (higher  $I_c$  with the magnetic field parallel to the wide face of the conductor) [1].

#### Measurement System

At the time of these measurements, our only magnet system suitable for large conductor tests was a split pair magnet with a straight sample geometry. This resulted in current transfer that was significant for this sample compared to the lower criterion of  $1 \times 10^{-12} \Omega\cdot\text{cm}$ . Thus, there was a larger uncertainty for the lower criterion. The total sample length was 42 cm, with 4 cm long current contacts. The voltage tap separation was 1.95 cm, centered in a 6.35 cm diameter magnet bore. The sample was bonded with epoxy to a 316 stainless steel mandrel. A greater length of the sample in full, perpendicular magnetic field would be necessary to reduce the current transfer voltage on the taps. As of August 1987, we have a 12.2 T, 12.7 cm diameter solenoidal magnet system purchased by NBS which will be useful for further large conductor tests.

#### System Calibration

A number of calibrations were done on the high current system before the round robin measurements. A voltage source and precision resistive divider

were used to check the calibration of the sample voltage and current amplifier channels. The current sensing resistor was calibrated against a lower-current resistor that had a previous calibration. The most involved calibration was the split pair magnet field calibration. In order to base this calibration on nuclear magnetic resonance (NMR), an NMR calibration of another magnet (normal, room temperature magnet) was required because the access of the superconducting magnet was not large enough for the necessary room temperature operation of the NMR probes. Once the normal magnet was calibrated, this calibration was transferred to a rotating coil gaussmeter. Then the rotating coil gaussmeter, inserted into a room temperature reentrant Dewar, was used to calibrate the superconducting magnet. Previously, magnetic field calibrations were done using the rotating coil gaussmeter calibrated at one point in a standard permanent magnet.

#### Effect of Current Ripple

A new technique for reducing the current ripple was used in this experiment (see the Battery Powered Current Supply section of this report for the detailed circuit). Basically it uses a low-noise, fast-response current supply to actively filter the current from a noisy, 3000 A, commercial power supply. Critical current measurements were made with and without ripple reduction to allow a precise comparison to determine the effect of ripple on the measured critical current. These measurements were made at three magnetic fields, 6, 7, and 9 T. A summary of the comparison is given in Table I. The amplitude of the ripple with active filtering was 0.3% for the two lower fields and 0.4% for 9 T, the lower current case. The effect of this level of ripple is assumed to be negligible. Without filtering, the amplitude of the ripple was 2.4, 2.2, and 2.7% respectively. The predictions came from the model curve of the current ripple section of this report. The measurements and model curves (uncertainty in the value of n) are only precise to  $\pm 0.1\%$ , but the extra digits were carried along for clarity. These results show further agreement between the model and experimental data to within the precision of the measurements. This also indicates that the effect of current ripple can be accurately modeled as a percentage effect [2].

#### Preliminary Results

Some preliminary results were communicated to NBS by IGC. There was good agreement between measurements made by BNL and NBS. IGC's measurements were about 10% lower than these. The low measurements at IGC were traced to a magnet calibration error and power supply current ripple and spikes. The magnet was recalibrated with a Hall probe. The current ripple was on the order of 2% rms. Some of the spikes originated from near-by heavy electrical equipment. To reduce the power supply noise and thus its effect on  $I_c$ , these measurements are now conducted during periods when the majority of the heavy electrical equipment is not operating. As a further check of the measurement system, the NbTi Standard Reference Material (SRM-1457) was measured and the results confirmed the system calibration.

### Acknowledgments

The author extend his thanks to W. E. Look for sample preparation, data reduction, and assistance with current shunt and magnetic field calibrations.

Table 1. A comparison of measured and calculated effect of current ripple on the measured critical current in a large conductor. Extra digits provided are for clarity.

Magnetic field	$I_c$ 0.2 $\mu$ V/cm	Percent ripple	Approximate value of n	Measured difference	Model difference
6 T	2983 A	2.4	40	0.55%	0.56%
7	2245	2.2	35	0.59	0.43
9	886	2.7	30	0.51	0.53

### References

- [1] L. F. Goodrich, W. P. Dube, E. S. Pittman, and A. F. Clark, "The Effect of Aspect Ratio on Critical Current in Multifilamentary Superconductors," *Adv. Cryog. Eng.-Materials*, Vol. 32, 833, Plenum Press, New York (1986).
- [2] L. F. Goodrich, S. L. Bray, and A. F. Clark, "Current-Ripple effect on Superconductive DC Critical Current Measurements," *Adv. Cryo. Eng.-Materials*, Vol. 34, pp. 1019-1026, Plenum Press, New York (1988).

#### IV. Nb<sub>3</sub>Sn ROUND ROBINS: NBS Critical Current Measurements

L. F. Goodrich and S. L. Bray

NBS has participated in three I<sub>c</sub> round robins on Nb<sub>3</sub>Sn conductors during the past three years. Two of these round robins developed from a Japan-USA cooperation on high-field superconducting materials for fusion energy, which started in 1980. The latest round robin developed under the Versailles Agreement on Advanced Materials and Standards (VAMAS), which involved laboratories from the European Economic Community (EEC), Japan, and the USA. In each case, a reference wire from a country or collection of countries was supplied and individual specimens of the wire were made and distributed to all laboratories.

The first Japan-USA round robin involved four laboratories from Japan (Electrotechnical Lab., Japan Atomic Energy Research Institute, National Research Institute for Metals, and Research Institute for Iron, Steel, and Other metals) and four laboratories from the USA (Brookhaven National Lab., Massachusetts Institute of Technology, NBS, and University of Wisconsin). The exchange of reference wires took place in November 1985. A paper by D. C. Larbalestier and K. Tachikawa on the results of this round robin was presented at the 1986 Applied Superconductivity Conference (Sept. 28-Oct. 3, 1986), but it was not published.

The second Japan-USA round robin involved seven laboratories from Japan (Electrotechnical Lab., Furukawa Electric, Hitachi, Japan Atomic Energy Research Institute, Kobe Steel, National Research Institute for Metals, and Research Institute for Iron, Steel, and Other Metals) and five laboratories from the USA (Brookhaven National Lab., Lawrence Livermore National Lab., Massachusetts Institute of Technology, National Bureau of Standards, and University of Wisconsin). This round robin was set up with significant constraints on the sample mounting and testing procedures that were designed to determine if a reduction could be made in the measured I<sub>c</sub> differences that were observed at high magnetic fields ( $H \geq 10$  T) in the first Japan-USA round robin test. Ultimately, the intent of this collaboration and these constraints was to improve the measurement procedures for Nb<sub>3</sub>Sn conductors. The main constraint was that all laboratories use measurement mandrels constructed from a supplied batch of G-10 tubes. Other suggestions were that all samples be bonded to the G-10 mandrel with an epoxy adhesive and that the I<sub>c</sub> be measured for both current directions (parallel and anti-parallel magnetic fields).

The VAMAS round robin was designed with few restrictions, to involve as much of the superconductor community as would like to participate. This involved an additional ten laboratories from EEC: Atominstutit der Oestereiden Universitaten (Austria), Clarendon Lab. (UK), Service National der Champs Intenses (Grenoble, France), INFN-Sez. (Genova, Italy), University of Nijmegen (Netherlands), Kernforschungszentrum Karlsruhe (FRG), Rutherford Appleton Lab. (UK), Siemens (FRG), SCK/CEN (Belgium), Vacuumschmelze GmbH (FRG). With the timing of the second Japan-USA and this VAMAS round robin, the second Japan-USA round robin became a subset of the larger VAMAS round robin. Thus, the distinction between these two may be lost with time.

This section of the report is a preliminary presentation of the measurements made at NBS Boulder for these last two round robins. Other NBS measurements of critical current as a function of strain will be presented elsewhere. It is noted that meaningful results of these measurements depend upon the collaboration among the laboratories; the knowledge of the results of other participants helps the interpretation of one's own results. To this end, all 22 laboratories that participated in the VAMAS round robin are acknowledged. A round robin is a unique setting where the intercomparison of results is essential to the advancement of measurement accuracy. The basic problem that these round robin tests reveal is that the correct and/or best method of critical current measurement for Nb<sub>3</sub>Sn is currently unclear. Thus, a statement regarding the accuracy of these measurements is presently inappropriate. A future joint publication on the results from all participants is planned.

### Samples

The samples in this round robin will be identified by letter only in order to avoid the identification of commercial products by the manufacturer's name. Some physical data is provided to indicate the general type of conductor used in these tests. In some cases these products might be indirectly identified by their particular properties. In no instance does this imply endorsement by the National Bureau of Standards, nor does it imply that the particular product was the best or worst available for this purpose.

Sample X had a wire diameter of 0.68 mm and 37 sub-bundles each containing 150 Nb filaments. The conductor fabrication method was an internal-tin, diffusion process. A single diffusion barrier of Ta separates the filament region from the outer layer of Cu. The sample reaction temperature was 700 °C for 48 h.

Sample Y had a wire diameter of 1.0 mm and 7 sub-bundles each containing 721 Nb filaments. The conductor fabrication method was a bronze, diffusion process. Each sub-bundle had a Nb diffusion barrier and the matrix was a CuSnTi alloy. The sample reaction temperature was 670 °C for 200 h.

Sample Z had a wire diameter of 0.8 mm and 114 sub-bundles each containing 54 NbTa filaments in a bronze matrix. The conductor fabrication method was a bronze, diffusion process. The Cu stabilizer was located at the center of the wire separated by a Ta barrier. The sample reaction temperature was 700 °C for 96 h.

Specimens of each sample were heat treated (reacted) at their central laboratory (central reaction). Other specimens of each sample were to be reacted at each individual measurement laboratory (self reaction). A comparison of results from these two groups would give an indication of reaction and shipping variables. Each specimen was reacted on a stainless steel tube that had a spiral groove on it to define the coil pitch. The surface of the stainless steel had been oxidized to reduce the chance of diffusion bonding the sample to the reaction mandrel. If bonding did occur, the sample could be damaged when it was removed for mounting onto the measurement mandrel. The self reactions performed at NBS were done in a

three-zone, vacuum tube furnace. The temperature of the furnace was controlled during the reaction to within  $\pm 5$  °C. The furnace temperature calibrations checked and was within  $\pm 10$  °C.

### Apparatus

The measurement mandrel was constructed from a G-10 tube that had a cylindrical Copper current contact rigidly attached to each end. Each contact had a superconductive bus bar (Cu and Nb<sub>3</sub>Sn tape) connected to it. The sample was transferred from the reaction mandrel on to the measurement mandrel by carefully unthreading the sample from the reaction mandrel and slipping it on to the measurement mandrel (not grooved). The one current contact that was removed for this transfer was reattached and the sample was tightened onto the mandrel. Each end of the sample was soldered onto its current contact. An effort was made to avoid a complete loop made by the sample and bus bar on the contact. This was done in order to circumvent slowly decaying persistent currents. Three pairs of adjacent voltage taps were placed along the center of the sample. Each pair had a separation of about 10 cm and there was a 1 to 2 cm gap between adjacent pairs. At this point the sample was bonded to the mandrel with filled epoxy (or varnish in one case) and allowed to cure. The epoxy coat was kept thin so that the thermal conductivity from the sample to the helium bath was not as limited. This unit could then be mounted onto the sample cryostat where the electrical connections were completed.

The measurements were made at about 4.2 K in a 12 T, 12.7 cm diameter superconductive solenoidal magnet. Since the ambient atmospheric pressure at this test site is low, resulting in a equilibrium liquid helium temperature of 4.0 K, the Dewar pressure was elevated. The pressure in the helium Dewar was controlled with a diaphragm-type manostat and the temperature deduced using the measured pressure. A heater on the bottom of the helium Dewar was used to remove the natural stratification and bring the bath into equilibrium at the elevated pressure.

The voltage-current curves, for all three voltage tap pairs, were taken simultaneously on a digital processing oscilloscope. An analog nanovoltmeter, with an amplified output, was used to measure the sample voltage of each tap pair. A battery powered current supply was used for the sample current. The sample voltage was measured at numerous bias currents. These points along the voltage-current curve were analyzed to determine  $I_c$ . These measurements were made with forward (anti-parallel magnetic fields, Lorentz force in) and reverse current directions in order to determine the effect of self-field and sample-to-mandrel bonding (strain effect). Unless otherwise stated, the  $I_c$  values given in this text are averages of all taps, observations, and current directions at 10  $\mu$ V/m. The precision of the  $I_c$  measurement was generally about  $\pm 0.2\%$ .

Another parameter that was determined during the  $I_c$  measurement was n. The parameter n is defined in the approximate voltage-current relationship,

$$V = V_o ( I / I_o )^n,$$

where  $I_0$  is a reference critical current at a voltage criteria of  $V_0$ ,  $V$  is the sample voltage,  $I$  is the sample current, and  $n$  reflects the shape of the curve with typical values from 20 to 60 (a higher number is a sharper transition). The value of  $n$  can be an indication of sample damage or strain.

Some specimens were difficult to measure because they would quench (thermal runaway into the normal state) at relatively low sample voltages (electric field strength about  $10 \mu\text{V}/\text{m}$ ). This resulted in more variation in the  $I_c$  values due to the small voltage range that could be analyzed. In some cases this low quench level was traced to damaged segments (weak links) adjacent to a current contact. These weak links may have been due to sample damage introduced in removing the sample from the reaction mandrel, transferring the sample to the measurement mandrel, or making the transition from the current contact to the G-10 body of the mandrel. The transition between the contact and the G-10 has two intrinsic problems. One problem arises from the differential contraction between the contact and the G-10, which causes a stress concentration. The other problem is the differential contraction between the copper contact and the sample, which introduces more sample pre-strain. Difficulties in measuring the Z sample may have been due to its high current density ( $535 \text{ A/mm}^2$  at 10 T) and bronze surface layer (larger contact resistance).

### Preliminary Results

A summary of these data on sample X is given in Table 1 and Figs. 1, 2, and 3. The effect of sample mandrel geometry, bonding method, thermal cycle, and central or self reaction variables were studied. Table 1 contains key words that relate to these variables. Each column, which is labeled with a letter from A to G, is a data set taken for a single thermal cycle of a specimen indicated by a number from 1 to 4. Some specimens, such as cycles A, B, and C for specimen 1 and also cycles E and F for specimen 3, were thermally cycled (between room and liquid helium temperatures) and measured again. The sequence of the thermal cycles was form left to right in the table. Specimens are numbered 1 through 4. The information contained in Table 1 is the critical current data, sample mandrel dimensions, and intercomparisons of critical current data. The critical current data are given at magnetic fields from 6 to 12 T.

The key words heading the columns of Table 1 (central, thick, thin, etc.) are used to indicate the measurement variables. Central indicates reaction of the specimen at a central laboratory and self indicates reaction at the individual measurement laboratory. Thick and thin refers to the ratio of wall thickness to outer radius of the sample mandrel. Under the Sample Mandrel Dimensions section of the table, these specific values are listed for each data set. Bored refers to a specimen that was originally mounted and measured on a thick walled mandrel. The specimen was then brought to room temperature (thermally cycled) and the inner diameter was bored to a larger dimension, resulting in a reduced wall thickness. The specimen's  $I_c$  was then remeasured. The typical method for bonding samples to measurement mandrels was to coat the sample and the entire surface of the mandrel with epoxy. Two variations of this technique are indicated by spiral and varnish. Spiral indicates that the sample was bonded to the mandrel with a thin stripe of epoxy along its length.

Table 1. Data on Sample X

## Critical current for Sample X

Specimen	1	1	1	2	3	3	4
$\mu_0 H, T$	Central thick	Central thick	Central thin bored	Central thin	Self thin spiral	Self thin	Self thin varnish
	(A)	(B)	(C)	(D)	(E)	(F)	(G)
6	343.3	343.2	397.3	386.3	388.9	386.6	374.5
7	268.4	267.6	318.4	308.9	312.4	310.3	297.9
8	207.0	207.4	253.8	246.0	249.7	247.6	235.9
9	156.5	156.6	200.1	193.5	197.4	195.6	184.8
10	113.6	114.0	154.7	149.3	153.2	151.6	142.1
11		78.5	116.0	111.9	114.6	112.8	106.6
12		50.2	83.5	80.4	82.5	81.1	74.6

Sample Mandrel Dimensions						
	(A)	(B)	(C)	(D)	(E)	(F)
Wall, mm	9.3	9.3	2.5	2.0	1.5	1.5
Rad., mm	15.6	15.6	15.6	15.6	15.6	15.6
w/r	60%	60%	16%	13%	10%	10%

## Intercomparison of Critical Current Data

$\mu_0 H, T$	Delta	Delta	Delta	Delta	Delta	Delta	Delta
	(A-B)/B	(B-C)/C	(C-D)/D	(E-D)/D	(F-D)/D	(G-D)/D	
6	0.0%	-11.8%	2.8%	0.7%	0.1%	-3.1%	
7	0.3%	-14.3%	3.1%	1.1%	0.5%	-3.6%	
8	-0.2%	-16.9%	3.2%	1.5%	0.7%	-4.1%	
9	-0.1%	-20.7%	3.4%	2.0%	1.1%	-4.5%	
10	-0.4%	-25.6%	3.6%	2.6%	1.5%	-4.8%	
11		-31.5%	3.7%	2.4%	0.8%	-4.7%	
12		-39.2%	3.9%	2.6%	0.9%	-7.2%	

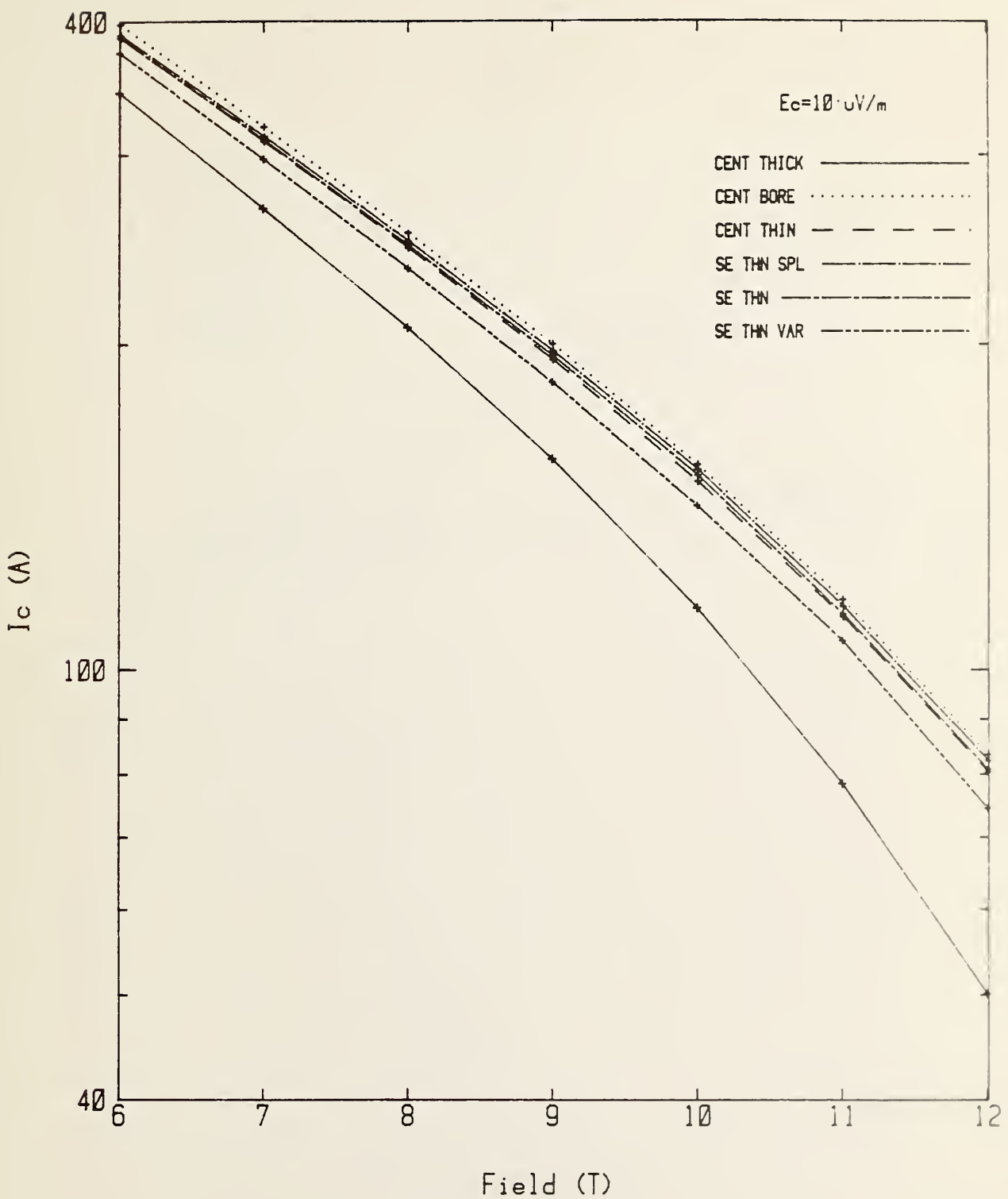


Fig. 1.  $I_c$  at  $10 \mu\text{V}/\text{m}$  versus magnetic field for specimens of sample X.

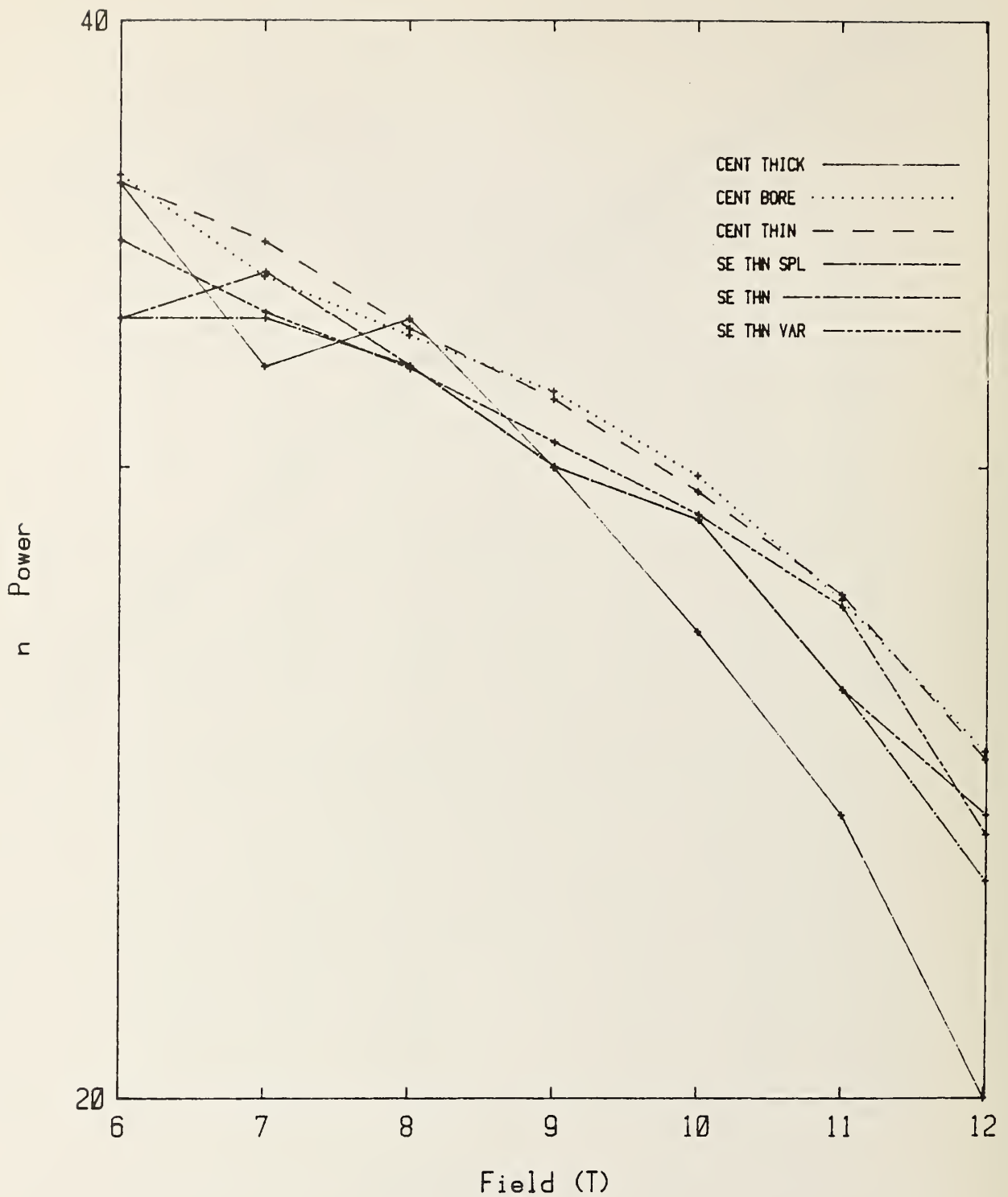


Fig. 2.  $n$  value versus magnetic field for specimens of sample X.

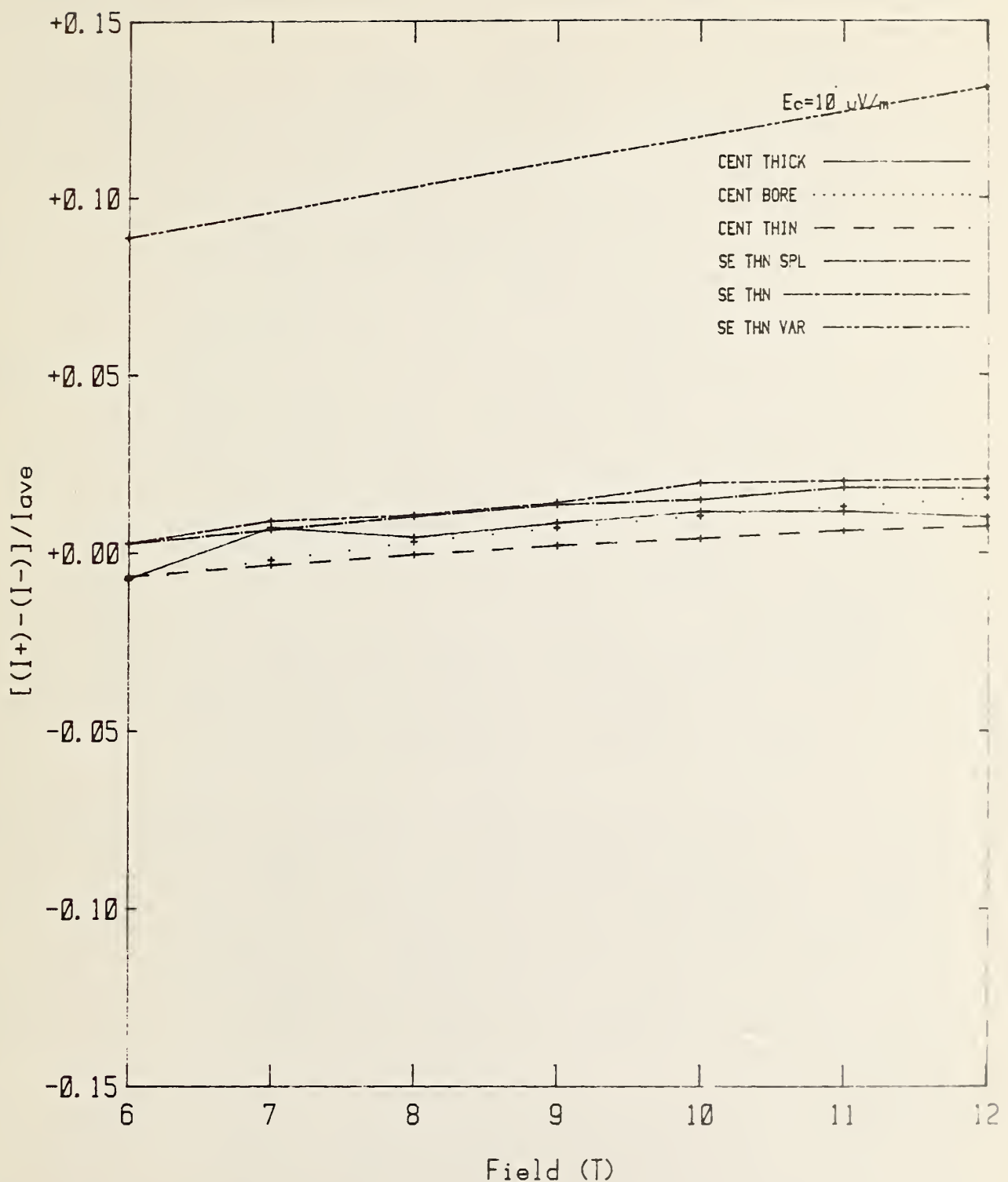


Fig. 3. Percentage difference between  $I_c$  measured with reverse and forward current directions versus magnetic field for specimens of sample X.

Varnish indicates that the sample and the mandrel were completely coated with varnish rather than epoxy.

The centrally reacted specimens were numbers 1 and 2. A comparison of the  $I_c$  data in columns A and B is a measure of  $I_c$  variation due to thermal cycling. The maximum variation was 0.4% at 10 T (the highest magnetic field for column A) as shown in the intercomparison portion of the table ( $[A-B]/B$ ). This small variation upon thermal cycling was representative of all observations. Column C was a special case of a thin walled mandrel in that it was bored (machined with the specimen mounted on the mandrel). Because this was the same specimen as A and B, the comparison is a systematic one. The intent of this procedure was to determine the effect of mandrel wall thickness on the measured  $I_c$  of a particular specimen. The intercomparison data ( $[B-C]/C$ ) shows a strongly field dependent variation of  $I_c$  (indicative of a strain effect) with a maximum difference of 39% at 12 T. This is believed to result from a change in the conductor pre-strain (at 4 K) due to variation in thermal contraction between thick and thin walled G-10 tubes. An approximate measure of the thermal contraction (from room to liquid nitrogen temperature) variations indicated a 0.2% greater contraction for the thick walled tube. Strain sensitivity measurements on this sample indicate that this additional pre-strain would result in an  $I_c$  degradation on the order of 33%. The composite nature of G-10 [1, 2, and 3] in conjunction with the compound geometry of a tube may result in a variation in radial thermal contraction between tubes of different wall thicknesses. Machining may have changed the mandrel's outer diameter at room temperature, due to stress relief, and, thus, the pre-strain state of the conductor. The rest of the intercomparisons in this table were made relative to D (central, thin) since it was thought to be a more ideal baseline for intercomparisons. The comparison between C and D showed only a small difference, 3 to 4%, with very little field dependence ( $[C-D]/D$ ). This indicates that the effect of boring was about equivalent to that of simply mounting a specimen on a thin walled tube.

The self reacted specimens on thin wall tubes were numbers 3 (E and F) and 4 (G). For data set E the specimen was bonded to the mandrel with a thin stripe of epoxy along its length (spiral). This spiral mounting technique was employed to examine the effect of a less rigid containment structure. The comparison between D and E was within 2.6%. Furthermore, the comparison of F (E with a continuous coat) with D was indicative of the small difference, 1.5%, between central and self reacted wires. The systematic difference between E and F was, thus, 1.7% or less. This demonstrates that a continuous epoxy coat was not detrimental in this case. Specimen 4 (G) was bonded to the mandrel with a coat of varnish in order to investigate the bonding properties of a less permanent adhesive. The  $I_c$  values in column G were averages of data taken with forward current only (Lorentz force into the mandrel). Some measurements were made with reverse current (Lorentz force away from the mandrel) at 6 and 12 T but these results were not included in this table. For this data set, the 12 T (magnetic field of lowest Lorentz force) measurements were made first to reduce the possibility of irreversible strain damage. However, even at this relatively low Lorentz force, there was an irreversible shift in the forward  $I_c$  after the reverse  $I_c$  measurements were made. Figure 4 is a plot of the percentage difference of the observed forward  $I_c$ 's from the average  $I_c$  at each magnetic field. For these data between 6 and 11 T, the

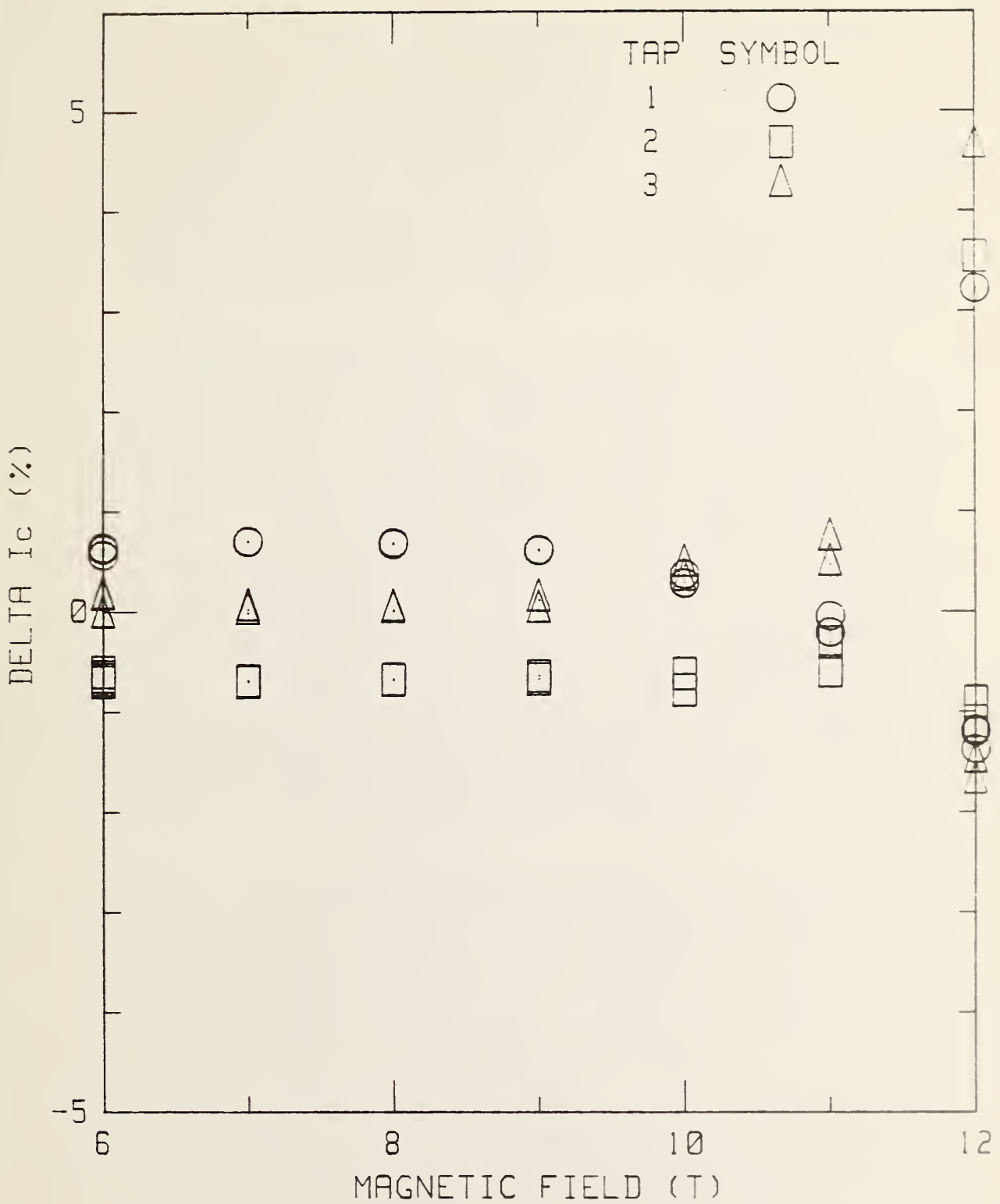


Fig. 4. Percentage difference of observed  $I_c$  versus magnetic field for specimen G (Self, thin, varnish) of sample X.

variation of measured  $I_c$ 's among the pairs of voltage taps was typical of specimen homogeneity. The indicated precision of the repeat determinations was also typical of these measurements. The first observations at 12 T are the lower group of data points. The upper group of data points were taken after the reverse  $I_c$  measurements. This irreversible enhancement can also be seen in the discontinuity of the intercomparison of G and D in Table 1. The limitations of varnish as a bonding agent are demonstrated by these results. First, the limited tensile strength of the varnish is incapable of constraining the wire on the mandrel even under moderate, outward Lorentz force. Second, even under compressive loads, the varnish seems incapable of reproducing the results obtained with epoxy. Sample inhomogeneity could also explain this difference.

Figures 1, 2, and 3 provide a graphic summary of these data on sample X. Figure 1 is a semi-logarithmic plot of  $I_c$  versus magnetic field. A semi-logarithmic plot was selected because it better illustrates the percentage differences between the curves. The four upper curves are in approximate agreement with data taken at other laboratories. The central, thick curve is significantly lower than the others and the thin, varnish curve was slightly lower. Figure 2 is a semi-logarithmic plot of n versus magnetic field. The significant element of this plot is the lower values of n for the central, thick curve at the higher magnetic fields. This is consistent with a strain degradation. The magnitude of the differences among the other curves is insignificant for this measurement variable. Figure 3 is plot of the percentage difference between reverse and forward  $I_c$  versus magnetic field. The thin, varnish curve illustrates the large strain effect, 13% at 12 T, when the sample is not adequately constrained to the mandrel. The smaller difference at 6 T was probably due to the decreased strain sensitivity at the lower magnetic field. The other curves illustrate the competition between the self-field effect, which is significant at the lower magnetic fields, and the strain effect, which is dominant at the higher magnetic fields. The maximum difference for the specimens bonded with epoxy was only 2% at 12 T which indicates that this bonding method is very positive.

A summary of these data on sample Y is given in Table 2 and Figs. 5, 6, and 7. The centrally reacted specimens were numbers 1, 2, and 3. With respect to mandrel geometry, mounting technique, and the reaction site, these specimens were the same. Data sets A and C are in good agreement (0.3% maximum variation); however, set B is in contradiction with both A and C (7.5% maximum difference). There are several possible explanations for this discrepancy including shipping damage, mounting damage, sample inhomogeneity, and variation in mandrel thermal contraction. These data are insufficient to determine the most likely source of this effect. Data set D was acquired on specimen 3 after boring and again is an indication of the pre-strain effect. The magnitude of this  $I_c$  enhancement was 17% at 12 T and is in approximate agreement with a 0.2% change in the pre-strain state of the wire as explained for sample X above. Sample Y's higher upper critical field would explain a lower strain sensitivity than that of sample X (39% at 12 T).

Data sets E and F, self reacted specimen number 4, are compared to data set D and again there is a similar  $I_c$  discrepancy (8.7% at 12 T) between two comparable specimens. The additional possible explanation for this is the

Table 2. Data on Sample Y  
Critical Current for Sample Y

Specimen	1	2	3	3	4	
$\mu_0 H, T$	Central thick (A)	Central thick (B)	Central thick (C)	Central thin bored (D)	Self thin (E)	Self thin (F)
6	398.1	372.5	397.1	447.8	429.1	
7	332.7	311.0	333.1	377.6	359.2	
8	279.4	261.2	280.0	320.5	302.4	
9	235.0	220.0	235.3	272.9	255.7	
10		184.9	198.9	232.7	216.1	
11		154.8	166.9	198.3	182.1	182.9
12		128.6	139.1	168.1		153.4
Sample Mandrel Dimensions						
	(A)	(B)	(C)	(D)	(E)	(F)
Wall, mm	9.3	9.3	9.3	2.5	2.0	2.0
Rad., mm	15.6	15.6	15.6	15.6	15.6	15.6
w/r	60%	60%	60%	16%	13%	13%
Intercomparison of Critical Current Data						
$\mu_0 H, T$	Delta	Delta	Delta	Delta	Delta	
	(A-C)/C	(B-C)/C	(C-D)/D	(F-D)/D	(E-D)/D	
6	0.3%	-6.2%	-11.3%		-4.2%	
7	-0.1%	-6.6%	-11.8%		-4.9%	
8	-0.2%	-6.7%	-12.6%		-5.6%	
9	-0.1%	-6.5%	-13.8%		-6.3%	
10		-7.0%	-14.5%		-7.1%	
11		-7.2%	-15.8%	-7.8%	-8.2%	
12		-7.5%	-17.3%	-8.7%		

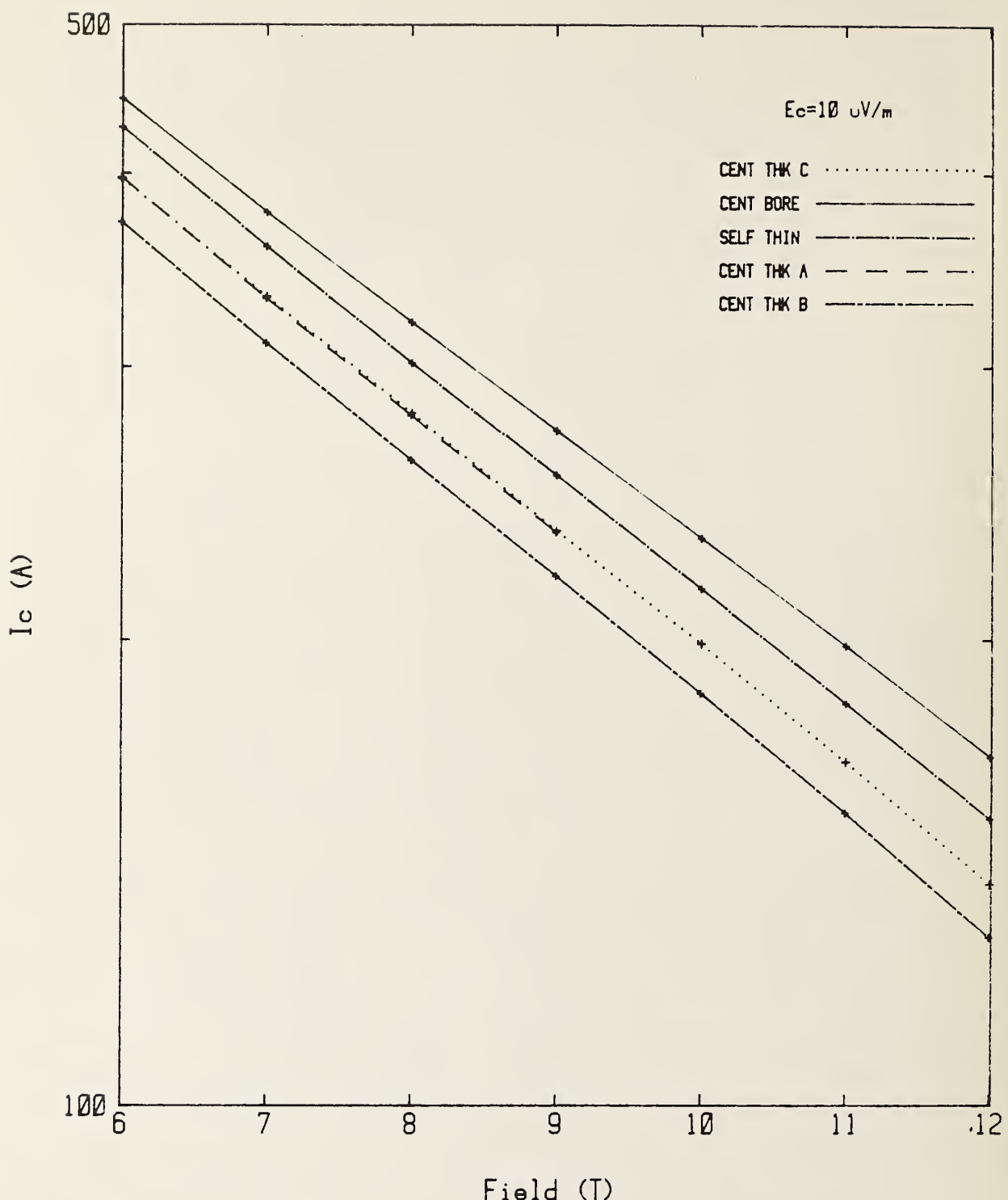


Fig. 5.  $I_c$  at  $10 \mu\text{V}/\text{m}$  versus magnetic field for specimens of sample Y.

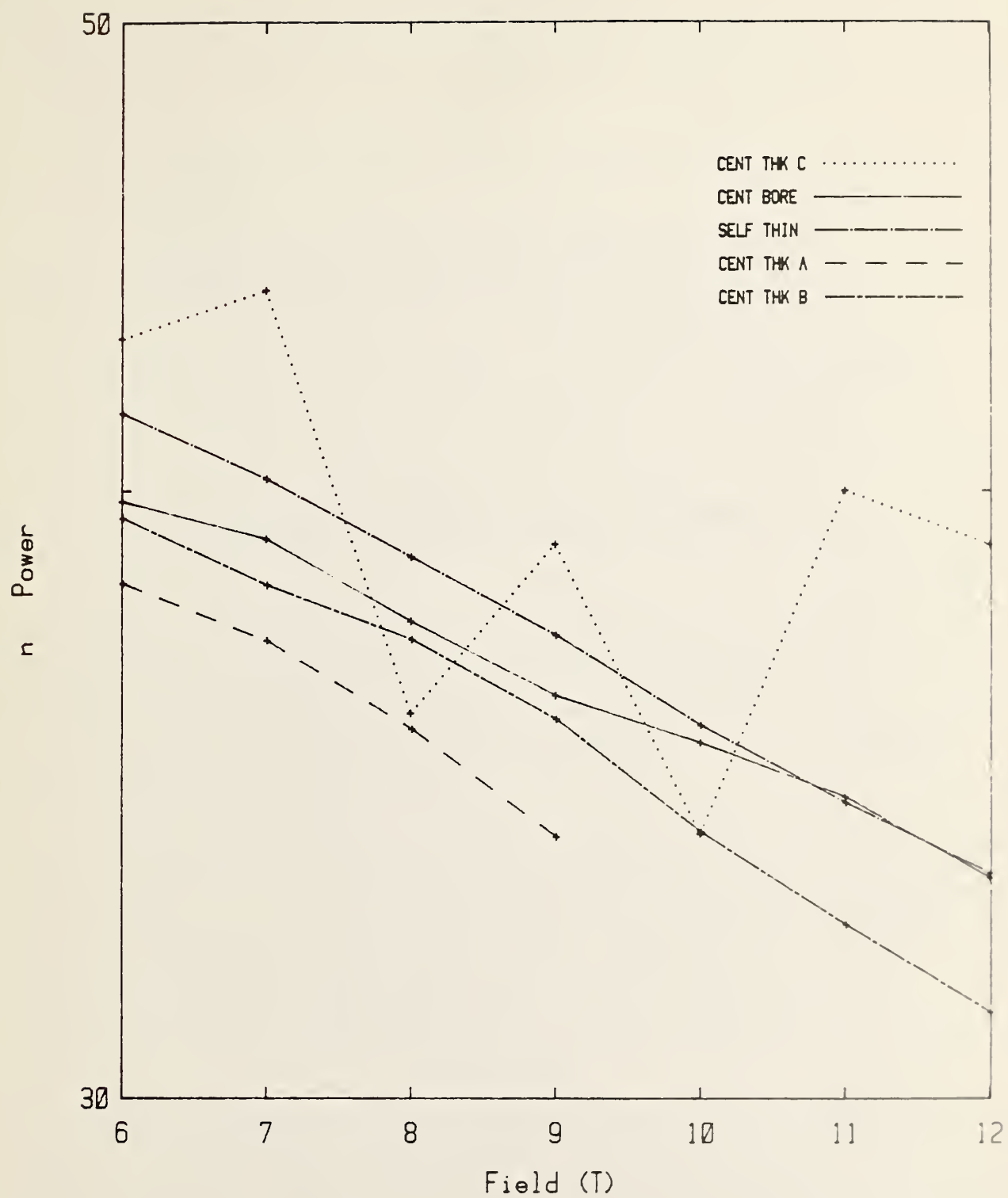


Fig. 6.  $n$  value versus magnetic field for specimens of sample Y.

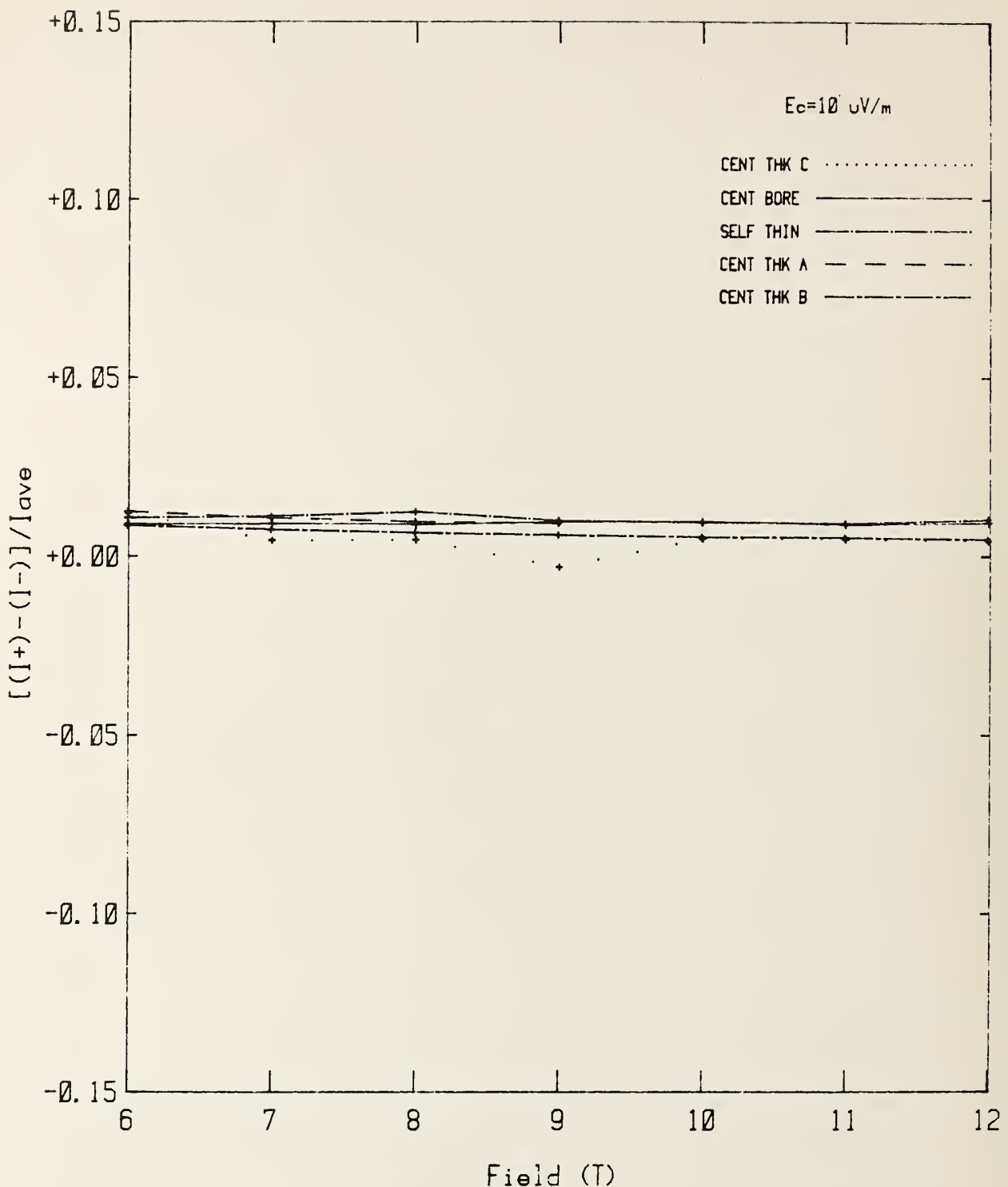


Fig. 7. Percentage difference between  $I_c$  measured with reverse and forward current directions versus magnetic field for specimens of sample Y.

fact that these specimens were reacted at different sites. A comparison of data sets E and F was another check on the effect of thermal cycling. These abbreviated data sets and resulting thermal cycle were induced by one of several magnet quenches. And, as in the previous cases, the effect of thermal cycling on  $I_c$  appears to be about 0.4%.

The most significant result for this sample is, again, the dependence of  $I_c$  on mandrel wall thickness.

Figures 5, 6, and 7 provide a graphic summary of these data on Sample Y. Figure 5 is a semi-logarithmic plot of  $I_c$  versus magnetic field. These curves show two data bands: an upper band, associated with the thin walled specimens, and a lower band, associated with thick walled specimens. While there is considerable scatter in the curves, the dominant variation is between the thick and thin walled mandrels. Figure 6 is a semi-logarithmic plot of  $n$  versus magnetic field. The larger data scatter for the central-thick-C curve may be due to the tap-to-tap  $I_c$  variation observed on this specimen. The magnitude of the differences among the other curves is insignificant for this measurement variable. Figure 7 is a plot of the percentage difference between forward and reverse  $I_c$  versus magnetic field. In this case the maximum difference was only about 1%. These curves are similar to those for sample X, Fig. 3, and indicate that the specimen was well bonded to the mandrel.

Figures 8 and 9 are plots of the percentage difference of the observed forward  $I_c$ 's from the average  $I_c$  at each magnetic field. Both of these plots contain data for specimen 3, the difference being that Fig. 8 contains central-thick-C data and Fig. 9 contains central-thick-bored-D data. The significant difference between the two plots is that the tap-to-tap  $I_c$  variation, observed in Fig. 8, was not present after boring as shown in Fig. 9. One possible explanation is a reduced longitudinal variation in G-10 thermal contraction after boring. The variation of measured  $I_c$ 's for the other specimens was similar to that of Fig. 9.

A summary of these data on sample Z is given in Table 3 and Figs. 10, 11, and 12. The centrally reacted specimens were numbers 1 and 2 with specimen 3 being self reacted. Data sets A, B, and C are in good agreement, with a 1.6% variation in  $I_c$  at 12 T. The centrally reacted specimens were measured on mandrels that had an outer diameter of about 19 mm rather than the typical 31 mm of all the other specimens. Prior to this study, this diameter was convenient for the anticipated measurements and not expected to be a significant variable. Given these limited data and this extra variable, no additional conclusion can be made regarding mandrel geometry and reaction site.

Figures 10, 11, and 12 provide a graphic summary of these data on Sample Z. Figure 10 is a semi-logarithmic plot of  $I_c$  versus magnetic field. Figure 11 is a semi-logarithmic plot of  $n$  versus magnetic field. The significant information contained in this plot is the relatively high  $n$  value for this conductor. Figure 12 is a plot of the percentage difference between forward and reverse  $I_c$  versus magnetic field. In this case the maximum difference was only about 4%. With the possible exception of the self reacted specimen, these curves are similar to those for samples X and Y, Figs. 3 and

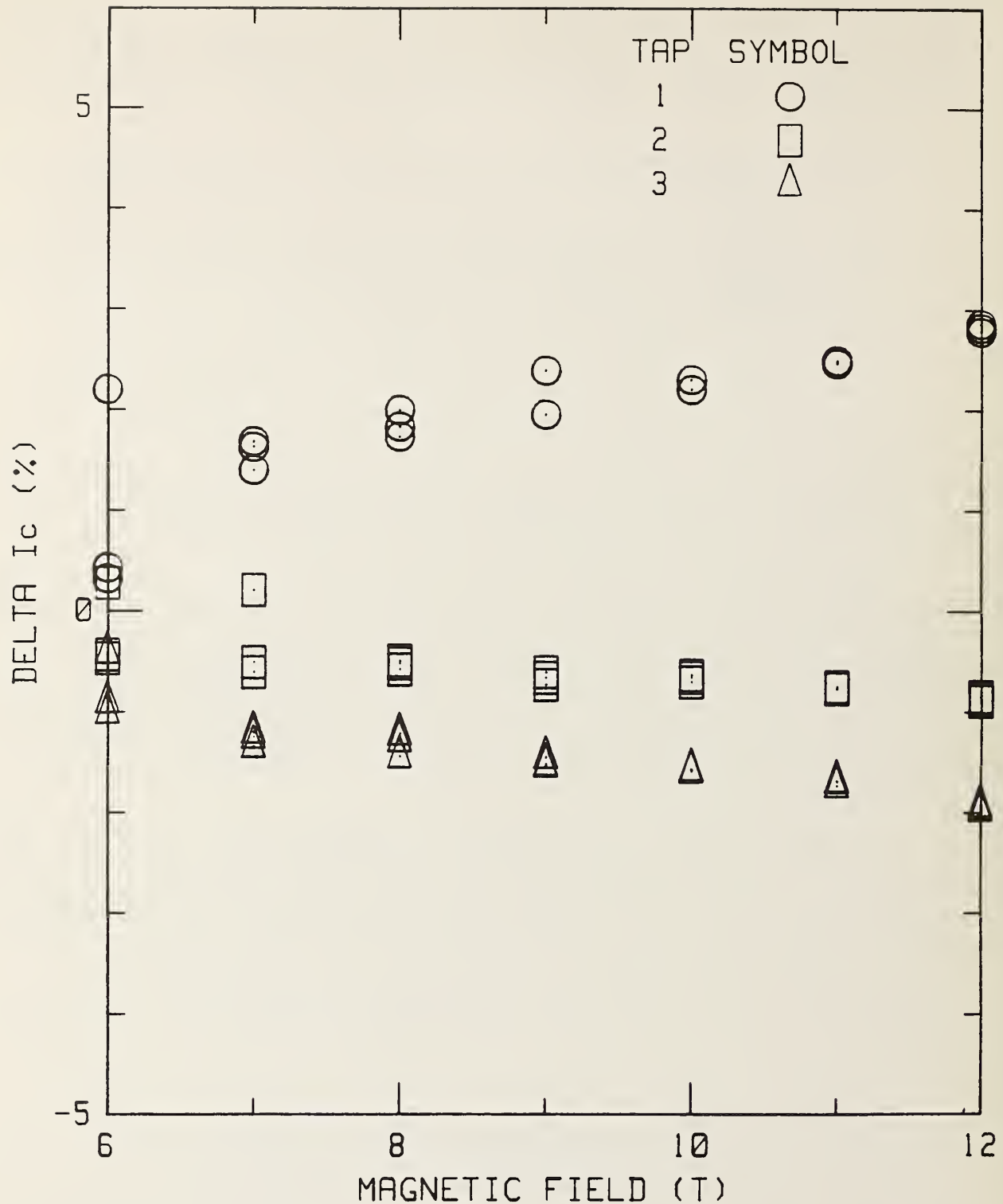


Fig. 8. Percentage difference of observed  $I_c$  versus magnetic field for specimen C (Central, thick) of sample Y.

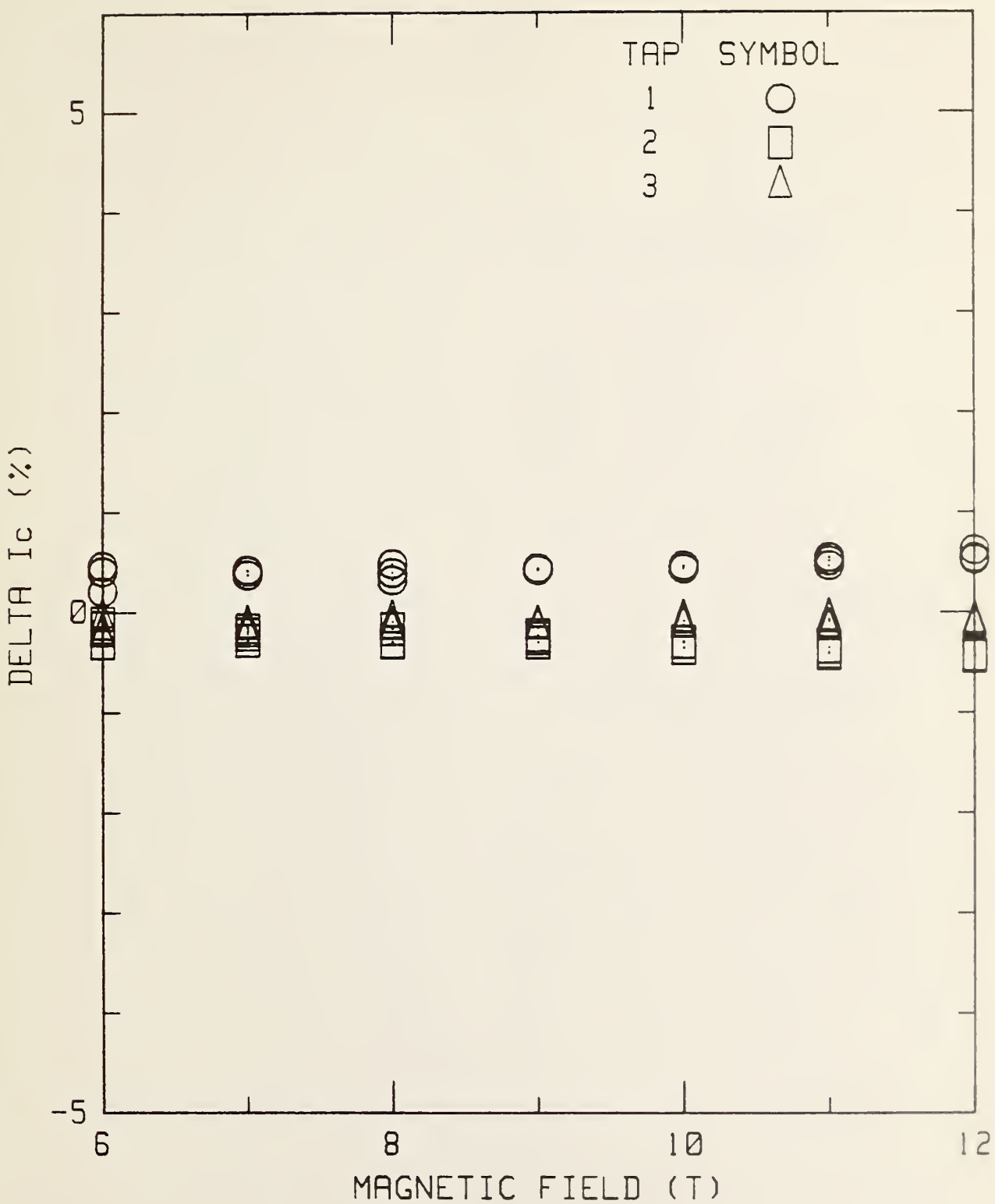


Fig. 9. Percentage difference of observed  $I_c$  versus magnetic field for specimen D (Central, thick, bored) of sample Y.

Table 3. Data on Sample Z

## Critical Current for Sample Z

Specimen	1	2	3
$\mu_0 H$ , T	Central (A)	Central (B)	Self (C)
6		544.1	
7		454.5	443.1
8		381.4	372.2
9		320.6	311.5
10	270.6	268.9	263.5
11	226.4	224.3	221.1
12	187.6	185.6	184.6

Sample Mandrel Dimensions		
	(A)	(B)
Wall, mm	3.0	3.0
Rad., mm	9.3	9.3
w/r	32%	32%
		13%

Intercomparison of Critical Current Data		
$\mu_0 H$ , T	Delta (A-B)/B	Delta (C-B)/B
6		-2.5%
7		-2.4%
8		-2.8%
9		
10	0.6%	-2.0%
11	0.9%	-1.4%
12	1.1%	-0.5%

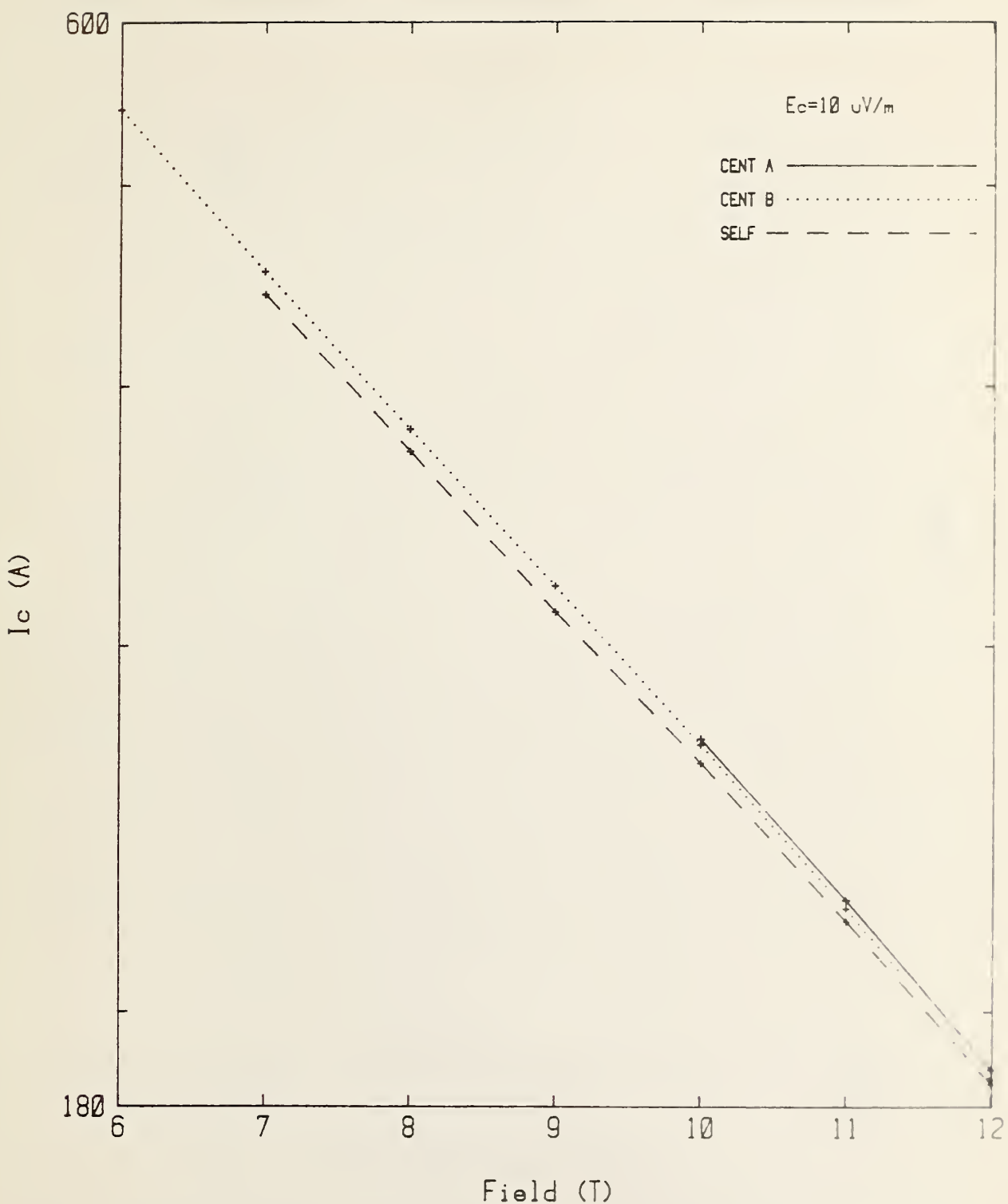


Fig. 10.  $I_c$  at  $10 \mu\text{V}/\text{m}$  versus magnetic field for specimens of sample Z.

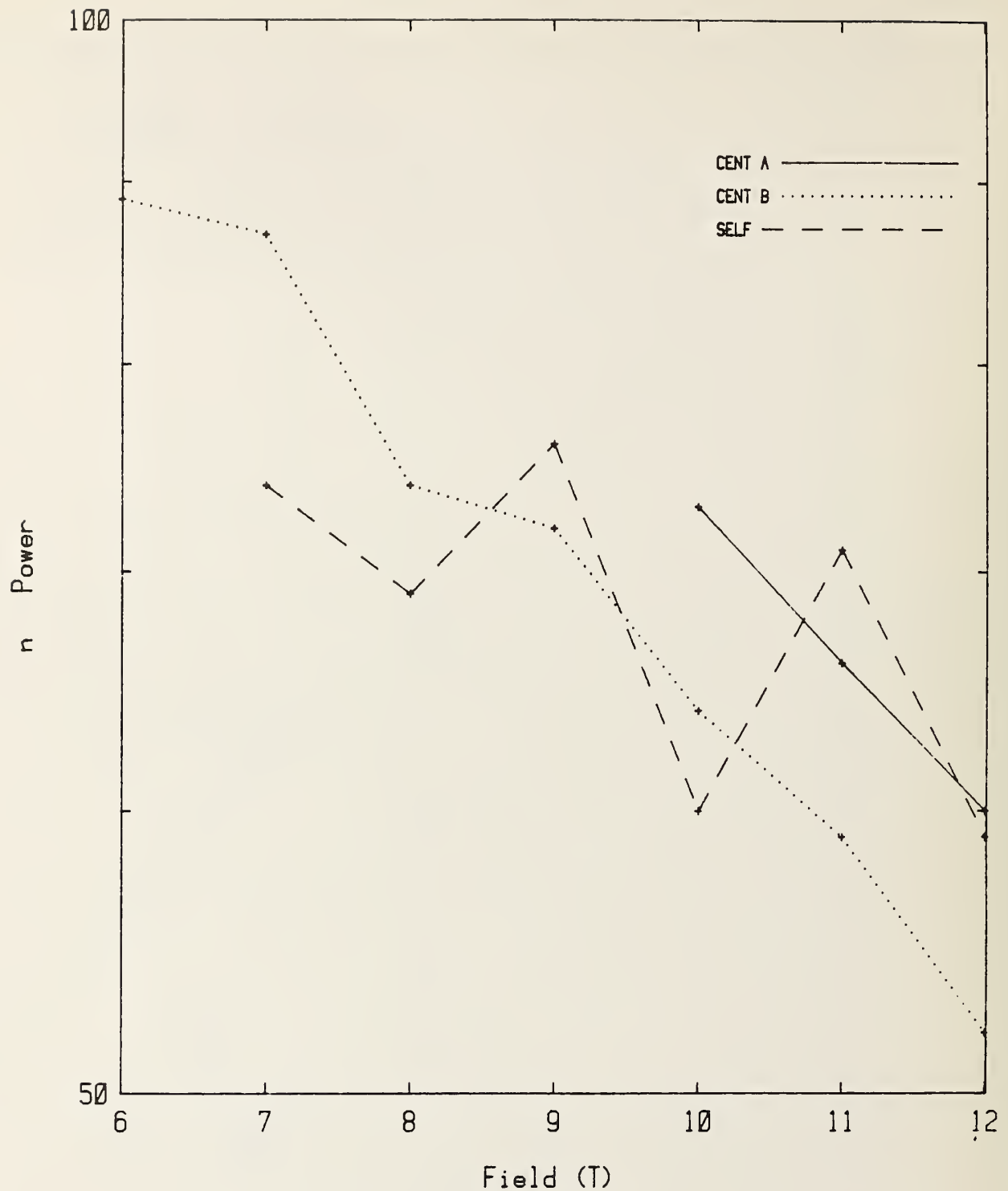


Fig. 11. n value versus magnetic field for specimens of sample Z.

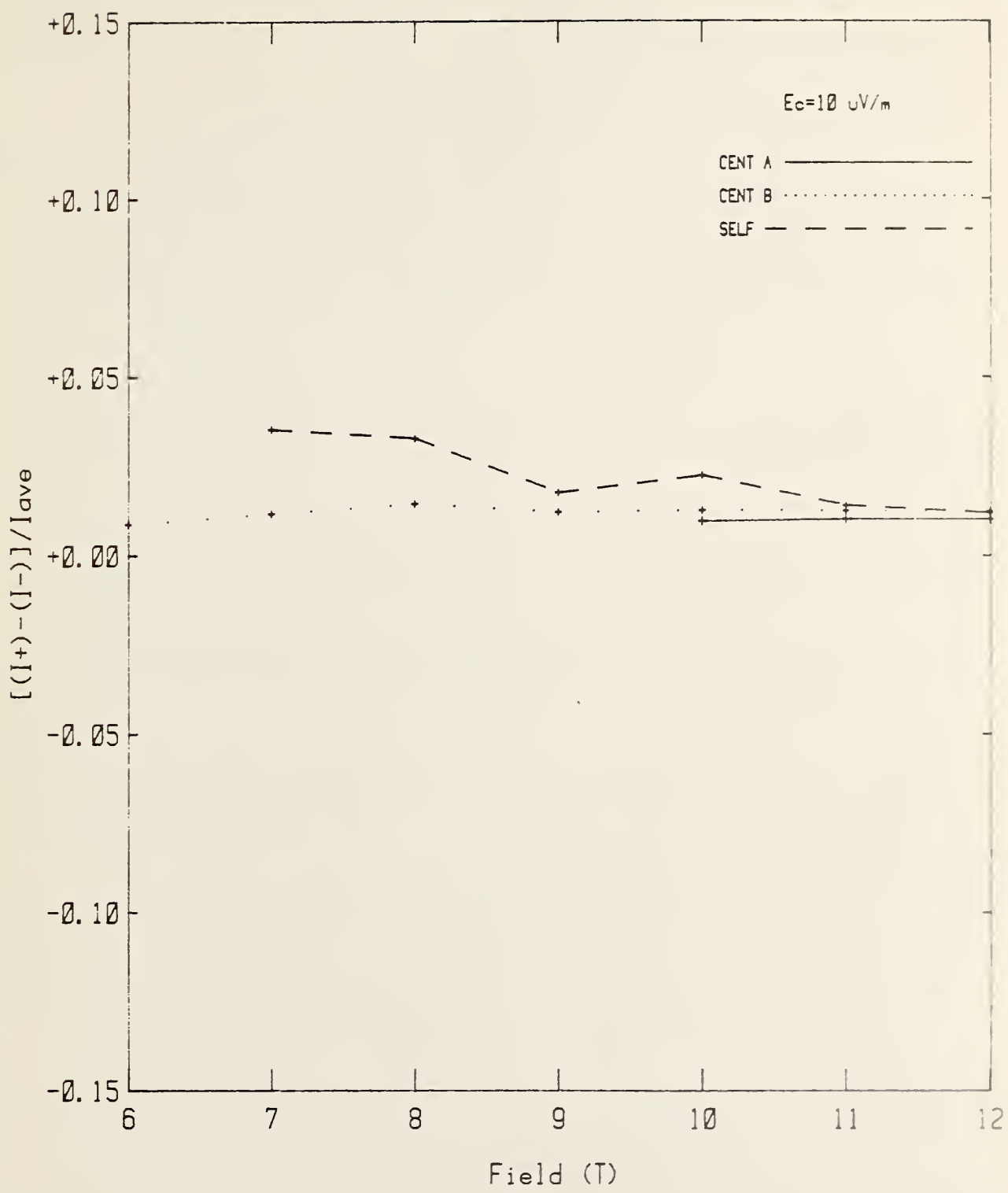


Fig. 12. Percentage difference between  $I_c$  measured with reverse and forward current directions versus magnetic field for specimens of sample Z.

7, and indicate that the specimen was well bonded to the mandrel. Within the limits of the measurement precision for this sample, homogeneity between taps was similar to the other samples.

#### Thermal Contraction Measurements and Strain Calculations

Thermal contraction measurements on NEMA-type G-10 glass-epoxy composites have been published for the plate geometry [1, 2, and 3] but, not for the tube geometry. The contraction of a G-10 plate is highly anisotropic. In composite nomenclature, the two directions in the plane of the fiberglass fabric are warp and fill. The direction perpendicular to the plane of the fabric is referred to as the normal direction. The thermal contraction from 293 K to 4 K is about 0.24% for the warp direction and 0.71% for the normal direction. The contraction in the fill direction is expected to be a little more than that of the warp direction. The contraction in the warp direction is dominated by the fiberglass fabric and the normal direction is dominated by the epoxy. The G-10 tubes used for measurement mandrels were rolled spirals of fiberglass fabric embedded in an epoxy matrix, rather than tubes machined from plate material. The radial direction for a rolled tube is normal to the fabric. The radial contraction of a tube is different than the contraction of a plate, however, because the circumferential fiberglass is put in hoop compression by the epoxy and the resulting contraction is a competition between the two structural components. The dependence of the radial contraction on wall thickness is expected to be caused by this competition.

A thick walled G-10 tube was selected as a common sample mandrel material in order to allow one size tube to be used by all the participants of the Japan-USA round robin. A thick walled tube is difficult to manufacture without getting delaminations that can cause irregular contraction and voids when they are machined. Also, the outer diameter can change when the inner diameter is bored. Another observation was that the radial contraction can be slightly asymmetric; this will result in an approximately elliptical rather than circular cross section at low temperatures. In order to make an approximate correction for this, the measurements below were the average of two approximately orthogonal diameter measurements.

As briefly mentioned above, thermal contraction measurements were made on several G-10 tubes in order to estimate the resulting conductor strain. In the interest of expediency, these measurements were limited both in accuracy and precision; nonetheless, the measurements gave a preliminary indication of the variation in thermal contraction between the tubes. These tests consisted of measuring the outside diameter of the G-10 tube at room temperature, submerging the tube in liquid nitrogen, allowing it to reach thermal equilibrium, and then quickly removing it and remeasuring the diameter. These measurements were made with a precision micrometer but they were limited by the practical difficulties of the measurement. Two tube geometries were measured; both had 31.2 mm nominal outside diameters, but one tube had a 12.7 mm inside diameter while the other had a 26.2 mm inside diameter. These two geometries have 9.3 mm and 2.5 mm walls, respectively, and are representative of the thick and thin walled mandrels. These measurements showed a substantial difference between the radial thermal contraction of G-10 tubes having different wall thicknesses. Specifically, the thin walled tube's

radial thermal contraction was ~0.23% while the thick walled tubes contraction was ~0.41%. A bias in this study exists as a result of the thermally transient measurement conditions (with a systematic difference in thermal mass) and the fact that it was conducted at liquid nitrogen, rather than liquid helium, temperature. Both of these factors result in an underestimation of the actual thermal contraction between room and liquid helium temperatures. Using the temperature dependence of the thermal contraction of G-10 plate [2 or 3], the thermal contraction to 4 K was estimated as ~0.28% for the thin walled tube and ~0.48% for the thick walled tube. The thermal contraction of the Nb<sub>3</sub>Sn conductor was only ~0.21%; consequently, the G-10 contraction may have introduced additional amounts of conductor pre-strain. The amount of compressive pre-strain might depend on several factors including the mandrel's wall thickness and the strength of the mandrel-to-conductor bond.

For samples X and Y, considerable I<sub>c</sub> tensile-strain-sensitivity data was available; however, no explicit data were available for compressive strain sensitivity. Consequently, the strain scaling law [4] in conjunction with the available tensile strain data was used to estimate the expected I<sub>c</sub> degradation for compressive strain. For Sample X the results of these calculations predict a ~33% reduction in the I<sub>c</sub> at 12 T for the thick walled specimens as compared to the thin walled ones. As mentioned above, the observed reduction was ~39%. Sample Y had a lower strain sensitivity with a predicted I<sub>c</sub> degradation of ~24% at 12 T. The actual reduction in I<sub>c</sub> for the thick mandrel as compared to the thin was ~18%. As stated, these measurements and calculations are only approximate but the trend seems to be obvious. In all cases, the thick walled samples had reduced I<sub>c</sub>'s and this reduction was in approximate agreement with that predicted by the strain scaling law.

### Discussion

Sample damage is a major concern because it can go undetected and have a significant effect on the accuracy of the I<sub>c</sub> measurement. Two potential sources of damage are specimen shipment, where the packaging of reacted samples is inadequate, and specimen transfer from the reaction mandrel to the measurement mandrel, particularly when diffusion bonding between the specimen and the stainless steel reaction mandrel has occurred. Diffusion bonding has been observed even in cases where the surface of the stainless steel was oxidized prior to sample reaction. Consequently, a more complete and reliable technique for oxidizing the reaction mandrel needs to be developed. Damage introduced by specimen transfer is easier to detect and evaluate than the other source but, if specimen damage during transfer is to be avoided, dexterity and patience are required. Unthreading the specimen from a grooved mandrel seems to be better than attempting to flex the coil to a larger diameter in order to slip it over the grooves. Long coils tend to tighten as they are unthreaded unless some torque is applied to each turn with the palm of the hand. Some observations on packaging methods that were used for shipping reacted specimens are listed here. It is not possible in this study to separate the effect of shipping damage from the effect of central versus self reaction or from sample homogeneity. The reaction mandrel alone cannot protect a sample from shipping damage. The packaging needs to protect the sample from collisions with external objects as well as from inertial

collisions with other specimens within the container or with the container. The damage or loss of samples during shipping and the delay of sample shipments by customs are characteristic problems of international round robin measurement and, hopefully, with experience these problems will be reduced.

The study concerning the effect of boring and thick-versus-thin walled G-10 tubes was not originally intended but, rather, the results of initial measurements led naturally to it. Thus, the number of specimens and the schedule limited the completeness and organization of these results. A more selective data presentation was not used because it would imply that there were fewer difficulties and that less was learned in these studies than was actually the case. Any future publication will most likely contain a more condensed version of these results to give proper weight to the significant and the definitive.

### Conclusions

Two major conclusions are that the bonding method and the mandrel material and geometry have a significant effect on the critical current measurement of Nb<sub>3</sub>Sn. Thick wall G-10 tubes contract about 0.2% more than thin wall G-10 from room to liquid helium temperature. Thus, the amount of differential thermal contraction between the mandrel and the sample depends on the wall thickness of the G-10. The method of bonding the sample to the mandrel also determines how much of the differential thermal contraction is transmitted to the sample. A positive bond will change the strain state of the sample more than a weak bond; however, a weak bond may allow the sample to be strained by the Lorentz force. The difference between critical current measurements on thick and thin wall G-10 was about 20% at 12 T for a Nb<sub>3</sub>Sn conductor with an upper critical field of 24 T and about 35% at 12 T for one with an upper critical field of 19 T.

The effect of self versus central sample reaction was not indicated as a major source of error in the resulting critical current measurements. The most direct comparison of this effect can be made on sample X, where the effect was less than 3% at 12 T. Furthermore, sample X should have been more sensitive to reaction conditions because of its relatively short reaction time, which may not have fully reacted the Nb filaments.

Some preliminary recommendations based on these results can be made. G-10 tubes with wall thickness less than about 20% of the tube radius could be used for the measurement mandrel and they would be well matched in thermal contraction to the sample. Do not use thick walled G-10 tubes with voids and machine them to make a measurement mandrel because the voids will cause irregular thermal contraction. A well oxidized stainless steel reaction mandrel should be used to reduce diffusion bonding of the sample to the mandrel and the resulting damage when the sample is transferred to the measurement mandrel. A thin, continuous coat of epoxy will provide a good bond between the sample and the mandrel.

The results presented here are preliminary in the sense that they have yet to be correlated with measurements from all 22 participating laboratories. This correlation is a necessary element in a study of this type and may

clarify the results presented here. This second round robin indicates why studies of this type need to be iterative. For example, it was anticipated that by simply using the same mandrel material, different laboratories would arrive at the same, correct  $I_c$  results. However, due to differences in bonding technique, the  $I_c$  results were different. This indicates that in order for various laboratories to arrive at the same  $I_c$  results, a more detailed unification of the measurement techniques would be required. However, this would not insure the correctness of the results. If, for example, all of the participants of this study would have used a continuous coat of epoxy to bond their samples, the results may have been in close agreement but the  $I_c$  results would have been lowered by the increased conductor pre-strain. A unified definition of the desired measurement is required in order to make a correct measurement. Hopefully, a future joint publication will address some of these issues and result in a simple measurement method that has only the restrictions necessary for accuracy.

#### Acknowledgments

The authors extend their thanks to J. W. Ekin for discussions on these results, to R. M. Folsom, and T. C. Stauffer for sample preparation, data reduction, and plotting, to D. L. Rule for help with data plotting, to W. E. Look for assistance with the magnetic field calibration, and to all 22 laboratories that participated in these round robin measurements.

#### References

- [1] G. Fujii, J. W. Ekin, R. Radebaugh, and A. F. Clark, "Effect of Thermal Contraction of Sample Holder Material on Critical Current," *Adv. Cryog. Eng.-Materials*, Vol. 26, 589, Plenum Press, New York (1980).
- [2] G. Fujii, M. A. Ranney, and A. F. Clark, "Thermal Expansion of Nb<sub>3</sub>Sn and V<sub>3</sub>Ga Multifilamentary Superconducting Cables, Fiberglass-Epoxy and Cotton-Phenolic Composite Materials," *Jap. J. Appl. Phys.* 20, L267-L270 (1981).
- [3] A. F. Clark, G. Fujii, and M. A. Ranney, "The Thermal Expansion of Several Materials for Superconducting Magnets," *IEEE Trans. Mag. MAG-17*, 2316-2319 (1981).
- [4] J. W. Ekin, "Strain Scaling Law for Flux Pinning in Practical Superconductors. Part 1: Basic Relationship and Application to Nb<sub>3</sub>Sn Conductors," *Cryogenics* 20, 611 (1980).

## V. CRITICAL CURRENT MEASUREMENT SYSTEM

S. L. Bray and L. F. Goodrich

Power supply modifications to reduce the amount of current ripple and thus improve the overall accuracy and precision of critical current measurements were made. Also, additional modifications were made to systematically study the effect of power-supply current ripples. These circuit designs and innovations will be useful for and applicable to critical current measurements of all kinds.

In order to measure the critical current of superconductors, a high output current supply is required. In addition to high current capability, the supply should be designed to reduce ground loop problems, respond linearly to an input control signal, and minimize output noise. A current supply having these qualifications has been constructed and tested [1]. In addition to its normal operation as a constant-current source, two other unique modes of operation have been developed and tested. In one mode, the supply is used as a source of dc biased ac currents for testing the effect of dc-power-supply ripple on critical current measurements [2]. In the other mode, the supply is used in conjunction with a larger and noisier current source to form a hybrid supply. In the hybrid system, the smaller supply is used to increase the current output while actively filtering the noise output of the larger supply. Finally, systems for rapid quench (thermal runaway of the sample into the normal state) detection and supply reset have been incorporated in the design. The purpose of a quench detector is to prevent damage to the sample due to resistive heating. The specifics of all designs, modes of operation, and performance results are given.

### Low-Ripple Current Supply

This is an experimental design that has been gradually developed through continuous modification and improvement for an explicit application. Consequently, the specifics of the design should be considered quite flexible depending on the particular application. The performance of the circuit under different load conditions and with various input signals is being evaluated. Although the only application for which this supply has been tested is superconductor measurement, many other possible uses for a current supply of this type may exist.

The basic circuit is a voltage controlled current source (see Fig. 1) consisting of three main stages: input, control, and power. The principal power source for the supply is a 4 V battery consisting of two 1350 A-h 2 V wet cells. This 4 V battery supplies the output current through the power stage of the supply. Also, two 6 V wet cell batteries are used to power the control stage and a 115 Vac/15 Vdc supply is used at the input stage of the supply circuit. The power stage of the circuit utilizes six Darlington transistor pairs in parallel, with each pair consisting of a 25 A (T3) and a 300 A (T4) power transistor. Each of the 300 A transistor emitters is connected to the positive bus bar through a separate 1 mΩ resistor. The resistors provide the required current-proportional feedback signals for the control stage. The collectors of these transistors are all connected to the 4 V battery through a

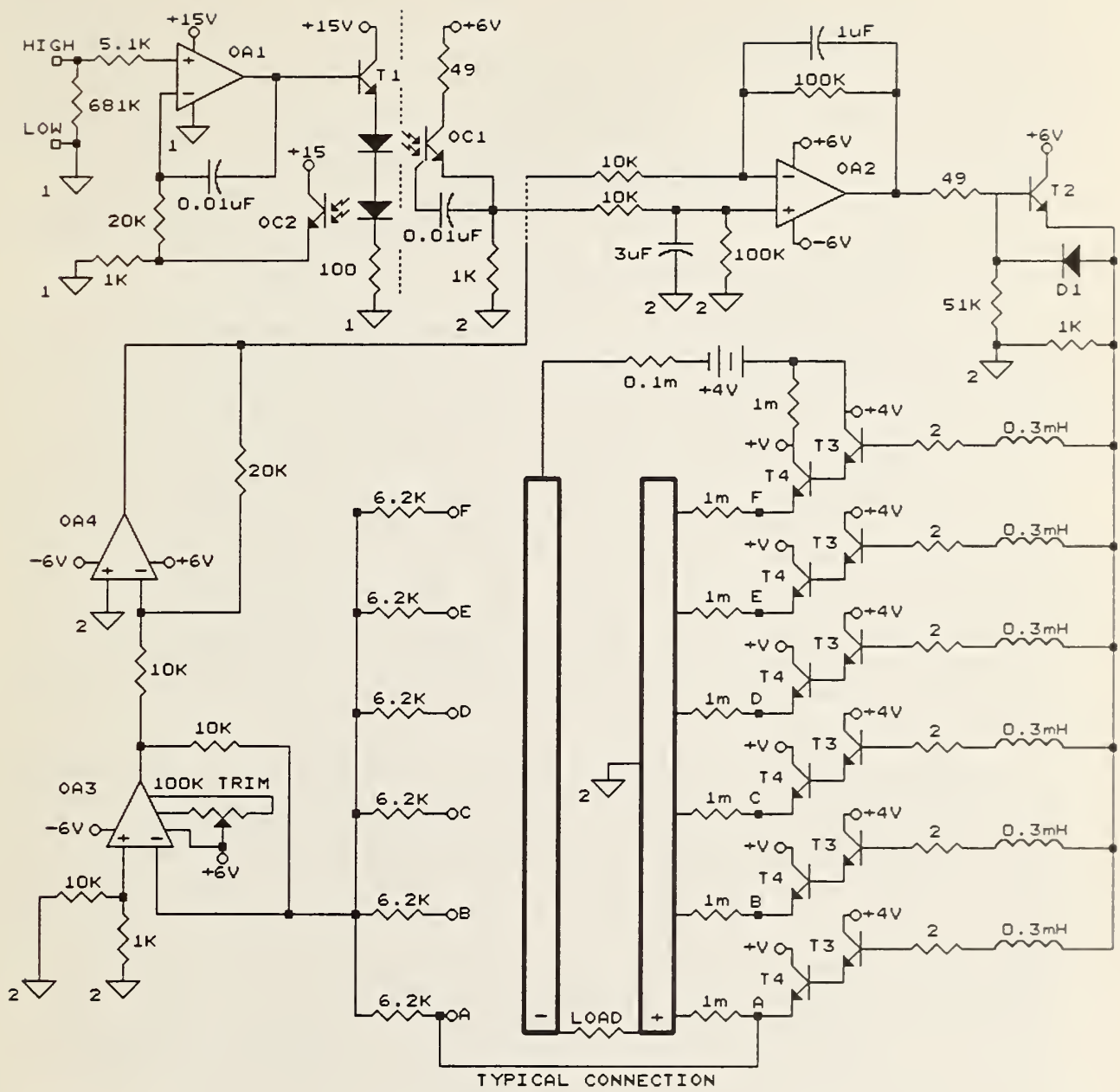


Fig. 1. Circuit diagram of the battery powered current supply in the low noise mode.

single 1 mΩ current limiting resistor. The collectors of the 25 A transistors are all connected directly to the 4 V battery and the bases are each connected to a series combination of a 0.3 mH inductor and a 1 Ω resistor. These inductors and resistors are beneficial in stabilizing the circuit with respect to parasitic oscillation. The opposite ends of the inductors are connected together, forming a branch point. The emitter of another 25 A (T2) transistor is connected to this branch point and provides the current to drive the Darlington pairs. This transistor amplifies the output signal from the control circuit. A 0.1 mΩ resistor connected between the negative battery terminal and the negative bus bar provides a current-proportional voltage signal for measuring the total current output of the supply.

The control stage of the circuit is based upon an operational amplifier (OA2) that compares the signal from the input stage with the feedback signal from the Darlington emitter resistors and applies the resulting signal to the power stage. In the feedback path, another operational amplifier (OA3) is used as a summing amplifier in order to combine and amplify the six signals from the feedback resistors. In order to avoid an offset current from the supply when the input signal is at zero volts, a trim potentiometer is used on this op-amp. This potentiometer is adjusted such that the normal output of the op-amp is slightly negative. This, in turn, results in a negative output signal from the comparator (OA2) and, thus, no offset current from the supply. Since the summing amplifier inverts the feedback signal, another inverting amplifier (OA4) is required in the feedback path to restore the polarity of the signal. The resulting signal is then sent to the inverting input of the comparator. The comparator uses a feedback capacitor to reduce the ac gain and, thus stabilize the circuit.

The main function of the input stage is to provide electrical isolation between the input signal generator and the supply circuit in order to avoid ground loop problems [3]. This isolation is achieved through the use of an optical isolator, or optocoupler (OC1). The input stage is linearized in a manner similar to that of the control stage (see page 66 of [3]). Again, a comparator (OA1) is used to compare the reference and feedback signals. The output signal from the comparator is amplified by a single transistor (T1). The feedback signal is supplied by a second optocoupler (OC2) which is in series with the first. This is necessary in order to provide electrical isolation. Moreover, the second optocoupler imitates the first and, thus, generates an appropriate feedback signal without electrically coupling the input and control stages. It is important to note that separate power supplies are used on each side of the isolation boundary (vertical dashed line on circuit diagram). Again, this avoids electrical coupling of the stages. The feedforward optocoupler (OC1) was found to be a significant noise source because of an unused base terminal which was picking up 60 Hz noise. This problem was greatly reduced by connecting this unused base terminal to the emitter terminal with a 0.1 μf capacitor.

The performance in this low current ripple mode of operation was tested with two load resistances. In the first case a low-inductance, 50-mΩ load (twisted wire) was used. This relatively large load resistance limited the output current to 20 A, but it also resulted in a sufficiently large current-proportional voltage signal for accurate measurement of the current ripple.

The peak-to-peak current ripple was 0.01 A at 20 A output current. In the second case a load resistance on the order of 1 mΩ was used to allow the supply to be operated to high currents. The voltage signal from a 0.1 mΩ resistor was used to measure the current ripple. For this case, the measured peak-to-peak current ripple was about 0.05 A for output currents from 10 to 900 A. The actual current ripple may be less than this but, because of residual voltage amplifier noise, this was the limit of this measurement.

#### Quench Detector with Rapid Reset

The control stage of the current supply contains several reactive elements that enhance stability and reduce noise. These elements, however, result in a time lag between the input signal and the supply's response. Traditionally, sample quench protection has been achieved by amplifying the sample voltage [4] and using this signal to reset the control signal generator in the event of a quench. However, this time lag between control signal reset and current interruption is great enough to jeopardize the sample. Consequently, a method for rapid current interruption was devised and implemented. Figure 2 is a schematic diagram of the quench protection circuit. This circuit is a combination of an adjustable amplifier stage, an absolute value stage, an inverter, an electronic timer, a single transistor current amplifier, and an optically coupled output stage. The amplified sample voltage is input to the absolute value stage which accommodates bipolar sample currents. The inverter provides the required high-to-low transition for the electronic timer. The timer holds the protection circuit output in the high state long enough to insure that the control signal generator will be reset. The current amplifier drives the output stage and the output stage provides electrical isolation between the quench protection circuit, the control signal generator, and the current supply. The signals sent to the control generator and the current supply by the quench protection circuit are high-to-low resistance transitions. In the case of the current supply, this output is connected between the base of transistor T2 (Fig. 1) and ground. The transition from high to low resistance, thus, interrupts the supply current by driving T2 into cutoff.

This circuit is capable of interrupting the supply current in approximately 50 μs, which is more than adequate for insuring sample protection.

#### ac and dc Current Supply

In order to test the effect of dc-power-supply ripple on critical current measurements [2], the basic current supply was modified to allow the generation of dc biased ac currents. There were two basic areas of modification.

First, the circuit had to be altered to accommodate simultaneous control by two separate input signals, a linear ramp and a sinusoid. The ramp signal provided the dc offset current while the sinusoid provided the ac ripple current. Figure 3 is a schematic diagram of the circuit used to generate the composite control signal. The two signal generators, ramp and ac, are isolated from one another by unity gain operational amplifiers, OA1 and OA2. The two input signals are then combined by the inverting summer, OA3. Another inverting summer, OA4, is used to restore the polarity of the signal

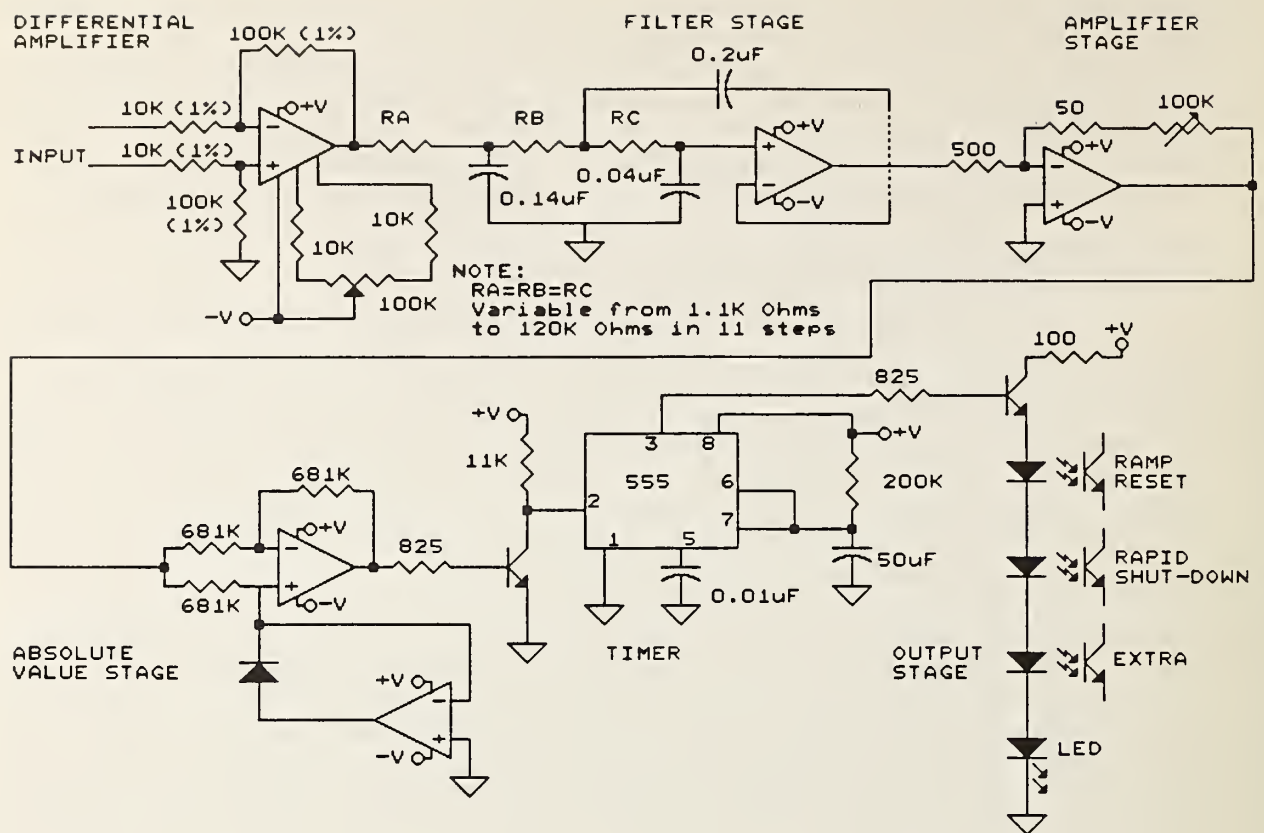


Fig. 2. Quench detector circuit with rapid shut-down of the current supply.

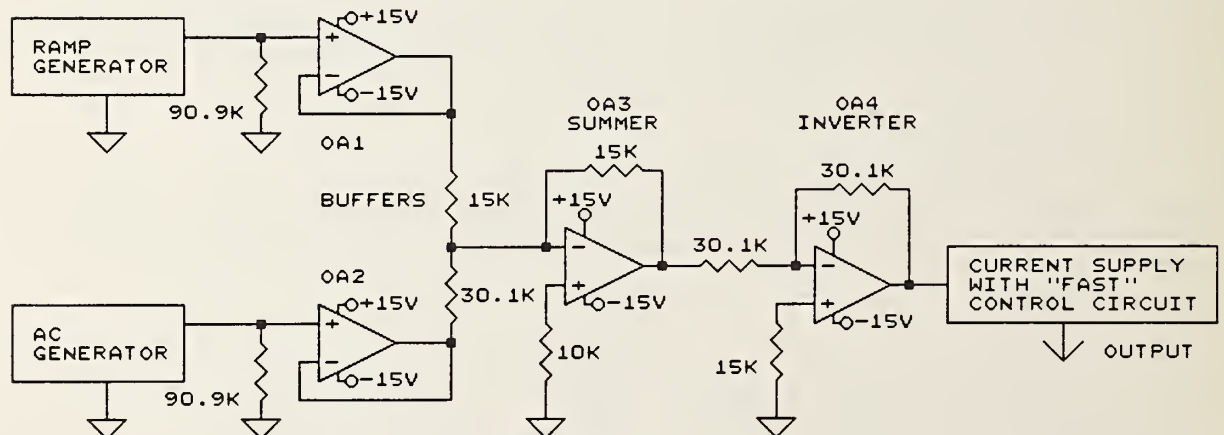


Fig. 3. Schematic diagram of the ac and dc current supply.

This signal is then applied to the input of the current supply's control circuit.

The second modification involved the ac response of the control circuit. The basic control circuit described above contains several filtering elements that are useful for noise reduction and stability; however, these elements greatly attenuate the desired ac output current in this mode of operation. Consequently, these filtering elements were altered to enhance the ac response of the supply. The resulting increase in current noise was insignificant in comparison with the deliberately generated ac current and, thus, was not considered detrimental in this application. Specifically, the  $0.01 \mu\text{F}$  feedback capacitor connected between the inverting input and the output of OA1 (see Fig. 1) was reduced to  $82 \text{ pF}$ . Also, the  $0.01 \mu\text{F}$  capacitor connected between the base and emitter of OC1 was removed. The  $3 \mu\text{F}$  capacitor connecting the inverting input of OA2 to common was reduced to  $0.02 \mu\text{F}$ . Finally, the  $1 \mu\text{F}$  feedback capacitor connected between the inverting input and the output of OA2 was reduced to  $0.1 \mu\text{F}$ . These changes gave the desired increase in ac response while maintaining stability. The intrinsic (no input ac voltage control signal) current ripple in this mode was about  $0.5 \text{ A}$  peak-to-peak for dc output currents from  $0$  to  $400 \text{ A}$ .

In this mode of operation, the maximum tested frequency was  $10 \text{ kHz}$ , ac amplitude was  $275 \text{ A}$  peak-to-peak, and dc bias was  $400 \text{ A}$  (not all at the same time). Moreover, the maximum output voltage of the current supply is limited to less than  $4 \text{ V}$  by its battery voltage, the impedance of the current path between the battery and the load, the collector-emitter saturation voltage of the output transistors, the dc and ac levels of the output current, and by the frequency of the output current. If the impedance of the load and the ac and dc output current levels are such that the load voltage reaches the maximum available output voltage, saturation results. In these particular tests measures were taken to reduce the load impedance and, thus, extend the operating limits of the supply.

### Hybrid Supply

Although the low noise character of the battery powered current supply is very desirable for critical current measurements, its most notable limitation, particularly for large conductor measurements, is its maximum output capability of approximately  $950 \text{ A}$ . Unfortunately, high output commercially available current supplies often have high noise levels that limit their suitability for critical current measurements. In light of this, a method for using the battery powered supply in conjunction with a larger current supply to form a high output and low noise hybrid supply has been developed and tested.

The high-current supply that was used in these tests is a  $3000 \text{ A}$ , three phase, SCR switching supply. Like the battery supply, this supply is controlled by an external input signal and uses feedback to maintain a linear input-output relationship. Unlike the battery supply, the  $3000 \text{ A}$  supply has a substantial output noise level. This noise is predominantly harmonics of  $60 \text{ Hz}$  and has a peak-to-peak amplitude of  $144 \text{ A}$  ( $36 \text{ A rms}$ ) at a dc output of  $3000 \text{ A}$ . The relationship between the peak-to-peak and rms values will not be

the usual one because the noise is not sinusoidal. This noise level is sufficiently large to cause errors in dc critical current measurements [2].

Figure 4 is a block diagram of the hybrid current supply. As shown, the control circuits of both the battery supply and the 3000 A supply receive two input signals, one from the ramp generator and one from the 3000 A shunt resistor. The ramp signal controls the dc current from each supply and the shunt resistor provides feedback signals. In the case of the 3000 A supply, this feedback signal is simply used to maintain a linear input-output relationship. The feedback signal sent to the battery control circuit encounters a dc blocking capacitor that allows only the ac, or noise, portion of the signal to pass. This noise signal is inverted and combined with the ramp signal to control the output of the battery supply. As indicated in the diagram, the two supplies are connected in parallel and, therefore, the total current output is the sum of the individual supply outputs. Since the two supplies put out similar noise signals that are of opposite polarity, this summation tends to cancel the total output noise from the hybrid supply.

In order for the battery supply to simultaneously decrease the noise output and increase the dc output of the 3000 A supply a different control circuit than those previously described was required. Ideally, in this application, the battery's behavior should be as follows. As the ramp input signal becomes nonzero, the output current from the battery supply abruptly increases from zero to a relatively low dc bias level in order to allow ac currents without clipping (the battery supply is unipolar and can only produce positive currents). As the output current from the 3000 A supply increases, its noise level also increases and the resulting negative feedback signal to the battery supply causes its output to reduce this noise. Finally, as the 3000 A supply nears its peak output, the battery supply's dc output ramps quickly to its peak value such that both supplies reach their peak output levels simultaneously. This complex behavior of the battery supply is only necessary in order to limit its duty cycle. Otherwise, the battery supply could be held at peak output (less the required ac peak output) throughout the majority of the 3000 A supply's ramp cycle. The battery control circuit was designed to minimize the supply's output at all times and, thus, prolong discharge of the battery cells. It is important to note that this nonlinear behavior of the battery supply does not result in a nonlinear output from the hybrid supply. This is due to the fact that the battery supply is contained within the 3000 A supply's control loop. In other words, the 3000 A supply compensates for nonlinear variations in the battery supply's contribution to the total output current.

Figure 5 is a diagram of the control circuit used to achieve this nonlinear behavior. Beginning at the output side of the control circuit, the original power circuit of Fig. 1 is driven by the output of an optical isolator (nonlinear). The isolator is driven by an inverting summer which combines three input signals. The first input signal is the 3000 A shunt resistor feedback signal as described above. The second signal is a constant voltage obtained from a Zener diode. The gain of the amplifier that drives the Zener diode is high in order to insure early zener breakdown. This signal provides the current-bias. The potentiometer that is connected to the Zener diode allows adjustment of the bias-current level. The input to the bias

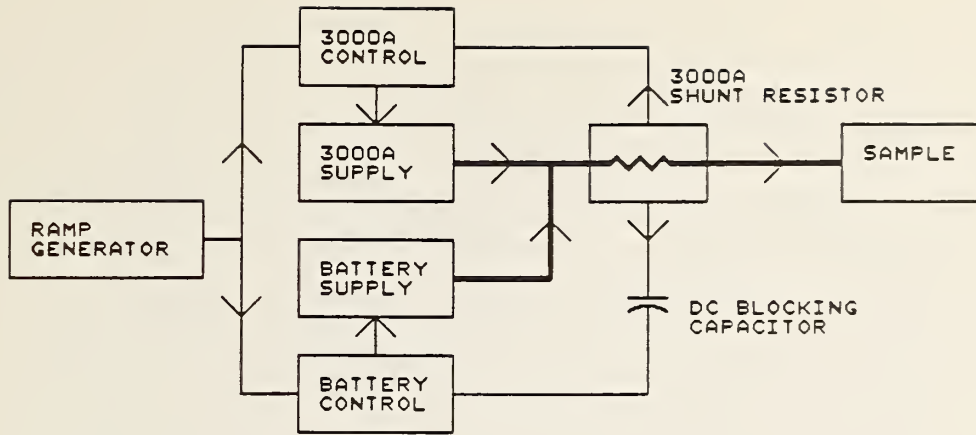


Fig. 4. Block diagram of the hybrid current supply.

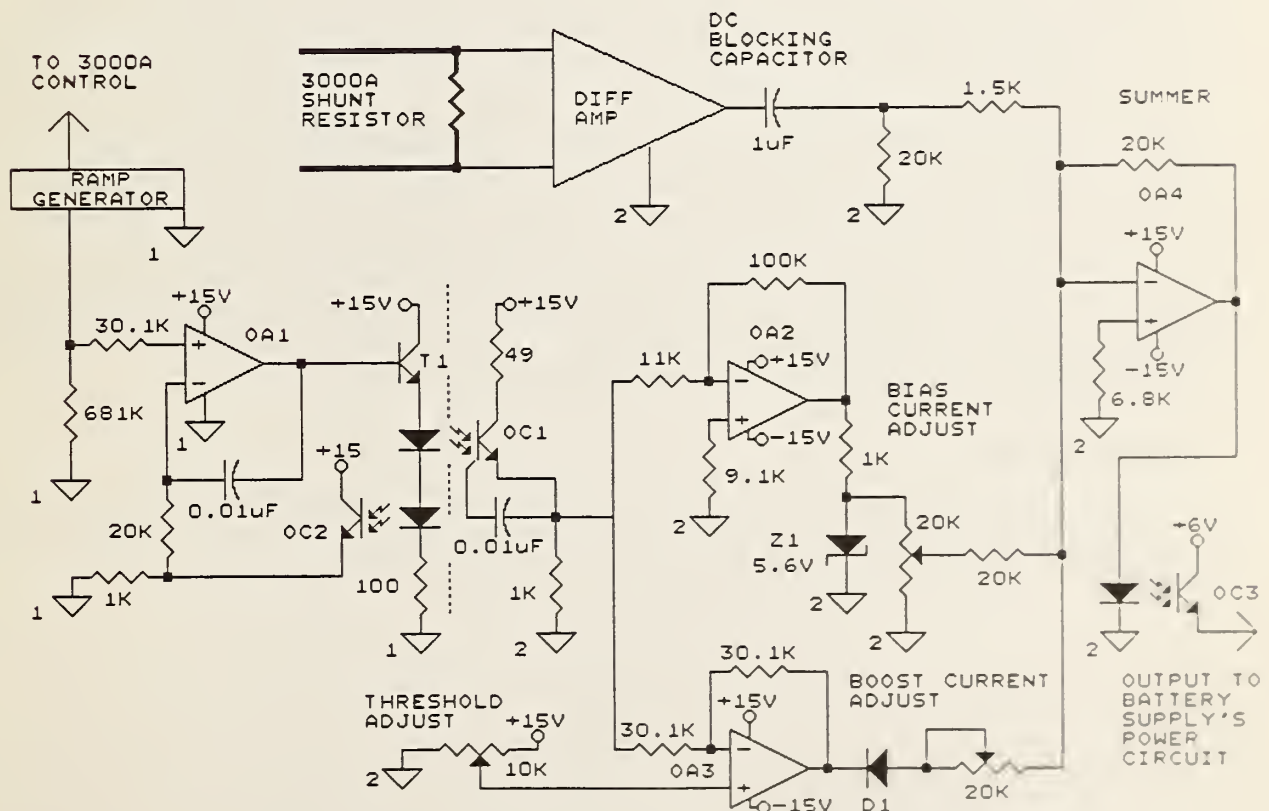


Fig. 5. Schematic diagram of the control circuit used to filter and boost the current.

portion of the control circuit comes from the ramp generator through an optical isolator. The third input signal to the summer is the current boost signal. In this case, the output potentiometer provides adjustment of the current gain or, in other words, determines the ramp rate of the battery supply output. The signal to the potentiometer is provided by an inverting amplifier that has an adjustable threshold voltage. This threshold voltage determines the point at which the boost current begins its ramp cycle. The diode between the current boost potentiometer and the amplifier blocks the positive polarity signal that would result from the threshold voltage being greater than the input voltage. Again, the input voltage is provided by the ramp generator. The threshold and current gain adjustments must be made in a coordinated manner such that the battery supply peaks in unison with the 3000 A supply. When the circuit is adjusted correctly, the result is a low noise linear ramp current that peaks near 4000 A. The peak-to-peak noise level of the composite supply has been measured at 17.6 A (3.5 A rms) for an output of 3000 A. This is a 88% reduction in the peak-to-peak noise and a 90% reduction in the rms noise.

#### Battery Supply Protection

The battery powered current supply was not designed for continuous operation at its maximum current level. Its duty cycle is limited by the maximum power dissipation of the 300 A output transistors and the 1 mΩ collector resistor of Fig. 1. Consequently, a method of overcurrent protection that uses thermal cutoff switches on both the collector resistor and the output transistors has been designed. Referring to Fig. 6, under normal operating conditions all four thermal cutoff switches (TC1-TC4) are in the closed position. This holds the 12 V relay in a position that connects the Darlington output stage to the control signal amplifier, T2. If the temperature of any one of the four thermal cutoffs exceeds its set point, the relay current is interrupted and the relay switches to the other position. In this position, input to the Darlington output stage is connected to common and the output current is interrupted. The diodes in series with the relay current are used to prevent undesired relay energization in the unlikely case where two shorts between the 4 V battery and the thermal cutoff switches occur thus preventing the current interruption from occurring. These modifications are now under way and will be tested upon completion.

#### Acknowledgments

The authors extend their thanks to W. P. Dube for numerous discussions and being a constant source of advice, to R. M. Folsom for creating circuit diagrams, and to H. E. Spilman for circuit testing.

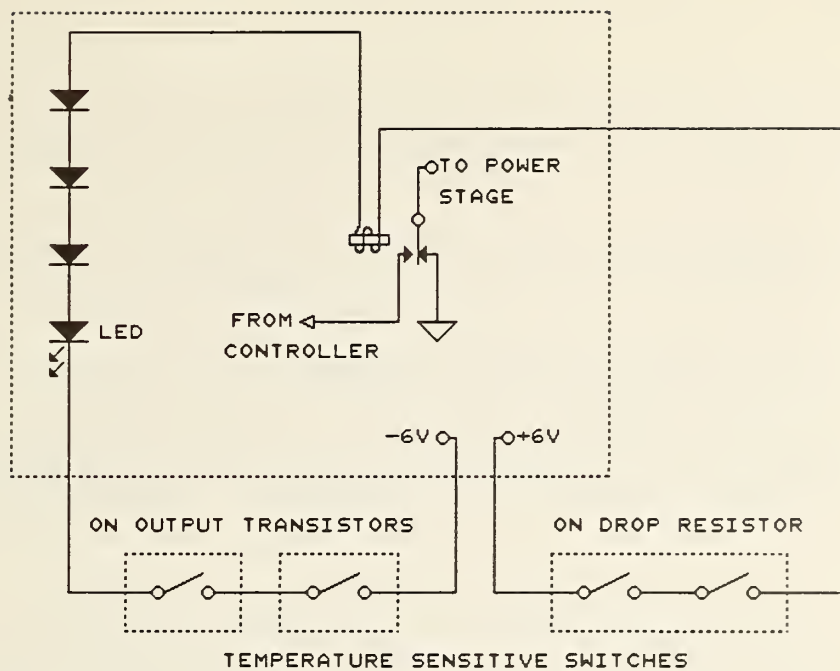


Fig. 6. Schematic diagram of the protection for the current supply.

## References

- [1] L. F. Goodrich, S. L. Bray, W. P. Dube, E. S. Pittman, A. F. Clark, "Development of Standards for Superconductors, Interim Report Jan.-Dec. 1985," NBSIR 87-3066, National Bureau of Standards, Boulder, Colorado (April 1987).
- [2] L. F. Goodrich, S. L. Bray, and A. F. Clark, "Current-Ripple effect on Superconductive DC Critical Current Measurements," *Adv. Cryo. Eng.-Materials*, Vol. 34, pp. 1019-1026, Plenum Press, New York (1988).
- [3] Ralph Morrison, Grounding and Shielding Techniques in Instrumentation, (John Wiley & Sons, New York, 1977).
- [4] W. P. Dube and L. F. Goodrich, "Quench detector Circuit for Superconductor Testing," *Rev. Sci. Instrum.*, 57, 680-682 (1986).

## VI. MAGNETIC EVALUATION OF Cu-Mn MATRIX MATERIAL FOR FINE-FILAMENT Nb-Ti SUPERCONDUCTORS

R. B. Goldfarb and D. L. Ried  
National Bureau of Standards, Boulder, Colorado 80303

T. S. Kreilick and E. Gregory  
Supercon, Inc., Shrewsbury, Massachusetts 01545

### Abstract

Copper-manganese alloys have been proposed as matrix material for the reduction of coupling losses in fine-filament Nb-Ti superconductor wires. Magnetization and susceptibility measurements show that adverse magnetic effects arising from the spin-glass properties of this matrix are minimal for concentrations of Mn up to at least 4 percent.

### Introduction

The addition of Mn to the Cu matrix of fine-filament Nb-Ti superconductors has been recently shown to reduce proximity-effect coupling between closely spaced filaments [1,2]. Small interfilament separation promotes the formation of filaments with uniform diameter [3,4], thus avoiding the deleterious effects of "sausaging" [5]. The result is a large total Nb-Ti cross section (and therefore a large critical current for the composite wire) with small filament diameters (to minimize hysteresis losses). In the absence of Mn, coupling losses can offset the reductions in hysteresis losses that are achieved by using fine filaments. The reduction in coupling is thought to be caused by magnetic scattering of electron pairs by the Mn moments [1,2,6,7] rather than simply the increased electrical resistivity of the matrix [1,8].

Copper-manganese, the proposed matrix alloy, is a classical spin glass, characterized by magnetic viscosity and anisotropy that develop below a "spin-freezing" temperature. Several review articles on spin glasses have been published [9-17]. Spin-glass effects could result in hysteresis loss and remanent magnetization in composite superconductors, features that could counteract the reduction in loss due to the Mn additions.

We have examined some of the magnetic properties of Cu-Mn alloys with Mn content in the range 0.16 to 3.75 mass percent (wt.%) to determine whether spin-glass effects could impair the performance of fine-filament Nb-Ti conductors. It appears that, for Mn content in this range, the adverse magnetic properties of the matrix are not significant.

### Spin-Glass Properties

A spin glass exhibits a peak in magnetic susceptibility as a function of temperature which is associated with a "freezing" of magnetic moments. Freezing is a relative concept, depending on magnetic field strength and time, in addition to temperature [18]. Above the freezing temperature,  $T_f$ , the alloy behaves paramagnetically [19], sometimes with large moments. Near and

below  $T_f$ , magnetic relaxation effects appear [20]. In this paper, we do not discuss the time (or frequency) dependence of the magnetic properties.

Applying a magnetic field to a sample at 4 K results in an isothermal remanent magnetization, IRM, measured after reducing the field to zero. The IRM is a function of the maximum applied field. Cooling the samples from above  $T_f$  to 4 K in a field, and then reducing the field to zero, gives a thermoremanent magnetization, TRM. The TRM is also a function of field. For a large enough experimental field, the IRM will equal the TRM [21]. Fine details of the hysteresis loops of magnetization vs. field near the origin for dilute Cu-Mn alloys are discussed in Refs. [22] and [23].

Spin glasses have three properties that might affect their suitability for use as matrix material for multifilamentary superconductors. The magnitude of each of these effects would be a function of the volume of the matrix that contained the Mn, usually just the interfilamentary space.

First, large magnetic moments could produce a significant magnetization at high fields. The field profile of a superconducting magnet could be distorted if it were made with wire containing such matrix material.

Second, if the operating temperature of the wire is below  $T_f$ , there could be a large IRM in the matrix material after the superconducting magnet is cycled to high fields. (The direction of the IRM would be the same as that of the trapped flux in the superconductor.) Third, if the magnet were intended to be cycled, hysteresis in the matrix material could be a problem. These last two possibilities could partially defeat the purpose of using wire with fine filaments.

(The field-cooled unidirectional anisotropy at 4 K in Cu-Mn is not fixed very well compared to other spin glasses; it can be switched by moderate fields. As a consequence, there is a symmetrical hysteresis loop after exposure to moderate fields. It is a "false" hysteresis due to the switching of the unidirectional anisotropy as the field is cycled. The reader interested in this point is referred to Refs. [21] and [24].)

#### *Proximity Effect*

Proximity-effect coupling arises when interfilament separation is on the order of the coherence length,  $\xi$ , in the matrix (approximately equal to the electron-pair decay length in the "dirty limit"). Manganese additions to the matrix cause magnetic scattering of the electron pairs and a reduction in  $\xi$ . In the spin-glass state, however, there appear to be two opposing tendencies [6]. On the one hand, the freezing of the Mn spins is thought to inhibit electron scattering, tending to increase  $\xi$ . On the other hand, the exchange interactions in the spin-glass state could enhance electron-pair breaking, thereby reducing  $\xi$ . The latter effect appears to dominate and, generally,  $\xi$  is inversely proportional to Mn content [6].

## Measurements

Measurements were made on Cu-Mn alloys containing 0.16, 0.72, 2.00 and 3.75 wt.% Mn (0.19, 0.83, 2.31, and 4.31 at.% Mn). Manganese content was checked by dc plasma emission spectroscopy by an independent laboratory, which reported 0.21, 0.80, 2.15, and 3.68 wt.% Mn. We will use the manufacturer's chemical compositions. The alloys were melted in a vacuum induction furnace in an Ar atmosphere. The ingots were machined to a diameter of 6 cm, preheated to 816°C, hot-extruded to 1.9 cm diameter, cold drawn to 3.2 mm diameter, and annealed in Ar for 1 h at 650°C. Samples were cut into cylinders, about 1.5 cm in length, 3.2 mm in diameter.

### *Susceptibility vs. Temperature at Low Field*

The ac susceptometer was a two-position, mutual-inductance type [25]. Susceptibility was measured along a sample's axis as a function of increasing temperature in an 80 A/m (1 Oe) rms, 10 Hz field. Eddy-current contributions to the susceptibility signal were negligible for the thin samples at this low frequency. No demagnetization factor corrections were necessary. A typical susceptibility curve for one of the samples is shown in Fig. 1. Peaks in the susceptibility curves gave the spin-freezing temperatures,  $T_f$ , and maximum volume susceptibility values at  $T_f$ , in Table I.

For comparison, we refer to the careful susceptibility measurements on Cu-Mn single crystals by Nagata et al. [26] They measured  $T_f$  values of 9.90 and 14.67 K, and effective magnetic moments of Mn of 4.80 and 4.86  $\mu_B$ , for 1.08 and 2.02 at.% Mn, respectively. (Similar effective moments are given in Refs. [27] and [28] for other concentrations of Mn.)

The susceptibilities in Table I are not insignificant. They exceed, for example, the susceptibilities of many austenitic stainless steels [29-31]. Even at these levels, however, the susceptibility of the Cu-Mn matrix should not adversely affect superconductor performance. However, since  $T_f$  is above the boiling temperature of helium for all except the 0.16 wt.% Mn alloy, the low-temperature magnetization-vs.-field behavior of these samples is examined.

### *Magnetization vs. Field at 4 K*

Magnetization measurements of the 0.72, 2.00 and 3.75 wt.% Mn alloys were made as a function of field at 4 K with a vibrating-sample magnetometer. We report measurements of magnetization at 5.6 MA/m (70 kOe, referred to below as "7 T", the magnetic flux density in free space), hysteresis loss for cycled fields, and remanent magnetizations at zero field. The results are summarized in Table II.

At the maximum applied field of 7 T, the 3.75 wt.% Mn sample had a magnetization of 44 kA/m, greater than that of many austenitic steels. This suggests that there could be some field distortion due to the matrix material if it were used in the manufacture of superconducting magnets. The magnetizations of the 2.00 and 0.72 wt.% Mn samples at 7 T were 26 kA/m and 11 kA/m, respectively, with much less potential for problems. Characteristic of spin glasses, the magnetization curves were far from saturation at 7 T.

The hysteresis losses per 7-T field cycle are small. Compared to typical hysteresis in multifilamentary conductors, about  $100 \text{ kJ/m}^3$  ( $10^6 \text{ erg/cm}^3$ ), the losses are negligible. For the 3.75 wt.% Mn sample, the loss is approximately  $10 \text{ kJ/m}^3$ . For the 2.00 and 0.72 wt.% Mn alloys, the losses are about 4 and 0.4  $\text{kJ/m}^3$ , respectively. In applications where the field direction is not reversed, there will be virtually no hysteresis.

Reducing the field to zero with the samples at 4 K allows the IRM to be measured. For the 3.75 wt.% Mn sample, the IRM gets no larger than  $1.8 \text{ kA/m}$  once the maximum field per cycle exceeds  $2.4 \text{ MA/m}$ . For the 2.00 and 0.72 wt.% Mn samples, the values of IRM get no larger than  $600$  and  $80 \text{ A/m}$ , respectively, for smaller maximum fields. Similar remanent magnetizations at 4 K have been reported by others [27,32,33]. Even for the 3.75 wt.% Mn alloy, the IRM is small.

Cooling the samples from above  $T_f$  to 4 K in the field, and then reducing the field to zero, gives the TRM. For a 7-T cooling field, the TRM values approximately equaled the IRM values noted above.

### Conclusion

Spin-glass properties of Cu-Mn alloys have the potential to impair superconductor performance when they are used as the matrix material for fine-filament Nb-Ti wires. For the case of dilute alloys, with less than 4% Mn, the effects are minimal.

The main concern is possible distortion of the superconducting-magnet field profiles when matrix material containing 3.75 wt.% Mn (or more) is used. A lesser concern is that there will be a small remanent magnetization owing to the matrix material when the wire is cycled to high field at low temperatures. Hysteresis losses are insignificant.

### Acknowledgments

R. L. Spomer assisted with some of the measurements. E. W. Collings made several helpful comments and suggestions on the manuscript. This work was supported, at NBS, by the Department of Energy, Office of Fusion Energy and Division of High Energy Physics, and at Supercon, by the Department of Energy, Small Business Innovation Research Program.

## References

- [1] E. W. Collings, *Adv. Cryo. Engr. (Materials)* 34, 867 (1988).
- [2] T. S. Kreilick, E. Gregory, J. Wong, R. M. Scanlan, A. K. Ghosh, W. B. Sampson, and E. W. Collings, *Adv. Cryo. Engr. (Materials)* 34, 895 (1988).
- [3] E. Gregory, T. S. Kreilick, J. Wong, A. K. Ghosh, and W. B. Sampson, *Cryogenics* 27, 178 (1987).
- [4] T. S. Kreilick and E. Gregory, *Cryogenics* 27, 401 (1987).
- [5] J. W. Ekin, *Cryogenics* 27, 603 (1987).
- [6] J. Niemeyer and G. von Minnigerode, *Z. Physik B* 36, 57 (1979).
- [7] D. K. Finnemore, H. C. Yang, V. G. Kogan, and S. L. Miller, *Adv. Cryo. Engr. (Materials)* 30, 909 (1984).
- [8] T. S. Kreilick, E. Gregory, J. Wong, *J. Less Common Metals* (1988), in press.
- [9] G. Heber, *Appl. Phys.* 10, 101 (1976).
- [10] J. A. Mydosh, *Am. Inst. Phys. Conf. Proc.* 24, 131 (1975).
- [11] J. A. Mydosh, *J. Magn. Magn. Mater.* 7, 237 (1978).
- [12] P. A. Beck, *Prog. Mater. Sci.* 23, 1 (1978).
- [13] K. H. Fischer, *Phys. Stat. Sol. B* 116, 357 (1983).
- [14] K. H. Fischer, *Phys. Stat. Sol. B* 130, 13 (1985).
- [15] C. Y. Huang, *J. Magn. Magn. Mater.* 51, 1 (1985).
- [16] K. Moorjani and J. M. D. Coey, *Magnetic Glasses*, Amsterdam: Elsevier, 1984, Ch. 7.
- [17] D. Chowdhury, *Spin Glasses and Other Frustrated Systems*, New Jersey: Princeton University, 1986.
- [18] R. B. Goldfarb, K. V. Rao, and H. S. Chen, *Solid State Comm.* 54, 799 (1985).
- [19] A. F. J. Morgownik and J. A. Mydosh, *Phys. Rev. B* 24, 5277 (1981).
- [20] C. N. Guy, *J. Appl. Phys.* 50, 7308 (1979).
- [21] R. W. Knitter, J. S. Kouvel, and H. Claus, *J. Magn. Magn. Mater.* 5, 356 (1977).
- [22] C. N. Guy, *J. Phys. F: Met. Phys.* 12, 1453 (1982).
- [23] P. Monod, J. J. Préjean, and B. Tissier, *J. Appl. Phys.* 50, 7324 (1979).
- [24] P. A. Beck, *Phys. Rev. B* 33, 3585 (1986).
- [25] R. B. Goldfarb and J. V. Minervini, *Rev. Sci. Instrum.* 55, 761 (1984).
- [26] S. Nagata, P. H. Keesom, and H. R. Harrison, *Phys. Rev. B* 19, 1633 (1979).
- [27] J. Owen, M. E. Browne, V. Arp, and A. F. Kip, *J. Phys. Chem. Solids* 2, 85 (1957).
- [28] J. M. Franz and D. J. Sellmyer, *Phys. Rev. B* 8, 2083 (1973).
- [29] E. W. Collings and S. C. Hart, *Cryogenics* 19, 521 (1979).
- [30] E. W. Collings and R. L. Cappelletti, *Cryogenics* 25, 713 (1985).
- [31] K. Pieterman, A. Ketting, and J. Ch. Geerse, *J. Physique (Colloq.)* 45, C1-625 (1984).
- [32] J. A. Careaga and R. Tournier, cited in J. Souletie and R. Tournier, *J. Low Temp. Phys.* 1, 95 (1969).
- [33] The conversion of magnetization from  $\mu_B$  per Mn atom to A/m for dilute Cu-Mn is:  $[\mu_B/\text{Mn}] \times [\text{at.\% Mn}] \times 7.854 \times 10^3 = [\text{A}/\text{m}]$ . For example, 0.0123  $\mu_B/\text{Mn}$  for 0.83 at.\% Mn corresponds to a magnetization of 80 A/m.

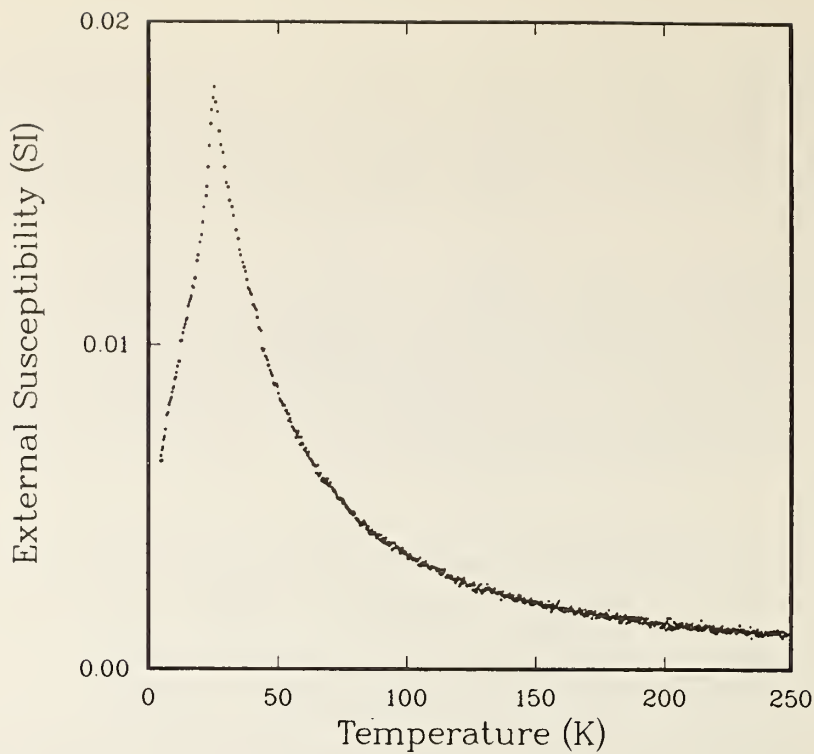


Figure 1. Volume ac susceptibility vs. temperature for Cu-3.75 wt.% Mn. The peak at 25.2 K corresponds to the spin-freezing temperature,  $T_f$ .

Table I. Spin-freezing temperatures ( $T_f$ ) and maximum volume susceptibilities ( $\chi_{\max}$ ) for dilute Cu-Mn alloys.

Wt.% Mn	At.% Mn	$T_f$ (K)	$\chi_{\max}$ (SI)	$\chi_{\max}$ (cgs)
0.16	0.19	< 4.0	$2.1 \times 10^{-3}$	$1.7 \times 10^{-4}$
0.72	0.83	9.2	$4.5 \times 10^{-3}$	$3.6 \times 10^{-4}$
2.00	2.31	18.0	$1.0 \times 10^{-2}$	$8.0 \times 10^{-4}$
3.75	4.31	25.2	$1.8 \times 10^{-2}$	$1.4 \times 10^{-3}$

Table II. High-field magnetization (M), hysteresis loss, and isothermal remanent magnetization (IRM), for dilute Cu-Mn alloys at 4 K.

Wt.% Mn	M at 7 T		Hysteresis		IRM	
	(kA/m) (G)	(kJ/m <sup>3</sup> ) (erg/cm <sup>3</sup> )	(kJ/m <sup>3</sup> ) (erg/cm <sup>3</sup> )	(kA/m) (G)	(kA/m) (G)	
0.72	12	150	0.4	$4 \times 10^3$	0.08	1
2.00	26	325	4.0	$4 \times 10^4$	0.6	8
3.75	44	550	10.0	$1 \times 10^5$	1.8	23

## VII. COUPLING LOSSES MEASURED BY VIBRATING-SAMPLE MAGNETOMETRY

R. B. Goldfarb

### Abstract

Coupling losses in multifilamentary superconductors may be measured with a vibrating-sample magnetometer by varying the waiting period before recording the magnetization signal after a field change. A Nb-Ti multifilamentary wire and a multistrand cable with different twist pitches were measured for different waiting periods. For wire with long twist lengths, coupling losses may be up to two times the hysteresis loss.

### Introduction

Coupling in multifilamentary superconductors refers to the tunneling of Cooper pairs from one superconducting filament to another through a normal-metal matrix, a phenomenon known as the proximity effect. These electron currents are induced by changes in applied field in an attempt to shield the composite conductor. They give rise to magnetic moments which may be detected by magnetometers based on vibrating a sample or on integrating flux [1].

Magnetic moments from coupling currents add to those from superconductor shielding and trapped flux to increase the area of a magnetization-vs.-field hysteresis loop. Unlike superconductor shielding currents, coupling currents decay with time. Thus the measured area of a hysteresis loop depends on the sweep rate of the field.

Measurements made by the integrated flux method [2] require a swept field. With increasing cycle time, the hysteresis loss remains constant, but the coupling loss decreases. The hysteresis loss may be isolated by extrapolation.

A vibrating-sample magnetometer may be used with either swept or stepped fields. The former method requires perfectly balanced pick-up coils to eliminate induced voltages from the changing applied field. Since balanced coils are difficult to realize, I use the latter quasistatic method. Sufficient waiting time is allowed between field steps for the superconducting field magnet to come to equilibrium and for coupling currents in the superconductor sample to decay. Thirty to 40 seconds are usually adequate for the lock-in amplifier to stabilize.

Typical methods for reducing coupling losses are to twist the multifilar conductors [3], increase the resistivity of the matrix, or add magnetic scatterers to the matrix [4]. In this note, I report on some measurements of magnetization as a function of field for a multifilamentary Nb-Ti conductor in several geometries to illustrate how coupling losses can be measured with a vibrating-sample magnetometer.

## Experiment

Samples were in the form of wires or flat woven cable. Some of the wire characteristics are given in Table I [5]. A thin Nb diffusion barrier was on the surface of each Nb-Ti filament. Wire samples were coiled in two layers around the threads of a size 10 nylon screw sample holder, about 4.5 mm in diameter. The magnetic field was applied approximately transverse to the wire, along the axis of the coil.

The cable was made with 30 strands of wire. A cable sample consisted of two carefully cut 4-mm segments with the field applied in the cable plane. Because of the transposition of the strands in the cable, the field was only approximately transverse to the individual strands. One wire sample was carefully cut into 4-mm segments, for comparison with the cable sample.

The wire stock had a twist length of 2.5 cm. In the cabling operation the twist length of each strand was increased somewhat. However, because the cable sample consisted of 4-mm segments, there was an "effective" twist length of 0.4 cm. For purposes of comparison, I further twisted some of the wire to a final twist length of 0.45 cm.

Measurements of magnetization as a function of field were made at 4 K, with maximum applied fields of  $\pm 800$  kA/m ( $\pm 10$  kOe, corresponding to a flux density in free space of  $\pm 1$  T). Each complete hysteresis loop was traversed in 60 equal steps per cycle. The waiting time between reaching a measurement field and recording the magnetization was either 40 or 90 seconds. The area enclosed by the loops equaled the total losses under these conditions.

Table II gives the total loss per sample volume (Nb-Ti plus matrix) for wires and cable, for different twist lengths and waiting times. It may be concluded from these data that the intrinsic hysteresis loss per cycle for this wire is  $31 \text{ kJ/m}^3$ . Additional losses, due to coupling, depend on time and twist-pitch. These coupling losses could amount to twice the hysteresis loss.

## Conclusion

Interfilamentary coupling losses may contribute to the losses measured by vibrating-sample magnetometry. They can be eliminated by sufficiently long waiting times between field steps or by cutting the sample in short segments. Short twist lengths are effective in reducing coupling losses in the actual wires.

## Acknowledgments

Wire and cable stock, and wire characteristics based on delivered material, were provided by R. M. Scanlan, Lawrence Berkeley Laboratory. The work was supported by the Department of Energy, Office of Fusion Energy and Division of High Energy Physics.

## References

- [1] A comparison of the advantages of each type of magnetometry is given in: R. B. Goldfarb and A. F. Clark, Adv. Cryo. Engr. (Materials) 32, 779 (1986).
- [2] W. A. Fietz, Rev. Sci. Instrum. 36, 1621 (1965).
- [3] G. H. Morgan, J. Appl. Phys. 41, 3673 (1970).
- [4] E. W. Collings, Adv. Cryo. Engr. (Materials) 34, 867 (1988).
- [5] This wire is described in: T. S. Kreilick, E. Gregory, and J. Wong, "The design and fabrication of strand for SSC magnet applications," ICEC11, G. Klipping and I. Klipping, eds., Butterworth, UK (1986) pp. 725-729. The billet number is Supercon 351E, alternately designated "LBL2". Cable identification is SC322.

Table I. Characteristics of Nb-Ti wire.

Number of filaments	4326
Filament diameter	6.3 $\mu\text{m}$
Edge-to-edge filament spacing	0.8 $\mu\text{m}$
Wire diameter	0.65 mm
Twist length	2.5 cm

Table II. Total loss for different twist lengths and waiting times.

Run number	Sample geometry	Twist length (cm)	Waiting time (s)	Loss per cycle ( $\text{kJ}/\text{m}^3$ )
1	Wire coil	2.5	40	91
2	Wire coil	2.5	90	58
3	Wire coil	0.45	40	31
4	Wire segments	0.4 *	40	31
5	Cable segment	0.4 *	40	32
6	Cable segment	0.4 *	90	32

\* "Effective" twist length equal to segment length.

Appendix A    From: ADVANCES IN CRYOGENIC ENGINEERING MATERIALS, Vol. 34  
Edited by A.F. Clark and R.P. Reed  
(Plenum Publishing Corporation, 1988)

CURRENT-RIPPLE EFFECT ON SUPERCONDUCTIVE DC CRITICAL CURRENT MEASUREMENTS\*

L. F. Goodrich, S. L. Bray, and A. F. Clark

Electromagnetic Technology Division  
National Bureau of Standards  
Boulder, Colorado 80303

ABSTRACT

The effect of sample-current power-supply ripple on the measurement of dc critical current is reported. Measurements were made on multifilamentary NbTi superconductor. In general, ripple in a current supply becomes more significant above 500 A because effective filtering is difficult. The presence of current ripple reduces the measured dc critical current. Ripple also causes noise at the input to the voltmeter used for the measurements. The quantitative effect of current ripple was studied using a battery current supply modified to allow the creation of ripple current with variable frequency and amplitude. Problems common to all large-conductor critical-current measurements are discussed.

INTRODUCTION

The presence of current ripple (any periodic departure from a dc output level) reduces the measured dc critical current ( $I_c$ ). In addition to quantifying this effect, an attempt was made to determine its source. Several possibilities are discussed.

The  $I_c$  measurements reported here were made using a straight sample geometry and a radial-access magnet. The  $I_c$  was defined as the dc current at which the measured electric-field strength rose to  $0.2 \mu\text{V}/\text{cm}$ . A battery current supply was modified to allow the creation of current ripple with variable frequency and amplitude. Two types of voltmeters were used to measure the sample voltage. One was an analog nanovoltmeter and the other was a digital nanovoltmeter. Both were direct-current meters with an amplified analog output, which was input to a digital processing oscilloscope. The voltage signal of a current-sensing resistor was split, amplified, and fed into two channels of a digital processing oscilloscope. One of these current signals was filtered to give the dc component and the other was unfiltered (passed wide band). A total of eight channels (two current and six voltage) were used to acquire data simultaneously. The sample voltage was measured at relatively fixed current ripple and numerous dc bias currents. These points along the voltage-current (V-I) curve were analyzed to determine  $I_c$ . The precision of the  $I_c$  measurement was about  $\pm 1\%$ .

\* Contribution of NBS, not subject to copyright.

The performance of the battery power supply as a source of ac current at several frequencies was evaluated by measuring the peak amplitude and rms values of the output current. To judge the shapes of the waveform the ratio of the peak amplitude to the rms value was compared to the ideal value for the given waveform (1.73 for a triangular wave and 1.41 for a sinusoid). For both waveforms and all frequencies (60 Hz triangle; 60, 360, and 1000 Hz sinusoids) the variation between the ideal and measured ratios increased with increasing ac amplitude. This variation was essentially independent of frequency and had a maximum value of less than 12% at the maximum tested ac amplitude of 70 A. At amplitudes below 40 A, the maximum variation was less than 5%.

The sample voltage has several components. For this work, the intrinsic dc transport V-I characteristic of the superconductor was assumed to have the voltage proportional to the current raised to the power n, where n for the tested sample was about 30.<sup>1</sup> There might be a slight current-transfer voltage but otherwise the real component of the voltage should be zero, within measurement limits, until the current approaches the  $I_c$ . Here, the highly current-dependent flux-flow voltage occurs. The unavoidable loop made by the pair of voltage taps and the segment of the sample between them, will give an inductive voltage proportional to the time derivative of the sample current. There will be a highly asymmetric voltage signal due to periodic entry of the peak current into the flux-flow region of the superconductor at high enough bias currents.

A simple electronic circuit was designed to simulate the intrinsic V-I characteristic of a superconductor. The circuit was used to determine the nanovoltmeter's response to a highly asymmetric voltage waveform. It was also useful for testing and developing data acquisition systems. This circuit was developed based on an idea by J. W. Ekin and J. C. Brauch of this institution. The original idea used a diode in series with a current sensing resistor and this combination in parallel with a high-current shunt resistor. This passive circuit gives a nonlinear V-I characteristic but the curve is not very sharp (n about 10) and it is not adjustable. For the adjustable active circuit, a voltage signal proportional to the sample current is the input and a highly nonlinear current is the output of the circuit. The circuit consists of a variable gain (variable n) operational amplifier with the current-proportional signal as the input and a variable voltage bias point (variable  $I_c$ ). The amplifier output drives the base of a transistor, which has a diode and current sensing resistors in series with the emitter current. These current sensing resistors provided various voltage level waveforms. A  $0.01 \Omega$  series resistor is used to produce a low voltage ( $\sim 1 \mu\text{V}$ ) waveform for the nanovoltmeter to monitor. A  $100 \Omega$  series resistor provides a high voltage signal ( $\sim 10 \text{ mV}$ ) that allows the indirect determination of the input signal to the nanovoltmeter using a wide band amplifier to measure the total voltage waveform.

The sample measured in this experiment was a commercial multifilamentary NbTi superconductor with a diameter of 0.65 mm. The filament twist pitch was 0.8 twist/cm. There were 6006, 5- $\mu\text{m}$ -diameter filaments with a Nb diffusion barrier around each of the filaments. The sample was contacted with several sets of twisted pairs of voltage taps. For this experiment, this allowed simultaneous acquisition of data with several voltmeters to determine variation in the observed effect, any difference in voltmeters, and any effect due to voltage-tap geometry. One voltage tap pair was connected to the sample in such a way that the mutual inductance between the voltage-tap pair and sample was larger. It spanned the same segment of the sample as another lower-mutual-inductance pair. Two other voltage-tap pairs had their wires connected together near the sample and only one of the wires was connected to the sample (referred to as null tap pairs). This provided pairs that should not have any real (resistive)

voltage. One of these pairs had low and the other had high mutual inductance. This allowed for a determination of how the voltmeters measure a purely inductive voltage.

## RESULTS

The  $I_c$  for increasing dc bias current was measured as a function of ac amplitude and frequency using two different types of voltmeters and various pairs of voltage taps. The reduction in the measured dc  $I_c$  versus ac amplitude is shown in Fig. 1. The ac amplitude is the peak value of the ac component of the current waveform (not peak-to-peak or peak of total current). These data were taken using an analog nanovoltmeter. The range of ac amplitude covered 0 to 50% of the dc bias-current ( $I$ ) which was about 140 A at 8 T. A reference line was drawn for an  $I_c$  reduction equal to the ac amplitude. For all frequencies and waveforms, these data are just below this reference line indicating that the effect is to reduce the measured  $I_c$  by slightly less than the ac amplitude. The -60 Hz frequency was labeled negative to indicate that it was a triangular waveform at 60 Hz rather than a sinusoidal waveform. At all of the other frequencies, the waveform was sinusoidal with very little distortion. The zero frequency data had only the intrinsic ripple of the supply, which was about 0.3 A in this operating mode. All of the non-zero frequency data fall on a straight line; all of the curvature takes place between zero ripple and the first point. The triangular waveform was added to determine if the detailed shape of the ripple and the relationship of rms to peak, changed the measured values. These data suggest that the detailed shape is not significant. The ac amplitude, however, does have a significant effect on the measured dc  $I_c$ .

Data taken using a digital nanovoltmeter is shown in Fig. 2. The 60 Hz data of Fig. 2 were measured on the identical pair of voltage taps as the 60 Hz data of Fig. 1. The data at other frequencies were measured simultaneously with the corresponding data on Fig. 1, but with another pair of voltage taps that spanned the same segment of the sample. This other pair of voltage taps had a higher mutual inductance but the results for both pairs of taps were within the experimental limits. The results measured by the two voltmeters were very close. This indicates that the measured dc  $I_c$  does not depend on the voltmeter used. There were, however, other differences between these two voltmeters that will be discussed later. The effect of current ripple was repeated on a number of sample segments and each segment gave similar results.

In order to develop a quantitative understanding of the nanovoltmeter input-output relationship for ac voltage inputs, and thus determine the effect on the measured  $I_c$ , two ac tests were conducted on both the digital and analog nanovoltmeters. The first test (symmetric test) consisted of applying sinusoidal voltage signals of various amplitudes and frequencies to the nanovoltmeter input and measuring the resulting output signal. AC signals of appropriate amplitudes were obtained by dividing the output voltage of an ac signal generator. The objective of the second test (asymmetric test) was to determine the response of the nanovoltmeters to the highly asymmetric ac voltage that is characteristic of a superconductor carrying a sinusoidal current. The superconductor simulator circuit was employed to generate the required asymmetric nanovoltmeter input signals.

The results of the symmetric tests were considerably different for the digital and analog meters. In both cases, the dc output of the meters increased with increasing ac input amplitude. However, the output signal from the analog meter was approximately an order of magnitude greater than that of the digital meter for a given ac input. Defining the ac rejection (ACR) of the nanovoltmeter as one minus the ratio of the dc output voltage

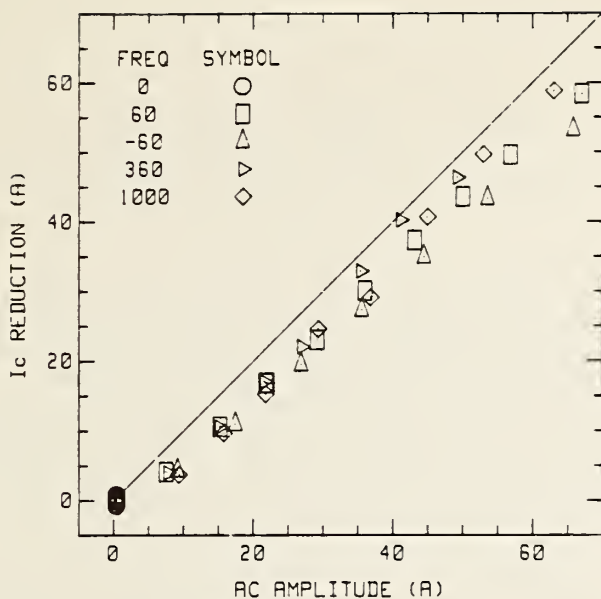


Fig. 1.  $I_c$  reduction versus ac amplitude at several frequencies using an analog nanovoltmeter.

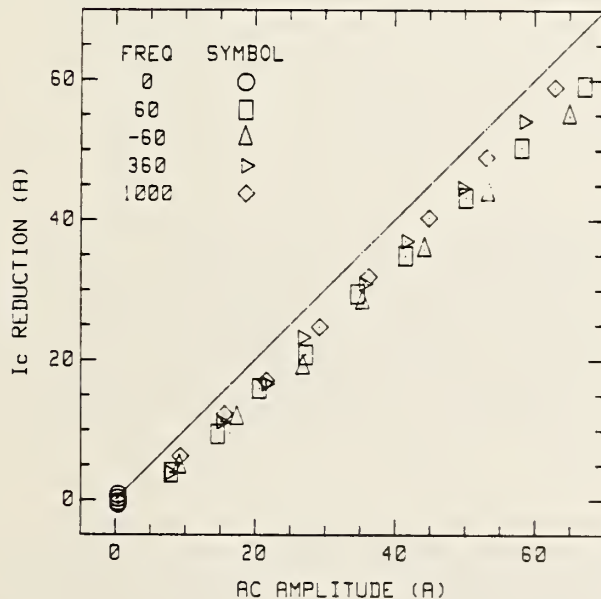


Fig. 2.  $I_c$  reduction versus ac amplitude at several frequencies using a digital nanovoltmeter.

to the peak ac input voltage provides a useful measure of a meter's relative tolerance for ac input voltages. This is not the common mode rejection ratio (CMRR).<sup>2</sup> For the analog meter, a 60 Hz, 500  $\mu$ V peak ac signal resulted in a dc output of 5.2  $\mu$ V, or an ACR of 99.0%. The same input signal applied to the digital meter resulted in a dc output of 0.66  $\mu$ V, or an ACR of 99.9%. This input signal was on the high end of those encountered in this ripple experiment, indicating that a detectable artificial voltage may be observed for the analog meter. For a voltage tap pair with a 1 cm separation, a typical mutual inductance was about 2 nH (53  $\mu$ V peak for 60 Hz and 70 A amplitude; 880  $\mu$ V peak for 1000 Hz and 70 A amplitude). The mutual inductance of the high inductance taps was about 6 nH.

The dependence of the dc output on the input signal's frequency (60, 360, and 1000 Hz) was also investigated. Again, there was a significant difference between the response of the analog and digital meters. Although the dc output of both meters showed a non-monotonic dependence on the input signal's frequency, the analog meter showed a considerably stronger frequency dependence. For the analog meter, a 250  $\mu$ V peak ac signal at 60, 360, and 1000 Hz resulted in a dc output of 0.8, 3.5, and 0.5  $\mu$ V respectively. The same input signals applied to the digital meter resulted in a dc output of 0.14, 0.16, and 0.10  $\mu$ V respectively.

In the case of the asymmetric test, the behavior of the two meters was essentially the same. A broad range of dc biased sinusoidal signals was applied to the input of the simulator circuit resulting in a large variety of typical asymmetric nanovoltmeter input signals. As before, three ac frequencies (60, 360, and 1000 Hz) were tested. In order to determine the nanovoltmeters' response to these input signals, the signals were observed and analyzed on a digital processing oscilloscope. The peak to peak, time average, and rms values of the input signals were thus determined and compared with the output of the nanovoltmeters. The results were that, regardless of the meter being tested or the character of the input signal (frequency, dc bias level, and ac amplitude), the output signal was always within 5% of the time-average (dc) value of the input signal. In other words, the nanovoltmeter behaves like a very low-frequency, low-pass filter, passing the dc component and rejecting the ac component of the input signal. This behavior is consistent with the symmetric test where the meters were shown to ignore sinusoidal input signals.

## MODEL

The motivation for modeling this effect is to help understand what is being measured and how to generalize these results to different samples, ripple, and voltmeters. It will become clear that the shape of the V-I curve and the shape of ripple will change the magnitude of this effect. To extend the dc  $I_c$  criteria to a general current waveform in a way consistent with the design limits of a superconductor application, the measured voltage criteria should reflect the ohmic power loss within the superconductor. Differentiation between voltage and electric field strength criteria will be dropped in this section.

The magnitude of the effect of ac ripple on the measurement of dc  $I_c$  can be calculated for the case of a normal, ohmic sample which would have an  $n$  of 1. For the purpose of this argument, start with the definition of  $I_c$  as the rms value of the total current (ac and dc) at which the rms of the total voltage equals some criterion. This would be correct for a normal, ohmic sample because it is analogous to the derivation of ac power. For sinusoidal waveforms, the time average of the instantaneous power is the

product of the rms of the current and the rms of the resistive voltage. However, measurements of this voltage would require a complex voltmeter that could separate the resistive from the inductive voltages and be capable of measuring the rms of the total (ac and dc) resistive voltage. Based on this definition of  $I_c$  and an  $n$  of 1, the measured dc  $I_c$  would be equal to the square root of,  $I_c$  without ripple squared minus the rms of the ripple squared. For example, the power of 99.9 A dc plus 5 A rms ac is equal to the power of 100 A dc ( $99.9 = ((100)^2 - (5)^2)^{1/2}$ ). The two components of current add in quadrature, thus for a low percentage ripple the effect on the dc value is very small, for  $n$  of 1.

A dc voltmeter will measure the time average of the voltage, which is close to the correct quantity to measure for a superconductor with finite  $n$ . Consider the case where the dc bias current is well below the flux-flow region and the ac amplitude is just large enough to put the total current into the flux-flow region. The instantaneous voltage signal will be zero except at the peak of the current when it will look like a periodic delta function. Considering the ac power analogy, the current is fairly constant for the period of non-zero voltage and the time average power becomes the product of the time average of the two. Thus the dc voltmeter is the proper instrument to use based on the definition of  $I_c$  that relates to the average power. It can be shown that for an  $n$  of 2 and a sinusoidal waveform, the time average of the voltage gives the same dc  $I_c$  as the time average power for the case of  $n$  equals 1. In general, the difference between the time average voltage and the time average power is a difference of 1 in the exponent. For relatively low amplitudes, the effect can be approximated using the first few terms of the binomial series for the instantaneous voltage. For an  $n$  of 30, this gives 98.3 A dc plus 5 A rms ac is equal to 100 A dc (i.e. the measured dc  $I_c$  would be reduced by 1.7 A). For an  $n$  of infinity, it is apparent that the dc voltmeter will give a reduction in the measured  $I_c$  that is equal to the ac amplitude. This sets the limits for the effect and these are consistent with the experimental data. Current ripple should be considered as a percentage of  $I_c$  and this in combination with  $n$  can be used to estimate the effect.

## DISCUSSION

The analyzed data from both the digital and the analog voltmeters gave the same  $I_c$ . However, some  $I_c$  data taken with the analog nanovoltmeter indicated the presence of a current-transfer voltage.<sup>1</sup> This was not true of the data taken with the digital meter. It is believed that this behavior is simply an artifact of the measurement system and not the result of a true current-transfer voltage. There are two characteristics of the measurement system that may explain this effect. One concerns the sample current supply and the other concerns the nanovoltmeter. First, at high ac amplitudes the sample current supply's ac amplitude increases with increasing dc bias level which results in an increasing inductive voltage at the sample voltage taps. Second, as was determined in the symmetric voltage test, the nanovoltmeters have a small dc voltage output when subjected to an ac input, and this dc voltage increases with increasing ac amplitude. Consequently, during a cycle of data acquisition, the nanovoltmeter has an increasing dc voltage output which is interpreted by the data analysis program as current-transfer voltage. The digital meter does not indicate this artificial current-transfer voltage because of its considerably greater rejection of symmetric input signals. Finally, agreement between the data taken by the two meters is achieved by simply subtracting the artificial voltage from the analog meter data. When this current-transfer correction is large, significant errors in the determination of  $I_c$  can result. This is probably the reason that the high-amplitude analog-voltmeter data at 360 Hz (worst case ACR) was out of line with the other frequency data.

Although both analog and digital nanovoltmeters have demonstrated predictable input-output behavior with respect to low amplitude input signals, there is an apparent ac amplitude threshold above which their behavior becomes erratic. This erratic behavior varied from a random output to a very low-frequency (less than 1 Hz) and high-amplitude output. These outputs could be positive or negative. Both meters display this erratic behavior but the ac amplitude threshold for the digital meter is approximately 10 mV, whereas the threshold for the analog meter is approximately 1 mV. These results are similar to the symmetric test where the digital meter was shown to have a considerably greater tolerance for ac input signals.

Data taken on the null tap pairs (described in the introduction) were used to determine the voltmeter's response to the symmetric voltage signals during the experiment. These data were consistent with the symmetric test, the artificial current transfer voltage, and the erratic behavior, all of which were presented above. This is further evidence for the assertion that these effects are caused by the ac inductive voltage. A passive RC filter was inserted at the input of the nanovoltmeter to reduce the ac amplitude of the voltage signal. This did reduce the artificial current transfer voltage, and it increased the threshold of the erratic behavior. However, the passive filter introduced more voltage noise. A passive filter may be an option for some experiments. Another possible method of reducing the inductive voltage is to balance the inductance by opening an opposite area within the twisted pair. This area can be adjusted with a high frequency signal during sample preparation.

The self-field loss is the primary type of transient loss present in the case of sample current ripple for this sample geometry.<sup>3</sup> The only effect of transient loss on the  $I_c$  measurement is sample heating, which may raise the temperature of the sample depending upon cooling conditions. The power dissipation is a strong function of frequency, amplitude, and current density. Computed self-field loss (for the 30 cm sample) at 8 T and the highest ac current amplitude was 3 mW at 60 Hz (50 mW at 1000 Hz). The effect of current ripple was also measured at 5 T with ac amplitudes up to about 50% of the 340-A dc  $I_c$ . The difference in the power between 5 and 8 T was a factor of 6 for comparable amplitudes and frequencies. There was a slight frequency and amplitude dependence for the 5 T data (higher frequency or amplitude reduced  $I_c$  by more), but the results were still at or below the reference line, reduction less than or equal to the ac amplitude. The lack of a strong frequency, amplitude, and current density dependence of the measured reduction of  $I_c$  indicates that sample heating due to transient losses was not significant for this experiment.

Other sample geometries might have larger transient losses due to current ripple. A change in the sample geometry was made to determine this. The sample was centered in a holder, and four conductors (symmetrically located on a 2-cm diameter circle) were all used for the return current path. This arrangement reduced the effect of the magnetic field from the return current path and reduced the net torque on the sample cryostat.  $I_c$  data was taken at 5 T with four returns and with one return for various frequencies and ac amplitudes. The results with a single return had a slight frequency and amplitude dependence. At 60 Hz (sinusoidal and triangular), these data were within 2 A of the four-return results. At 360 Hz and 100 A ac amplitude,  $I_c$  was reduced by another 8 A. This further reduction is attributed to the additional sample heating due to the transient loss created by the magnetic field of the return current path. For other geometries, such as a coiled sample, this effect could be much larger.

Additional  $I_c$  data were taken at higher frequencies (3 and 10 kHz), but experimental difficulties made the results at these frequencies less

reliable. Transient losses, inductive voltage, waveform distortion, and reduction in available amplitude all became more significant at higher frequencies. The motivation for investigating higher frequencies was to estimate the effect of frequencies near the range of spikes from silicon-controlled rectifiers (SCR) found in most large power supplies. These data indicated the same general trend of reduction in  $I_c$  but with more experimental uncertainty. Perhaps a better model of an SCR spike would be a spike rather than a continuous duty-cycle waveform. An extrapolation of the work presented here would indicate that the effect of the spikes would only be to add a finite amount to the time average of the resistive voltage.

## CONCLUSIONS

This report concludes that the effect of ripple should scale with the percentage of  $I_c$  and the effect will depend upon the shape of the V-I curve ( $n$ ). For an  $n$  of 30 or more and large ripple, the effect of current ripple on the measurement of dc critical current is to reduce it by slightly less than the ac amplitude. A dc voltmeter measures a relevant quantity, the time average of the voltage. A simple electronic circuit was used to test a dc voltmeter's response to an asymmetric waveform that simulates a superconductor's V-I characteristic. Reducing the mutual inductance of the voltage taps is important when testing with power supply ripple present.

A large-conductor test method has to address the reality of power supply current ripple. Power line frequencies and harmonics (up to 3-phase, fully rectified) are the dominant frequencies. Current ripple of 1 to 3% at the maximum current is typical for power supplies in the range of 600 to 6000 A. This ripple is generally a function of output current but the percentage ripple can be higher for intermediate currents. This can be a significant source of measurement error. The direct effect on the sample voltmeter can also introduce measurement error. Sample heating due to transient losses may also be significant for some sample geometries.

## ACKNOWLEDGMENTS

The authors extend their thanks to W. E. Look and H. E. Spilman for their assistance with sample preparation and computer programming; and to R. B. Goldfarb for discussions on transient losses. Research supported by the U.S. Department of Energy through the Office of Fusion Energy and the Division of High Energy Physics.

An effort was made to avoid the identification of commercial products by the manufacturer's name or label, but in some cases these products might be indirectly identified by their particular properties. In no instance does this identification imply endorsement by the National Bureau of Standards, nor does it imply that the particular products are necessarily the best available for that purpose.

## REFERENCES

1. L. F. Goodrich and F. R. Fickett, "Critical Current Measurements: A Compendium of Experimental Results," *Cryogenics* 22, 255-241 (1982).
2. L. F. Goodrich, S. L. Bray, W. P. Dube, E. S. Pittman, and A. F. Clark, "Development of Standards for Superconductors, Interim Report Jan. to Dec. 1985," NBSIR 87-3066, National Bureau of Standards, Boulder, Colorado (April 1987).
3. J. W. Ekin, "Superconductors," Chapt. 13 in Materials at Low Temperature, edited by R. P. Reed and A. F. Clark, American Soc for Metals, p. 489-494 (1983).

## Hysteresis losses in fine filament internal-tin superconductors

R.B. Goldfarb and J.W. Ekin

Electromagnetic Technology Division, National Bureau of Standards,  
Boulder, CO 80303, USA

Received 20 June 1986

Hysteresis losses were measured on a series of fine filament Nb<sub>3</sub>Sn superconductors made by the internal-tin process. Hysteresis was measured as a function of filament diameter and interfilament separation using a vibrating sample magnetometer in transverse magnetic field. Losses were greater than expected from the critical state model that expresses loss as a function of filament diameter. Micrographs of the reacted wire cross-sections showed some interfilament bridging for all wires. This gave rise to effective filament diameters that were greater than actual diameters. The critical interfilament separation, above which the losses would be expected to follow the critical state model, was determined.

**Keywords:** Nb<sub>3</sub>Sn; superconductors; fine filament internal-tin superconductors;  
a.c. losses; hysteresis; magnetization

Fine filament superconductors are of interest in a.c. loss studies because, according to the critical state model, hysteresis loss is proportional to filament diameter. Thus, one would expect that wires composed of fine filaments would exhibit small losses. In this study we used a vibrating sample magnetometer in transverse magnetic field to measure the d.c. hysteresis loss for a series of Nb<sub>3</sub>Sn superconductors made by the internal-tin process. There was no transport current. Filament diameter and edge to edge interfilament separation were systematically varied to determine whether filament coupling caused larger than expected hysteresis losses. Such magnified losses may be expressed in terms of an effective filament diameter that is greater than the actual filament diameter. The effective diameter is deduced from the hysteresis loss using the critical state model.

There has been some previous work on hysteresis losses in fine filament superconductors. Dubois *et al.*<sup>1</sup> compared measured and calculated hysteresis in Nb-Ti conductors with filament diameters ranging from 10 to 0.1 μm. They found that, for diameters < 1 μm, effective filament diameters remained at ≈ 1 μm. Information on interfilament separation was not given. Carr and Wagner<sup>2</sup> attributed the asymmetrical hysteresis curve they observed in Nb-Ti with 1.6 μm filament diameter to relatively large surface currents. Ghosh and Sampson<sup>3</sup> studied fine filament Nb-Ti with filament diameters in the range 1–5 μm. They note that, for diameters < 3 μm, the magnetization (and therefore hysteresis loss) is larger than expected from the critical state model. They attribute this to degradation of the magnitudes of critical current owing to filament necking or damage.

In this Paper we show that certain Nb<sub>3</sub>Sn internal-tin conductors with filament diameters < 5 μm have effective filament diameters greater than expected from the critical state model. The ratio of effective to actual Nb<sub>3</sub>Sn filament diameters appears to be a linear function

0011-2275/86/080478-04 \$03.00  
© 1986 Butterworth & Co (Publishers) Ltd

478 Cryogenics 1986 Vol 26 August/September

of interfilament separation. The slope of the line is a function of the local area ratio of matrix material to Nb for each wire. The greater effective filament diameters appear to be a consequence of bridging between filaments.

### Sample preparation and measurement

The multifilamentary Nb<sub>3</sub>Sn wires used in this study were composed of subelements containing 150 filaments each. The array of subelements was surrounded by a tantalum diffusion barrier. Unreacted Nb<sub>3</sub>Sn wires were wrapped on the threads of size 10-24 stainless steel screws. The thread pitch was such that the windings were not in contact with each other. The screws had been previously oxidized to prevent the wires from sticking to the screws. The internal-tin process wires were reacted in a vacuum, with the cold ends out of the furnace, according to the following schedule: one day at 340°C, four days at 580°C and four days at 700°C. This schedule is adequate to fully react the wires for the filament diameters in this study<sup>4</sup>. The residual tin content of each wire after reaction was estimated by the manufacturer to be 8 wt%.

After reaction, the wire coils were unscrewed from the stainless steel screws and the long ends cut off. Each coil was ≈ 1.3 cm in height. The wire volumes were measured using Archimedes' principle. The wire diameter was the same for each sample, 0.681 mm. Thus, the wire length for each coil was obtained.

The average Nb filament diameters before reaction and number of filaments in each sample were provided by the manufacturer. The reacted filament diameters and total volume of Nb<sub>3</sub>Sn in each coil were calculated based on a presumed increase of 38% in filament cross-sectional area after reaction<sup>5</sup>. Local area ratios of matrix to Nb were determined by the manufacturer from the arrangement of the Nb rods in the billets before drawing; the Nb may be thought of as enclosed by adjacent hexagons and the

**Table 1** Parameters for six Nb<sub>3</sub>Sn multifilamentary superconductors

Sample	Nb diameter ( $\mu\text{m}$ )	Nb <sub>3</sub> Sn diameter ( $\mu\text{m}$ )	Local area ratio	Nb separation ( $\mu\text{m}$ )	Nb <sub>3</sub> Sn separation ( $\mu\text{m}$ )	Number of filaments	Length (cm)	Volume Nb <sub>3</sub> Sn ( $\text{mm}^3$ )
3	4.2	4.9	1.5	2.1	1.4	2850	17.8	9.71
6	4.0	4.7	1.8	2.4	1.7	2850	17.3	8.55
9	3.0	3.5	1.5	1.5	1.0	5550	17.1	9.24
12	2.8	3.3	1.8	1.7	1.2	5550	17.0	8.01
15	2.3	2.7	1.5	1.2	0.8	9150	17.0	8.89
18	2.2	2.6	1.8	1.3	0.9	9150	16.8	8.04

cross-sectional areas of Nb and matrix material measured. The average centre to centre filament distance,  $s$ , may be determined from the local area ratio,  $L$ , and Nb filament diameter,  $d$ , by the equation

$$L = (2\sqrt{3}/\pi)(s/d)^2 - 1 \quad (1)$$

The edge to edge Nb separation is simply  $s - d$ .

Table 1 gives relevant parameters for the six samples. Note that the Nb diameter plus Nb separation equals the Nb<sub>3</sub>Sn diameter plus Nb<sub>3</sub>Sn separation. Both sums are equivalent to the centre to centre filament distance (not shown). The matrix to Nb local area ratios of 1.5 and 1.8 correspond to area ratios for reacted Nb<sub>3</sub>Sn of 1.0 and 1.2, respectively.

The magnetic moment was measured at 4.2 ± 0.2 K with a vibrating sample magnetometer in the axis of the coil (i.e. field transverse to the wire if we ignore thread pitch of ≈5.5°). The maximum applied field was 1.6 MA m<sup>-1</sup> (20 kOe). There was no transport current and the coils were open circuited. Magnetization was computed as magnetic moment per unit volume of Nb<sub>3</sub>Sn (i.e. not including the volume of the matrix material). Magnetization was plotted versus external (applied) magnetic field. A typical magnetic hysteresis loop for one of the samples (sample 18) is shown in Figure 1.

## Results

Hysteresis loss was computed by numerically integrating the loop area, ignoring the initial branch. According to the critical state model, for transverse field geometry<sup>6</sup>:

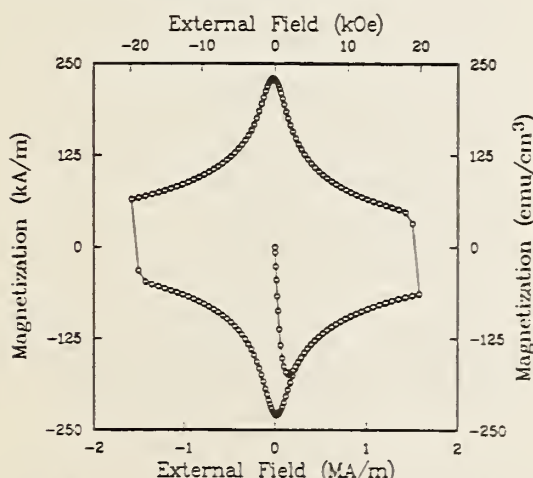


Figure 1 Typical hysteresis loop for a multifilamentary Nb<sub>3</sub>Sn wire made by the internal-tin process (sample 18). Magnetization was computed as magnetic moment per unit volume of Nb<sub>3</sub>Sn

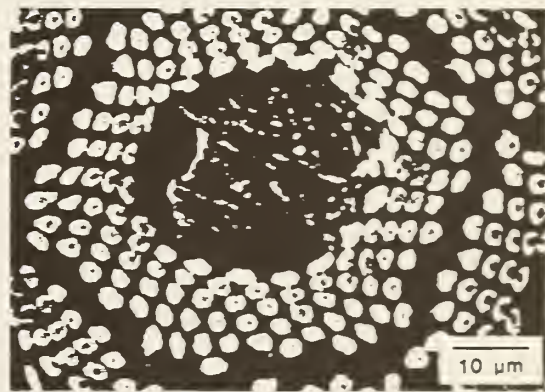


Figure 2 Typical scanning electron micrograph showing some interfilament bridging (sample 18, centre subelement)

$$W = 8J_c d_{\text{eff}} \mu_0 H_0 3\pi \quad (\text{SI units}) \quad (2)$$

Thus, an effective filament diameter,  $d_{\text{eff}}$ , may be defined that is a function of the hysteresis loss,  $W$ , for a maximum applied field,  $H_0$ . Since we did not have data for the critical current density,  $J_c$ , at 1.6 MA m<sup>-1</sup> (20 kOe), we deduced these  $J_c$  based on the critical current of each wire measured at 6.4 MA m<sup>-1</sup> (80 kOe) together with the total Nb<sub>3</sub>Sn cross-sectional area and the measured value of the full penetration field,  $H_p$ , at 1.6 MA m<sup>-1</sup> (20 kOe).  $J_c$ ,  $H_p$  and filament diameter,  $d$ , are related according to the critical state model<sup>6</sup>:

$$H_p = d J_c \pi \quad (\text{SI units}) \quad (3)$$

$H_p$  may be obtained as one half of the field required to reverse the magnetization. From the hysteresis loops,  $H_p$  at 1.6 MA m<sup>-1</sup> (20 kOe) is ≈75 kA m<sup>-1</sup> (940 Oe) for all the loops. This suggests a factor of 10 increase in  $J_c$  compared to the measured value of  $J_c$  at 6.4 MA m<sup>-1</sup> (80 kOe). Applying this factor of 10 to each conductor gives the values of  $J_c$  at 1.6 MA m<sup>-1</sup> (20 kOe) shown in Table 2. We then compute the effective filament diameters of the wires and, additionally, the ratio of the effective to actual Nb<sub>3</sub>Sn filament diameters.

Optical and scanning electron microscopy revealed that some of the filaments in each wire were not entirely isolated but were connected by 'bridges'. An example of this is shown in Figure 2. Such filaments had typically lost their original hexagonal spacing and aligned themselves in rows in the process of wire drawing.<sup>8</sup>

\*Evidence for interfilament bridging in these wires was first presented by A.K. Ghosh and W.B. Sampson<sup>8</sup>

**Table 2** Hysteresis loss and effective filament diameters for Nb<sub>3</sub>Sn

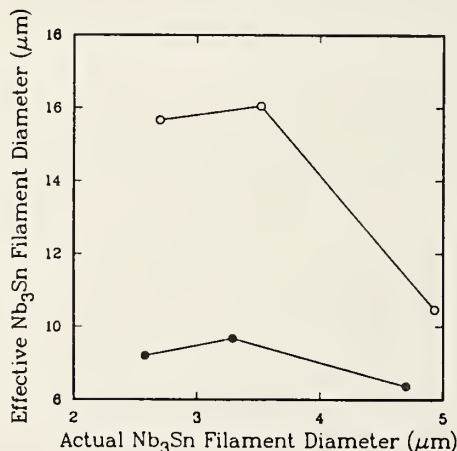
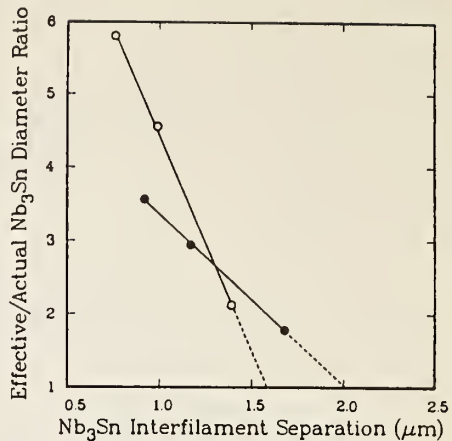
Sample	Estimated value of $J_c$ at 1.6 MA m <sup>-1</sup> (20 kOe)	$W$ (MJ m <sup>-3</sup> )	Effective Nb <sub>3</sub> Sn filament diameter ( $\mu\text{m}$ )	Effective to actual Nb <sub>3</sub> Sn diameter ratio
3	49.4	0.870	10.46	2.12
6	50.6	0.714	8.37	1.78
9	50.6	1.369	16.05	4.55
12	54.3	0.885	9.67	2.94
15	53.8	1.419	15.66	5.80
18	51.9	0.805	9.20	3.56

## Discussion

As shown in *Figure 3*, the relationship between actual and effective Nb<sub>3</sub>Sn diameters is not monotonic. However, some insight is obtained by plotting the ratio of effective to actual Nb<sub>3</sub>Sn diameters versus Nb<sub>3</sub>Sn interfilament separation (see *Figure 4*). It appears that effective filament diameter is a function of both actual filament diameter and interfilament separation. Thus, loss per volume of Nb<sub>3</sub>Sn superconductor is a function of both parameters.

Further refinement is possible by distinguishing among those conductors with the same matrix to Nb local area ratios. These are identified in *Figures 3* and *4* for the two ratios. We see in *Figure 3* that there is less of an increase in effective filament diameter for the conductors with the larger local area ratio. However, we note that in *Figure 4* the abscissa (Nb<sub>3</sub>Sn interfilament separation) is not independent of local area ratio [see Equation (1)]. The apparently linear dependence of the effective to actual diameter ratio on interfilament separation has no physical significance.

A critical interfilament separation can be defined. It corresponds to the separation above which the hysteresis losses would depend on filament diameter as expected from the critical state model. We determined the critical separation for reacted Nb<sub>3</sub>Sn, as shown in *Figure 4*, by

**Figure 3** Effective filament diameter as a function of actual Nb<sub>3</sub>Sn filament diameter for two local area ratios of matrix to Nb. Matrix to Nb area ratio: O, 1.5; ●, 1.8**Figure 4** Ratio of effective to actual Nb<sub>3</sub>Sn filament diameter as a function of Nb<sub>3</sub>Sn interfilament separation for two local area ratios of matrix to Nb. Matrix to Nb area ratio: O, 1.5; ●, 1.8

linearly extrapolating the data to a unity value of effective to actual diameter ratio. The critical separation appears to be a function of the local area ratio. Critical values for the separation between reacted Nb<sub>3</sub>Sn filaments were  $\approx 1.6 \mu\text{m}$  for an area ratio of 1.5 and  $\approx 2.0 \mu\text{m}$  for a ratio of 1.8. The corresponding critical values for the separation between unreacted Nb filaments were 2.4 and 1.5  $\mu\text{m}$ , respectively.

## Conclusions

Certain fine filament superconductors made by the internal-tin process have effective filament diameters that are greater than actual filament diameters. The differences between effective and actual diameters increase as actual diameters decrease, the effect being more pronounced in those wires with the smaller local area ratio of matrix material to Nb. When the ratio of effective to actual diameters is plotted as a function of edge to edge interfilament separation, a more refined picture emerges. The diameter ratio increases linearly with decreasing interfilament separation for each local area ratio. The larger than expected effective filament diameters are likely to be due to interfilament bridging in these wires.

For the practical purpose of conductor design, a critical interfilament separation can be determined. It corresponds to the spacing above which the hysteresis loss would depend on filament diameter as expected from the critical state model. The critical Nb<sub>3</sub>Sn interfilament separation for the conductors used in this study was  $\approx 1.6$  and  $2.0 \mu\text{m}$  for matrix to Nb area ratios of 1.5 and 1.8, respectively. The critical separation is offered simply as a practical design parameter related to the critical state model and for guidance in the manufacture of fine filament internal-tin superconductors such as those described in this Paper.

## Acknowledgements

M. Suenaga made the high field critical current measurements and generously shared samples of the

unreacted wires. A.K. Ghosh astutely pointed out the importance of local area ratios. G.M. Ozeryansky provided valuable information on the physical characteristics of the wires. E.S. Pittman made the optical and scanning electron micrographs. The wires were manufactured by Intermagnetics General Corporation\*. The experimental work was sponsored by the Air Force Office of Scientific Research, USA. Most of the results of this study were presented at the Fourth US-Japan Workshop on High Field Superconducting Materials for Fusion, 1986. This workshop and the microanalysis were sponsored by the US Department of Energy, Office of Fusion Energy.

\*Certain commercial materials are identified to adequately specify the experimental study. In no case does such identification imply recommendation or endorsement by the National Bureau of Standards, nor does it imply that the material is the best available for the purpose.

## References

- 1 Dubots, P., Février, A., Renard, J.C., Tavernier, J.P., Goyer, J. and Hoang Gia Ky NbTi wires with ultra-fine filaments for 50–60 Hz use: Influence of the filament diameter upon losses *IEEE Trans Magn* (1985) MAG-21 t77
- 2 Carr, W.J. Jr and Wagner, G.R. Hysteresis in a fine filament NbTi composite *Adv Cryog Eng* (1984) 30 923
- 3 Ghosh, A.K. and Sampson, W.B. Magnetization and critical currents of NbTi wires with fine filaments *Adv Cryog Eng* (1986) 32 809
- 4 Ghosh, A.K. personal communication (1986)
- 5 Ozeryansky, G.M. personal communication (1986)
- 6 Carr, W.J. Jr. *AC Loss and Macroscopic Theory of Superconductors* Gordon and Breach, New York, USA (1983) 67
- 7 Goldfarb, R.B. and Clark, A.F. Hysteretic losses in Nb-Ti superconductors *J Appl Phys* (1985) 57 3809
- 8 Ghosh, A.K. and Sampson, W.B. Magnetization studies of multifilamentary Nb<sub>3</sub>Sn wires, paper presented at the Fourth US-Japan Workshop on High Field Superconductivity Materials for Fusion (1986)

U.S. DEPT. OF COMM. <b>BIBLIOGRAPHIC DATA SHEET</b> (See instructions)		1. PUBLICATION OR REPORT NO. NBSIR 88-3088	2. Performing Organ. Report No.	3. Publication Date February 1988
4. TITLE AND SUBTITLE  DEVELOPMENT OF STANDARDS FOR SUPERCONDUCTORS				
5. AUTHOR(S) L.F. Goodrich				
6. PERFORMING ORGANIZATION (If joint or other than NBS, see instructions)  NATIONAL BUREAU OF STANDARDS DEPARTMENT OF COMMERCE WASHINGTON, D.C. 20234			7. Contract/Grant No.	8. Type of Report & Period Covered
9. SPONSORING ORGANIZATION NAME AND COMPLETE ADDRESS (Street, City, State, ZIP)  Office of Fusion Energy and Division of High Energy Physics Department of Energy Washington, DC 20545				
10. SUPPLEMENTARY NOTES				
<input type="checkbox"/> Document describes a computer program; SF-185, FIPS Software Summary, is attached.				
11. ABSTRACT (A 200-word or less factual summary of most significant information. If document includes a significant bibliography or literature survey, mention it here)				
<p>A cooperative program with the Department of Energy, the National Bureau of Standards, other national laboratories, and private industry is in progress to develop standard measurement practices for use in large scale applications of superconductivity. This report describes research for the period January 1986 through December 1987. It contains the results of critical current studies on the effect of power-supply current ripple, measurements on cable strands, an interlaboratory comparison (round robin) on a large NbTi monolithic conductor, and a Nb<sub>3</sub>Sn round robin. Several useful current supply circuits have been developed. The reduction in coupling losses in multifilamentary NbTi conductors has been addressed by a study of the magnetic properties of matrix material consisting of dilute alloys of Mn in Cu. In addition, vibrating-sample magnetometry is shown to be adaptable to the measurement of coupling losses, in addition to hysteresis losses, in multifilamentary conductors.</p>				
12. KEY WORDS (Six to twelve entries; alphabetical order; capitalize only proper names; and separate key words by semicolons)				
ac losses; circuit diagrams; critical current; current ripple; hysteresis; magnetization; niobium-tin; niobium-titanium; power supply; round robin; standards; superconductors; susceptibility				
13. AVAILABILITY			14. NO. OF PRINTED PAGES 88	
<input checked="" type="checkbox"/> Unlimited <input type="checkbox"/> For Official Distribution. Do Not Release to NTIS <input type="checkbox"/> Order From Superintendent of Documents, U.S. Government Printing Office, Washington, D.C. 20402. <input checked="" type="checkbox"/> Order From National Technical Information Service (NTIS), Springfield, VA. 22161			15. Price	



